Investigation Of Scalloping Effects Of Radial Turbines With Computational Fluid Dynamics

Anders Jacobsson

Thesis for the degree of
Master of Science

Divison of Thermal Power Engineering
Department of Energy Sciences
Lund Institute of Technology
Lund University, Sweden
June 2016
ISSN: 0282-1990
ISRN: LUTMDN/TMHP-16/5378-SE

Abstract

Turbochargers should both have high efficiency and rapid engine response. By removing material from the rotating parts in the turbocharger, decreases the inertia. Most suited is the turbine in the turbocharger, which has high density because of nickel-based alloys [6]. The material is removed between the radial blades in a shape that looks like a scallop and therefore called scalloping. Volvo Powertrain AB has developed prototypes of non-scalloped turbines and now wants to evaluate if it is possible to design and investigate the performance of different scalloped rotors.

This thesis presents a study on a mixed-flow prototype rotor. The rotor has been scalloped in five different models and covers a range where the inertia has been reduced by 35%. The models were simulated with the Computational Fluid Dynamics program STAR-CCM+ and a single blade passage geometry were designed with Creo Parametrics. Because of the time limit of this study, the simulations have been performed with steady state simulations compared to time-consuming transient simulations. Therefore, the exhaust pulse flow have been simplified as four different points covering the velocity ratios 0.51 to 0.77. A comparison between the scalloped and reference rotor have been made with the total to static efficiency. Also, a visualisation and evaluation of main stream flow through the rotors have been performed. The reference rotor was redesigned to be more comparable to the scalloped models with an outcome of increased efficiency.
The results from the simulations show that a lightly scalloped rotor has similar efficiency as the new reference rotor but with a reduction in transient response time to 2.5%.

Acknowledgement

This master thesis has been performed at Volvo Powertrain AB in Malmö, Sweden. It has been a great time to increase my knowledge about radial turbines, Computational Fluid Dynamics and Creo parametric.

I would like to thank Magnus Genrup how has been an inspiration the last years and guided me to choose this thesis and helped me with all my questions.

I would like to thank Per Andersson at Volvo, who introduced and helped me with all my question about radial turbines and Computational Fluid Dynamics, especially guided me up and down the hill when learning a new program, Starccm+.

I would like to thank Martin Bauer who gave me the opportunity to do this study.

Finally, I would like to thank Sara and my family for the support during this master thesis.

Contents

Chapter 1

Introduction

Scalloped radial and mixed-flow turbines are widely used in turbochargers by manufacturers all over the world. However, detailed analyses and knowledge of how the main stream flow through the turbine is affected by introducing a scalloped back-face have not been evaluated in the open domain. The main effects from scalloping are known and can be divided into four parts according to Table 1.1.

Table 1.1: Benefits and drawback of a scalloped turbine.

Drawback:
Decrease in efficiency

Benefits:
Decrease in inertia
Decrease in centrifugal stresses

Scalloping a turbine is done by simply removing material from the turbine at a large radius between the radial inlet section according to figure 1.1. Therefore, it is easy to understand that inertia and centrifugal stresses will decrease [4]. Furthermore, comparing the pictures in figure 1.1 gives a hint that the scalloped turbine may complicate the propagation of the main stream flow between the blade passage and introduce losses, decrease in efficiency. This study will focus on efficiency and inertia.

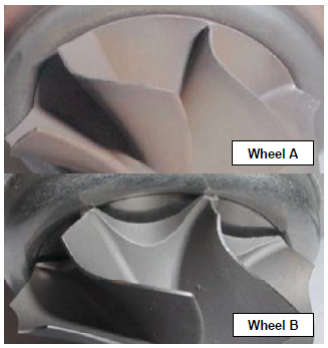

Figure 1.1: Picture from Grahamn Cox [6] shows two mixed-flow turbines. Wheel A: Non-scalloped, Wheel B: Scalloped. The picture simplifies the discussion about Table 1.1.

1.1 Background

It has been a tradition at Volvo Powertrain AB to design and develop prototypes of non-scalloped radial turbines for truck turbochargers. The radial turbines of Volvo have always been designed with high efficiency but the goal has also been to improve them. One way of doing so is to develop a scalloped turbine. The drawbacks with decreased efficiency may now be overcome by the possible reduction in inertia, which would be valuable for Volvo. A reduction in inertia with low degradation in efficiency would yield a turbocharger with faster acceleration and less response time[6]. In plain language, the customer will notice this by a more enjoyable driving experiencing of their Volvo truck. With accurate Computational Fluids Dynamics (CFD) program it may now be possible to develop and test different scalloped turbines with high accuracy at an earlier stage in the design process.

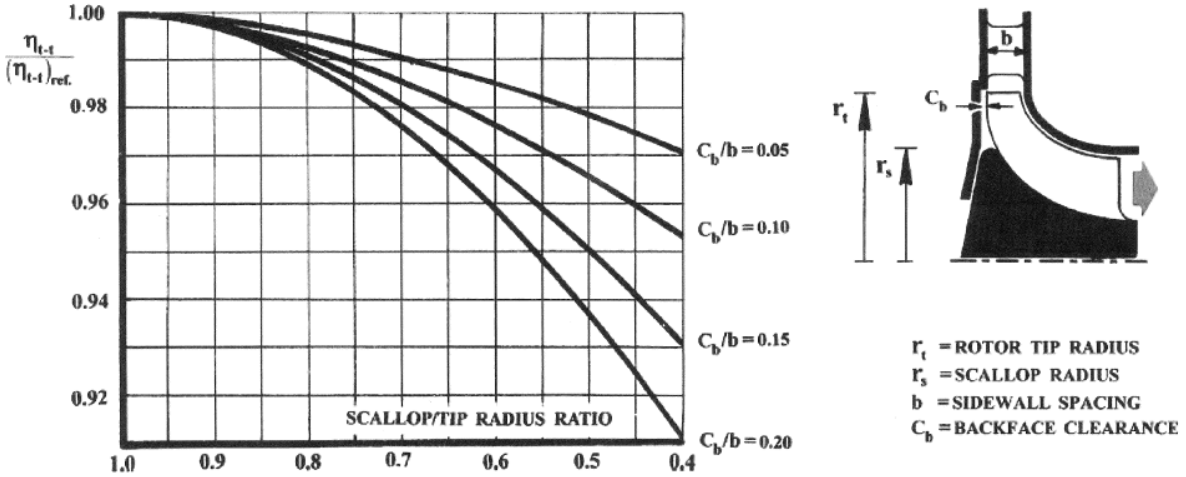

Figure 1.2: Diagram of how total to total efficiency decreases when introducing scalloping at different ratios of sidewall spacing and backface spacing [5]

In spite of the fact that scalloped turbines are used in turbochargers today, there is limited literature dealing with scalloping and how it influences the aerodynamic performance of a radial turbine. However, guidelines by Baines, one diagram by Baskharone and a more detailed article by Cox is known. Figure 1.2 shows the diagram that describes the scalloping effect on the ratio of the total to total efficiency of the scalloped rotor and reference rotor if the scalloped radius is decreased. It also considers the back-face clearance divided by the sidewall spacing, i.e. the width of the inlet in axial direction. If the sidewall spacing is constant then the back-face clearance increases and the efficiency decreases. With a deeper scalloping and wider back-face clearance, the efficiency decreases rapidly, consider the line $C_b/b = 0.20$. The diagram clearly shows that low loss of efficiency from scalloping can only be found when the ratio C_b/b is close to zero. Furthermore, Baines [3] describes the performance penalty of scalloping as difficult to estimate, but gives an indication according to figure 1.2. Baines estimation is clearly below the lines in Table 1.2 at the selected scallop/tip radius ratio.

Table 1.2: The performance penalty when scalloping according to Baines [3].

Scallop/tip radius ratio	$\Delta\eta$
0.8	2
0.65	3-4

Furthermore, In the book Axial and Radial Turbines by Baines et al.[4], the authors refer to Hiett and Johnson (1963) that heavily scalloping results in a loss of efficiency to 3-4% and that it could reduce to 2% if the discontinuity in the hub surface could be minimised. By heavily scalloping Hiett and Johnson

mean a reduction of inertia to 45%. However, there are no pictures or information of how a radial turbine should be designed or explanation of the flow field through the blade passage by Baines. A more detailed analyse of a mixed-flow turbine was done by Graham Cox. In the article A study on the flow around the scallops of a mixed-flow turbine and its effect on efficiency [6]. Graham Cox is comparing two turbines, one is non-scalloped and the second is according to Cox deeply scalloped. Furthermore, the turbines were simulated with CFD and the results compared with a turbo rig. The CFD simulations were both tested with single blade passage steady state and transient. Cox found that at high aerodynamic loading (low velocity ratio, U/C_s) the scalloped turbine allows a leakage that resulting in a strong passage vortex and reduces the efficiency. However, at low aerodynamic loading the flow re-enter the blade passage and seems to increase the efficiency. Cox also claims that the efficiency depends on the design point and the pulse flow. In the real turbo test bench where the turbine experienced a pulse flow between 0.5 to 0.7 U/Cs, the overall effect of the efficiency was a reduction of the total to static efficiency to 1.3 %. Cox does not state the ratio of the scallop/tip radius as Baines and Baskharone but instead gives the decrease in inertia of the scalloped rotor. The momentum of inertia was reduced with 16 % and according to Cox, this would have a noticeable effect on the engine response.

1.2 Objectives

The main objective of this work is to investigate with how scalloping influences the aerodynamic performance of a radial turbine with Computational Fluid Dynamics and what is the achievements of the reduction in inertia. Finally, a comparison with the known loss model by Baskharone should be performed.

1.3 Limitations

Since the purpose is to investigate scalloping on a newly designed radial turbine with on-going development of the compressor and turbocharger house, is this work limited by the possibility to compare the accuracy of the computational fluid dynamics results with real test data from a turbo rig. Furthermore, the simulations are limited by steady state simulations compared to time-consuming transient simulations.

1.4 Methodology

The radial turbine has been scalloped and analysed in the following order.

- A literature study was done to overview previous scalloped radial turbines.
- The program Creo Parametric was used to design and export the five scalloped geometries.
- The program STAR-CCM+ was used to perform numerical calculations and evaluate the scalloped and non-scalloped turbines.
- The program Simulink-ICES was used by Volvo Powertrain to perform a Constant Speed Response simulations for evaluating the transient response time due to inertia and efficiency.

Chapter 2

Theory

2.1 Turbocharger

A turbocharger is a device that is used in many applications, from small gasoline engines to large marine applications[2]. A turbocharger consists basically of three parts, a compressor, a turbine and a shaft which connect the turbine with the compressor. The compressor is driven by the turbine and delivers compressed air to a piston engine. After the combustion the turbine extract work from the pressurised and warm exhaust gas. The main benefit of a turbocharger is that the compressor increases the mass of the air injected into the cylinder. Thereby, more fuel can be added which increases the power output. With a turbocharged engine, it is possible to extract more power compared with the same size of a naturally aspirated engine. Furthermore, a turbocharged engine will also improve its fuel economy because a part of the hot exhaust gases taking cared by the turbine contribute to the overall engine performance. One more major difference compared to other compressor and turbine equipments, e.g. gas turbines, is that a turbocharger handles a great variation in pressure from the piston engines exhaust gases, compared to a gas turbine which is often driven at uniform speed and the design point can be treated as constant. Therefore, the turbocharger's design point includes a wide variation in pressure ratio [2].

2.2 Radial turbine

Radial turbines are mostly used in small turbocharger units for gasoline and diesel engines in cars and trucks. Compared to axial turbines, where the fluid enters the stator blades in the same direction as it exits the rotor blades, is that in a radial turbine the fluid is turned 90 degrees in the meridional plane. The fluid enters the stator blade in the radial direction and leaves the impeller or rotor in axial direction according to figure 2.1. The advantages, compared to axial turbines, why car and truck manufactures choose the radial turbine are; lack of installation space, manufacturing cost, one-piece casting and a more compact power plant[2].

The radial turbine consists of different parts that contribute to its efficiency and working range at design point and off-design. Figure 2.1 shows a cross section of a radial turbine. At section 1, the exhaust gas enters the turbine from a scroll or volute which distribute the flow around the annuls of the turbine. After the scroll it is common to use nozzle vanes that turn and accelerate the flow in the preferred angle towards the rotor or impeller at section 4. The nozzle row can both be fixed or movable called Variable Geometry Turbine (VGT). The difference between them is the choice and trade-off of the cost of the design. For a turbocharger in a car or truck, which experience different mass flow rates from the engine, a VGT-design would be preferable for optimum performance at different speeds. However, an engine running at a constant speed, the efficiency could be more aerodynamically optimised with fixed nozzle row without losses due to leakage around the VGT. However, due to the manufacturing cost and size of the turbocharger it is common to design turbochargers without any nozzle row.
Between section 4 and 6 the radial turbine extract work from the exhaust gas and turn the fluid 90°. This

is the section where most of the losses occur which will be described down below. At the exit of the turbine, often called exducer, the turbocharger can be designed with a diffuser if the meridional velocity is high. It is then preferable to take care of the exhaust energy loss.

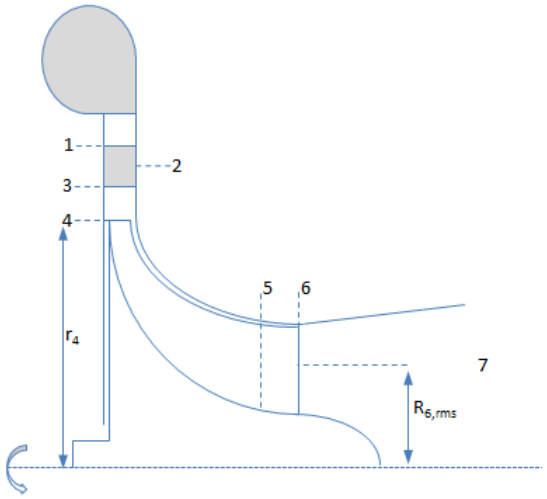

Figure 2.1: Cross section of a radial turbine

As mentioned before radial turbines are compact power plants, and deliver a greater specific power(power per unit mass flow rate) from one single stage compared to an axial turbine stage. The difference can be explained by considering the Euler turbomachinery equation, equation 2.1.

$$W_x = h_{04} - h_{06} = U_4 \cdot C_{\theta 4} - U_6 \cdot C_{\theta 6} \tag{2.1}$$

With the velocity triangles at rotor inlet and rotor exit according to figure 2.2.

$$W^2 = U^2 + C^2 - 2 \cdot U \cdot C \cdot sin\alpha \tag{2.2}$$

The Euler turbomachinery equation can be rewritten as

$$W_x = \frac{1}{2}((U_4^2 - U_6^2) - (W_4^2 - W_6^2) + (C_4^2 - C_6^2)) \tag{2.3}$$

This equation clearly states the contribution of each velocity at inlet and exit of a radial turbine [4]. With a significant change in radius between inlet and exit, the blade speed $(U_4^2 - U_6^2)$, shows that a larger radius change contributes to more work. This can be compared to an axial turbine were the blade speed is constant for one stage. Next term, $-(W_4^2 - W_6^2)$, shows that in order to receive high work output the relative velocity should increase from inlet to exit. The last, $(C_4^2 - C_6^2)$, state that the flow needs to be accelerated by the nozzle row before it enters the rotor inlet and the exit of the rotor should be arranged to minimise the absolute velocity. By considering equation 2.1 again, the velocity triangles should be arranged to minimise the absolute velocity at exit and maximise it at the inlet. This gives $C_{\theta 6}$ equals zero, no exit swirl, and $C_{\theta 4}$ equals U_4, equation 2.1 can be rewritten as the

$$W_{max} = U_4^2 \tag{2.4}$$

Now the inlet angle β_4 and exit angle α_6 are zero, which is the assumption for nominal design. If the rotor would be ideal (frictionless) and at nominal design the maximum work equals to the spouting velocity. Spouting velocity (C_s) is the velocity the fluid would have if it were allowed to expand in an ideal nozzle over the same expansion ratio as the rotor [4].

$$\frac{1}{2}C_s^2 = h_{04} - h_{06ss} \tag{2.5}$$

$$W_{max} = U_4^2 = \frac{1}{2}C_s^2 \tag{2.6}$$

and from this the velocity ratio is stated

$$\nu = \frac{U_4}{C_s} = 0.707 \tag{2.7}$$

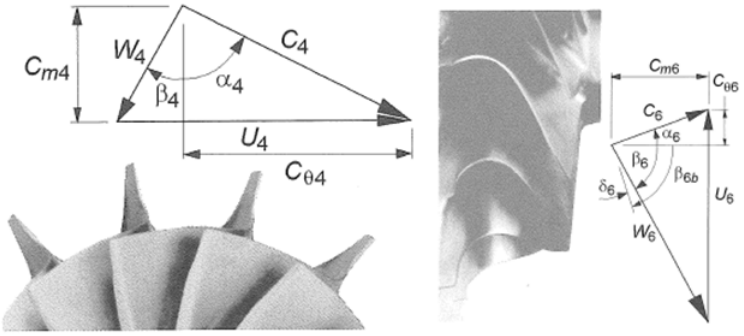

Figure 2.2: Velocity triangles at inlet and outlet of the rotor. The figures are adapted from [4]

2.3 Losses in radial and mixed-flow turbines

Since the flow field in a radial turbine is three dimensional and complex, with regions of secondary flow and vorticies, it may be preferable to dived the rotor region in inlet and outlet. Where at the inlet flow is in the radial direction and at the outlet flow is in the axial direction. This simplification ignores the turning process that the fluid does between the inlet and outlet in a radial turbine. At the design point with optimum efficiency, the flow needs to enter the inlet at a negative optimum incidence angle, this phenomenon has been visualised by Wooely and Hatton (1973) [4]. Also included in the loss called Incidence loss and refers to any work where the turning of the flow is not at the optimum angle to the blade passage.

$$i = \beta_4 - \beta_{opt} \tag{2.8}$$

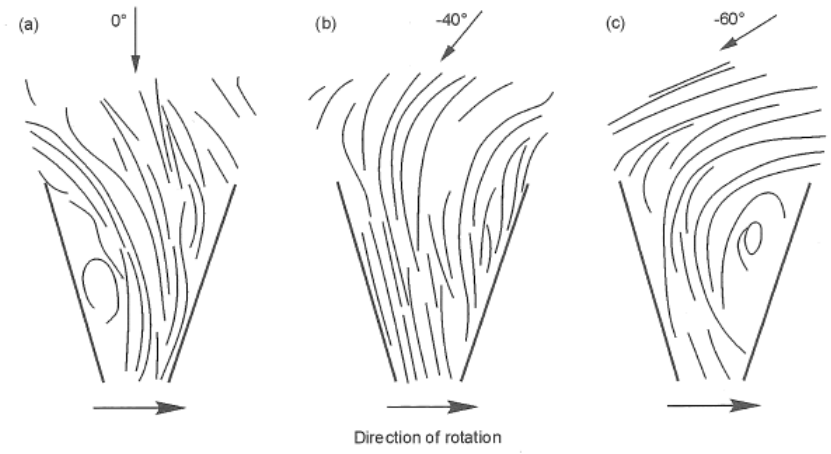

Figure 2.3: Visualisation of the separation in inlet region at different incidence angles by Wooly and Hatton 1973 from [4]

According to figure 2.3, three different inlet flow angles has been analysed. At zero inlet angle the flow will separates after the leading edge and generate a strong recirculation at the suction side. For an inlet angle at -60 degree the flow will now separate after the leading edge at the pressure side. For this particularly turbine was is found that the optimum inlet angle at -40 degree made the flow more uniform in the blade passage and without any separation. This phenomenon happens because of two things in

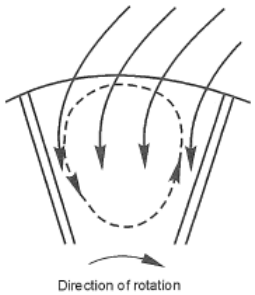

Figure 2.4: Schematically figure for the recirculation in the inlet region of a radial passage from [4]

the inlet region. Firstly, when the flow is entering the inlet there is little or no turning of the flow[4]. When the flow moves inward the blade speed U decreases with the radius but the tangential velocity $C_\theta = K/r$ increases due to low loading(no turning) [8]. Now the relative velocity vector move towards the positive direction of the rotation which is the pressure surface of the rotor. Secondly, when the radius

is decreasing a Coriolis acceleration ($2WxΩ$). Angular speed of the rotor is Ω and W is the relative velocity vector. Because of the Coriolis acceleration decreases as the flow is moving inward, cause this a stronger cross-passage force at inlet and a secondary flow is set up in the blade passage according to figure 2.4 [4]. The secondary flow is in the opposite direction of the rotation.
At the exducer region the flow between the blade passage is both in the axial and tangential direction, but now the flow is turned heavily before the trailing edge of the rotor. This causes the flow to have a large tangential component, and now a Coriolis acceleration is set up in the radial direction which moves the fluid from hub to shroud. It also acts a cross-passage acceleration between the blades due to the turning of the flow in the tangential direction. These two forces generate complex secondary flows and results in non-uniform distribution of blade loading and the flow velocity at the trailing edge. Kitson (1992) did a schematic picture of the flow near the exit. Figure 2.5 shows the tip leakage from pressure to suction side, contra-rotation passage vortices and the interaction with the Coriolis forces [4].

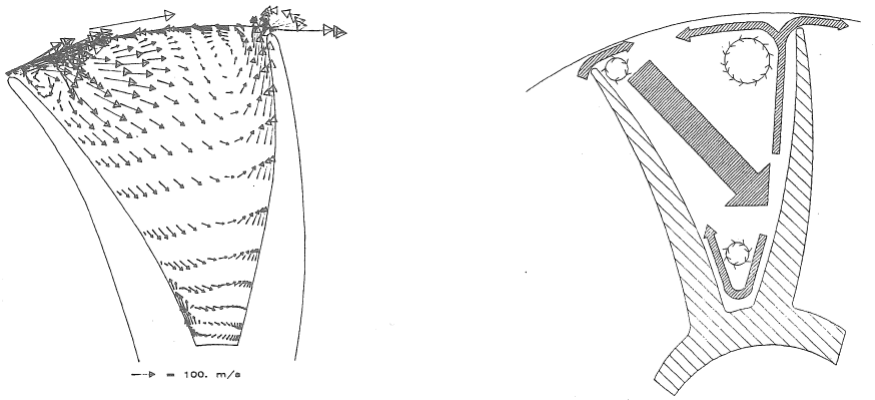

Figure 2.5: From Kitson 1992 [4] showing the relative velocities near the exit and a schematic picture of the secondary flows, vortices and tip leakage.

The tip leakage as mention in the figure arises due to the pressure difference in the blade passage. The leakage occurs through the gap between rotor and shroud from pressure to suction side and as seen in the figure introduces vortices.

2.4 The difference between a mixed-flow turbine and radial turbine

There is a clear difference between a mixed-flow turbine and a radial inflow turbine [2]. According to figure 2.6 the mixed-flow turbine has a leading edge angled to the axis and the main stream flow has both an axial and radial component. Nevertheless, the mixed-flow turbine has almost always a greater mass of the turbine rotor and the momentum of inertia is then larger. This is also displayed by figure 2.6 where the difference of the radius of the hub line curvature introducing a greater mass to the mixed-flow turbine rotor. For reduction of the momentum of inertia, the method scalloping may be used. This is greater for a radial turbine than a mixed-flow turbine. However, the turbine in this report is gently mixed-flow and the consequence of scalloping a mixed-flow turbine need to be considered. When scalloping a mixed-flow turbine a forward-facing step is introduced in the axial direction according to figure 3.2. According to Cox [6] this may introduce an additional loss mechanism in the turbine. Also Baines [2] recommends a smoother profile of the scalloped surface for a mixed flow turbine according to figure 2.7. Baines proposes that the heat shield may be profiled to avoid major discontinuity of the flow in the blade passage.

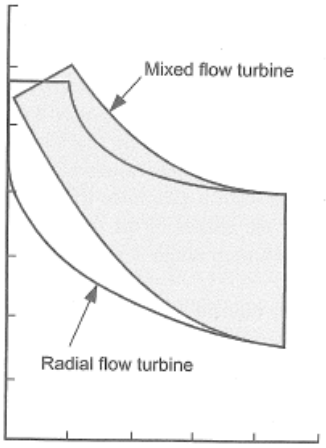

Figure 2.6: The difference between a radial and a mixed flow turbine from Baines [2]

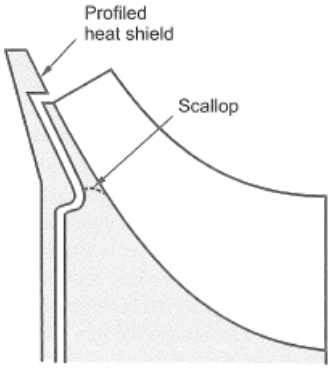

Figure 2.7: A scalloped mix flow turbine design according to Baines [2] with profiled heat shield and smoother scalloped surface.

2.5 Computational Fluid Dynamics

Computational Fluid Dynamics (CFD) is in this work used as the tool to calculate and visualise the flow field through the radial turbine. CFD do not only capture the complexity of the flow field it is also possible to enhance the design of a radial turbine before producing real prototypes.

CFD is a combination of three science fields: Fluid Mechanics, Mathematics and Computer Science. The flow of the fluid is described by the fundamental mathematical equations. The equations are referred in CFD as the Governing Equations due to they govern a particular process of interest. Finally, the governing equations are described with a computer program which visualises the fluid flow in either steady or unsteady state motion for a geometry. The governing equations represent the mathematical statement of the conservation laws of physics [10].

- Mass is conserved for the fluid.
- Newton's second law: The rate of change of momentum equals the sum of the forces acting on the fluid.
- First law of thermodynamics: The rate of change of energy equals the sum of the rate of heat addition to the fluid and the rate of work done on the fluid.

By considering an arbitrary and fixed control volume where the fluid is crossing the surface it is possible to derive the Continuity equation. When the mass is conserved it requires that the rate of change of mass within the control volume is equivalent to the mass flux crossing the surface S of the Volume V.

$$\frac{d}{dt}\int_V \rho dV = -\int_S \rho V \cdot \boldsymbol{n} dS \tag{2.9}$$

Where n is the unit vector. With Gauss's divergence theorem can the surface integral be replaced by a volume integral.

$$\int_V div \rho \boldsymbol{V} dV = -\int_S \rho V \cdot \boldsymbol{n} dS \tag{2.10}$$

Where $\boldsymbol{V}$ is the velocity for each components u, v, w. Now the surface integral can be replaced by the a volume V integral.

$$\int_V \left[\frac{\partial \rho}{\partial t} + \nabla \cdot (\rho V)\right] dV = 0 \tag{2.11}$$

where $\nabla \cdot (\rho V) = div\ \rho V$. Equation 2.11 is valid for any Volume V and finally state the Continutiy equation.

$$\frac{\partial \rho}{\partial t} + \nabla \cdot (\rho V) = 0 \tag{2.12}$$

The Continuity equation can also be described in a cartesian coordinate system and is then in a partial differential form.

$$\frac{\partial \rho}{\partial t} + \frac{\partial \rho u}{\partial x} + \frac{\partial \rho v}{\partial y} + \frac{\partial \rho w}{\partial z} = 0 \tag{2.13}$$

Now consider the same small control volume but instead of the flow through volume consider the forces. With Newton's second law, the sum of the forces action on the fluid element equals the product of its mass and the acceleration of the fluid element and with a cartesian coordinate system and only consider the x-direction Newton's second law states.

$$\sum F_x = m a_x \tag{2.14}$$

With the acceleration

$$a_x = \frac{Du}{Dt} \tag{2.15}$$

and the mass of the fluid element m is $\rho\Delta x\Delta y\Delta z$ gives

$$\rho\frac{Du}{Dt}\Delta x\Delta y\Delta z \tag{2.16}$$

And by expanding the sum of the forces in the left-hand side of equation 2.14 which includes body forces and surface forces. The final equation for Newton's second law is then

$$\rho\frac{Du}{Dt} = \frac{\partial\sigma_{xx}}{\partial x} + \frac{\partial\tau_{yx}}{\partial y} + \frac{\partial\tau_{zx}}{\partial z} + \sum F_x^{bodyforces} \tag{2.17}$$

The remaining $\sum F_x^{bodyforces}$ is a sum of gravity, centrifugal, Coriolis and electromagnetic forces. And for y-momentum and z-momentum.

$$\rho\frac{Dv}{Dt} = \frac{\partial\tau_{xy}}{\partial x} + \frac{\partial\sigma_{yy}}{\partial y} + \frac{\partial\tau_{zy}}{\partial z} + \sum F_y^{bodyforces} \tag{2.18}$$

$$\rho\frac{Dw}{Dt} = \frac{\partial\tau_{xz}}{\partial x} + \frac{\partial\tau_{yz}}{\partial y} + \frac{\partial\sigma_{zz}}{\partial z} + \sum F_y^{bodyforces} \tag{2.19}$$

where σ_{xx}, σ_{yy} and σ_{zz} are normal stress due to pressure and normal viscous stress components τ_{xx}, τ_{yy} and τzz which is perpendicular to the control volume. And with Newton's law of viscosity the normal and tangential viscous stress components can be described.

$$\sigma_{xx} = -p + \tau_{xx},\ \sigma_{yy} = -p + \tau_{yy},\ \sigma_{zz} = -p + \tau_{zz} \tag{2.20}$$

$$\tau_{xx} = 2\mu\frac{\partial u}{\partial x} + \lambda\left[\frac{\partial u}{\partial x} + \frac{\partial v}{\partial y} + \frac{\partial w}{\partial z}\right],\ \tau_{yy} = 2\mu\frac{\partial v}{\partial y} + \lambda\left[\frac{\partial u}{\partial x} + \frac{\partial v}{\partial y} + \frac{\partial w}{\partial z}\right],\ \tau_{zz} = 2\mu\frac{\partial w}{\partial z} + \lambda\left[\frac{\partial u}{\partial x} + \frac{\partial v}{\partial y} + \frac{\partial w}{\partial z}\right] \tag{2.21}$$

$$\tau_{xy} = \tau_{yx} = \mu(\frac{\partial v}{\partial x} + \frac{\partial u}{\partial y}),\ \tau_{xz} = \tau_z x = \mu(\frac{\partial w}{\partial x} + \frac{\partial u}{\partial z}),\ \tau_{yz} = \tau_{zy} = \mu(\frac{\partial w}{\partial y} + \frac{\partial v}{\partial z}) \tag{2.22}$$

where the constants μ and λ are respectively dynamic viscosity for stress to linear deformation and viscosity which relates stresses of the volumetric deformation. With the combination of equations 2.17, 2.18, 2.19, 2.20, 2.21 and 2.22 is then the Navier stokes (momentum) equations:

$$\rho\frac{Du}{Dt} = -\frac{\partial p}{\partial x} + \frac{\partial}{\partial x}\left[2\mu\frac{\partial u}{\partial x} + \lambda\left(\frac{\partial u}{\partial x} + \frac{\partial v}{\partial y} + \frac{\partial w}{\partial z}\right)\right] + \frac{\partial}{\partial y}\left[\mu(\frac{\partial v}{\partial x} + \frac{\partial u}{\partial y})\right] + \frac{\partial}{\partial z}\left[\mu(\frac{\partial v}{\partial z} + \frac{\partial u}{\partial x})\right] + \sum F_x^{bodyforces} \tag{2.23}$$

$$\rho\frac{Dv}{Dt} = -\frac{\partial p}{\partial y} + \frac{\partial}{\partial y}\left[2\mu\frac{\partial v}{\partial y} + \lambda\left(\frac{\partial u}{\partial x} + \frac{\partial v}{\partial y} + \frac{\partial w}{\partial z}\right)\right] + \frac{\partial}{\partial x}\left[\mu(\frac{\partial v}{\partial x} + \frac{\partial u}{\partial y})\right] + \frac{\partial}{\partial z}\left[\mu(\frac{\partial v}{\partial z} + \frac{\partial w}{\partial y})\right] + \sum F_y^{bodyforces} \tag{2.24}$$

$$\rho\frac{Dw}{Dt} = -\frac{\partial p}{\partial z} + \frac{\partial}{\partial z}\left[2\mu\frac{\partial w}{\partial z} + \lambda\left(\frac{\partial u}{\partial x} + \frac{\partial v}{\partial y} + \frac{\partial w}{\partial z}\right)\right] + \frac{\partial}{\partial x}\left[\mu(\frac{\partial v}{\partial x} + \frac{\partial u}{\partial y})\right] + \frac{\partial}{\partial z}\left[\mu(\frac{\partial v}{\partial z} + \frac{\partial w}{\partial x})\right] + \sum F_z^{bodyforces} \tag{2.25}$$

Finally, the first law of thermodynamics says that the time rate of change of energy is equal to the net rate of heat added and the net rate of work done and can be described as:

$$\Delta\dot{E} = \sum\dot{Q} + \sum\dot{W} \tag{2.26}$$

By consider the fluid element in Cartesian coordinate again, the time rate of change of energy is then:

$$\rho\frac{DE}{Dt}\Delta x\Delta y\Delta z \tag{2.27}$$

The work done on the fluid surface in the x-direction is the products of the surface forces caused by the normal viscous stresses σ_{xx} and tangential viscous stresses τ_{yx} and τ_{zx} and the velocity u. And with the heat added to the the fluid the equation for the conservation of energy is then in x, y, z-direction:

$$\rho\frac{DE}{Dt} = \frac{\partial(u\sigma_{xx})}{\partial x} + \frac{\partial(v\sigma_{yy})}{\partial y} + \frac{\partial(w\sigma_{zz})}{\partial z} + \frac{\partial(u\tau_{yx})}{\partial y} + \frac{\partial(u\tau_{zx})}{\partial z} + \frac{\partial(v\tau_{xy})}{\partial x} + \frac{\partial(v\tau_{zy})}{\partial z} + \frac{\partial(w\tau_{xz})}{\partial x} + \frac{\partial(w\tau_{yz})}{\partial y} + -\frac{\partial q_x}{\partial x} - \frac{\partial q_y}{\partial y} - \frac{\partial q_z}{\partial z} \tag{2.28}$$

With Fourier's law of heat conduction the energy fluxes q_x, q_y, q_z are described

$$q_x = -\lambda\frac{\partial T}{\partial x}, q_y = -\lambda\frac{\partial T}{\partial y}, q_z = -\lambda\frac{\partial T}{\partial z} \tag{2.29}$$

where λ is the thermal conductivity the energy equation becomes:

$$\rho\frac{DE}{Dt} = \frac{\partial}{\partial x}\left[\lambda\frac{\partial T}{\partial x}\right] + \frac{\partial}{\partial y}\left[\lambda\frac{\partial T}{\partial y}\right] + \frac{\partial}{\partial z}\left[\lambda\frac{\partial T}{\partial z}\right] - \frac{\partial(up)}{\partial x} - \frac{\partial(vp)}{\partial y} - \frac{\partial(wp)}{\partial z} + \Phi \tag{2.30}$$

Where the Φ is the dissipation function and is the source of energy due to deformation work, the work is then converted into heat. For a more comprehensive explanation and derivation of the Navier-stokes equations consider Tu et al.[10].

The next task is to apply the Navier-stokes equation in real fluid flow problem. Because real fluid flows often are three-dimensional as in a radial turbine and trying to solve simplified two-dimensional flow problems analytically is a challenging task. Therefore, the partial differential equations of the governing equations are obtained by an approximate solution. The technique is called discretization and convert the partial differential equations and auxiliary condition to a system of discrete algebraic equations. The auxiliary conditions are boundary and initial conditions. The most used discretization methods today are the Finite Difference and Finite Volume method[10]. However, Finite Volume has the advantage to suite for both structured and unstructured mesh and is used by the majority of the commercial CFD-program today. Compared to Finite Difference that needs high degree of regularity of the mesh it should be applied on, which implies limiting in grid stretching and distortion to maintain accuracy. Because STAR-CCM+ using the Finite volume method it is appropriate to consider this method [1]. First, the computational domain is divided into smaller control volumes and then the integral form of the conservation equations are solved for each control volume. All variables are calculated in the centroid of each control volume and then expressed by interpolation at the surface of the control volume where a quadrature approximates the surface and volume integrals. There are two main advantages with this method[10]. Firstly, it can be used on both structured and unstructured mesh as long as the neighbour control volume shear the same boundary. Secondly, the governing equations are turned into face fluxes and because the flux of the volume element face is the same that entering the adjacent volume surface makes the Finite Volume strictly conservative [9] compared to the Finite Difference method.

2.5.1 Solver: Segregated or Coupled solver

STAR-CCM+ has two solvers for solve the algebraic equations of the discretized governing equations: The Segregated and Coupled flow solver. The Segregated model solves each of the momentum equations in turn, one for each dimension. While the Coupled model solves the equation for mass, momentum and energy simultaneously [1]. These two solvers have different performance for different types of flows problem. Which to choose and why depends on the mach number. For highly compressible and super-sonic flows the coupled solver is more robust, particularly in the presence of shocks. Whereas the segregated solver is more suited for low mach number flow and mildly compressible flow [1]. Furthermore, the choice of solver is also based on experience, both from convergence problem and comparison with real test data from a turbocharger rig. From previous simulations and tests at Volvo the segregated solver has proven good accuracy around mach-number one [personal communication, Per Andersson 2016].Therefore is the segregated solver chosen in this study.

2.5.2 Turbulence

To this point, with the continuity and momentum equation the flow can be only be described in the laminar regime. However, most of the flow problems encounter disturbances from the free stream of the fluid motion or surface roughness. If the disturbances increase they will cause turbulence. The origin of turbulence depends on the ratio of inertia forces to viscous forces. This is described by the Reynold's number. For low Reynold's number the viscus forces are stronger than the inertia forces and the flow will remain laminar. For high Reynold's number the inertia forces will be larger than the viscous forces and increase the disturbance and create a random fluctuations [10]. The fluctuations have a rotational structure called turbulent eddies. In order to solve the turbulence of the flow, the governing equation needs to be complemented with a turbulence model. There are several turbulence models, the most common are the $k-\epsilon$, $k-\omega$ and $SST\ k-\omega$ model. Where the $SSTk-\omega$ turbulence model is a combination of $k-\epsilon$ and $k-\omega$. At Volvo the $SST\ k-\omega$ is used for compressor calculations because its performance for boundary layers under adverse pressure gradients whereas the $k-\epsilon$ has proven better accuracy for solving the free stream turbulence in radial turbines [personal communication, Per Andersson 2016]. Therefore, the $k-\epsilon$ turbulence model is chosen in this study. The model is also called the two-equation model because it solves the turbulence flow with two extra transport equations. It determines the energy in the turbulence with the turbulent kinetic energy k and the rate at which the turbulence kinetic energy is dissipated to heat with ϵ[10]. The standard model is complemented in STAR-CCM+ with the realizable two layer model which uses a two-layer approach to solve the viscous sub-layer inside the turbulent boundary layer. The two-layer model gains the flexibility of an all y_+ wall treatment[1]. The y^+ value is the dimensionless distance to the wall and defined as

$$y^+ = \frac{u_* y}{\nu} \tag{2.31}$$

where u_* is the wall friction velocity, y is the distance to the wall and ν is the kinematic viscosity. The wall friction velocity is defined with the wall shear stress τ_w and is defined as

$$u^* = \sqrt{\frac{\tau_w}{\rho}} \tag{2.32}$$

where ρ is the fluid density[10]. There is a relationship between the y_+ and the first node of the meshing. The y_+ can not be too large so it falls outside the boundary layer region, if this happens may the wall function calculate the flow properties incorrectly. For solving the viscous sublayer the y_+ value should be below five. The y_+-value can be visualised after the calculation is performed by the CFD-program[1].

Chapter 3

Design of the scalloped turbine

3.1 Scalloped turbines Model A-F

The non-scalloped turbine was scalloped in five different designs according to figure 3.1. The designs are ranged from light to deeply scalloped and for the two deeply scalloped turbines two different designs of the width of blade back-face was made. At models A to E the scalloped radius decreases and for model F

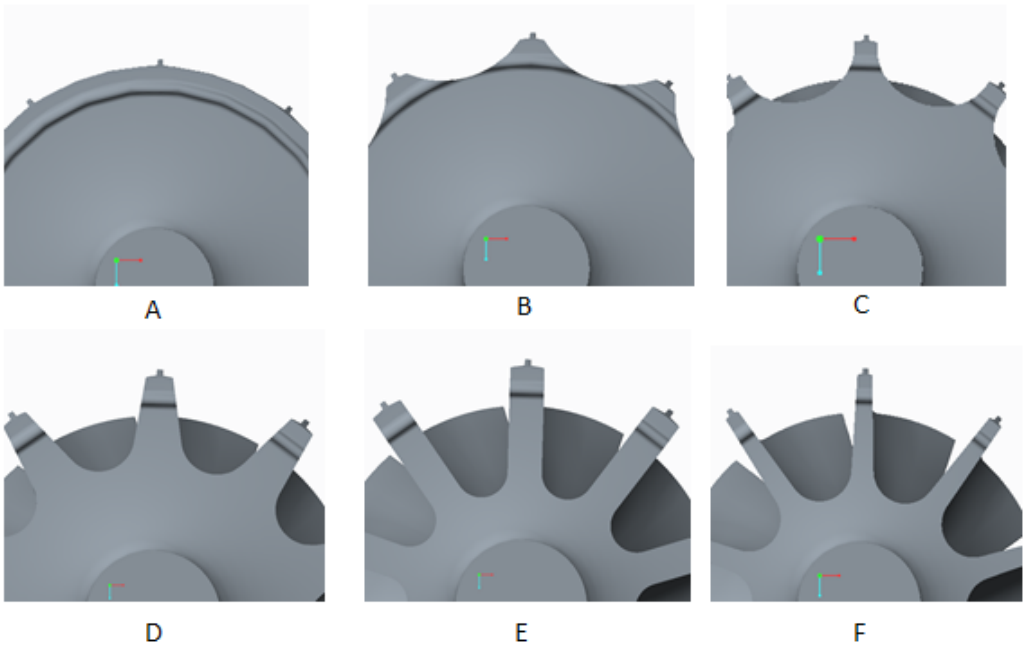

Figure 3.1: Pictures of the five scalloped back-faces. From the non-scalloped turbine to deeply scalloped with I-design. The designs are named Model A, B, C, D, E and F.

the blade back-face is thinner compared to model E. The purpose of the models E and F is to investigate how the rotor efficiency is affected by the width of the blade back-face. The characteristics of the designs can be described as a T-design for Model E and I-design for Model F, if the turbines are viewed from the back-face and radially inward. Finally, the scalloped surface for Model B to F is rounded according to figure 3.2.

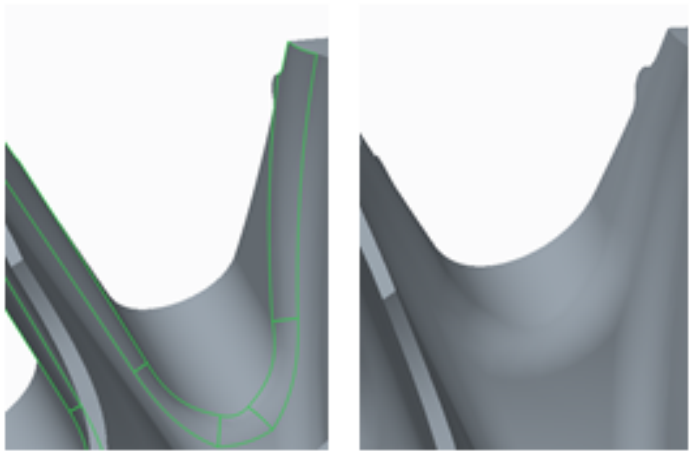

Figure 3.2: Close-up on the scalloped surface for Model E and D, the picture clearly show how the scalloped area is introducing a forward facing-step. The green lines indicate the rounding of the edge to improve the aerodynamics between the blade passage

3.2 CAD geometry

Before it was possible to analyse the scalloped turbines in STAR-CCM+ (CFD), a geometry to describe the turbine blade and blade passage was needed. With the CAD program, Creo Parametics, the original turbine was enclosed by a cylinder larger than the turbine. The geometry is then sketched between one blade on both suction side and pressure side, the sketch also include the back-face cavity were leakage from suction to pressure side occurs when scalloping is introduced. According to figure 3.3, a cut was then generated to cut out $1/10th$ of the cylinder to form a part called Bulk Air.

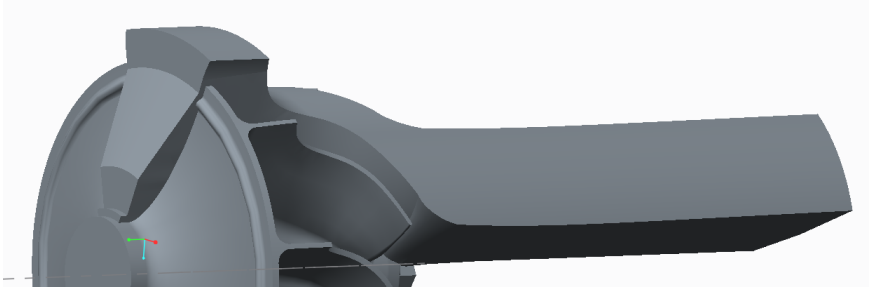

Figure 3.3: Turbine with the part Bulk Air

When Bulk Air was properly designed, the turbine was hidden and Bulk Air was saved as a solid to a Step- or Parasolid-file before it was imported through STAR-CCM+'s 3D-CAD processor. Before the part was saved, an analysis of the mass properties and volume indication ensured that the part was a solid part.

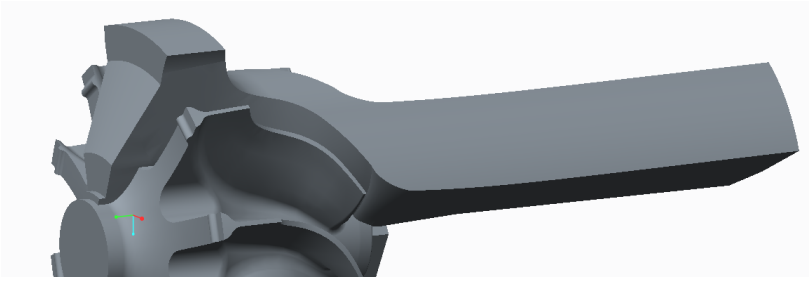

Figure 3.4: Deeply scalloped turbine with the part Bulk Air

Figure 3.4 show how the Bulk Air enclosed the scalloped turbine wheel and generating automatically the geometry for analysing a deeply scalloped turbine with CFD.
Figure 3.5 shows the reference model A and each radius of the scalloped models B to F. The figure also indicates that with a deeper scalloping the back-face cavity will introduce a larger "open" area between the rotor and back-face cavity wall. This area may increase the leakage from pressure to suction side.

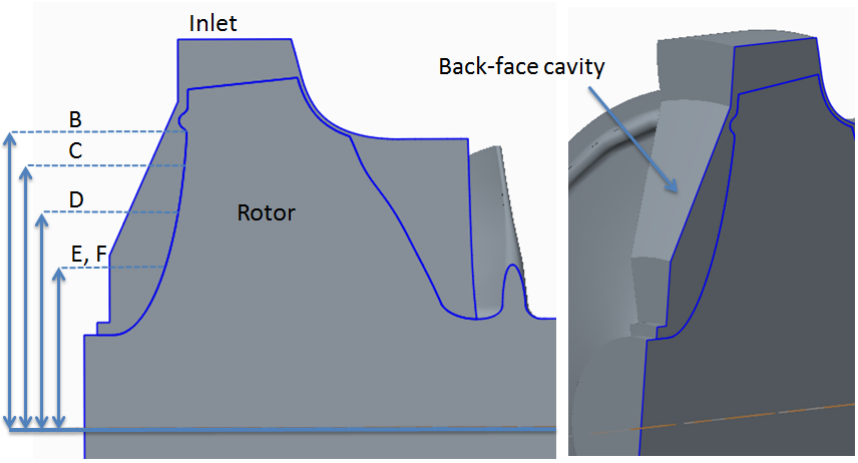

Figure 3.5: Shows the back-face cavity and scalloped radius for each model. Because it is a cross-section of the rotor may the rotor blade appears smaller than it is.

3.3 STAR-CCM+ CFD

3.3.1 Import of Bulk Air and Repair Surface

The file containing the Bulk Air was imported into STAR-CCM+ through the Geometry 3D-CAD processor. At this moment if the geometry was corrupted, e.i. the CAD program has failed to generate a proper solid part, it would be impossible to generate a proper volume mesh on the geometry. However, the step or parasolid-file geometry could consist of small errors according to figure 3.6. By selecting the tool Repair Surface, it was possible to repair the damaged area. The tool also indicates how many corrupted faces the model consists of, when the three selected options indicated zero, as in figure 3.3. The model is then a solid volume and consists of a surface without any holes or corrupted areas.

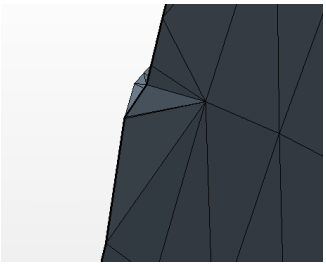

Figure 3.6: Example of corrupted faces on the back-face cavity of the Bulk Air geometry.

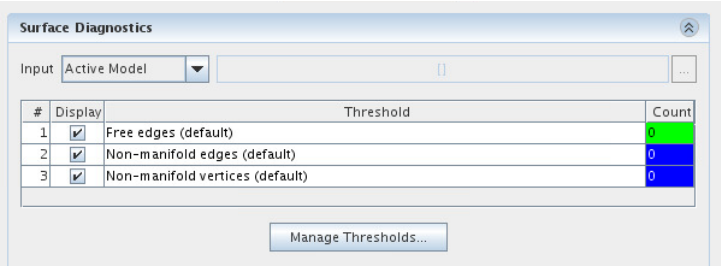

Figure 3.7: Surface diagnostics for control of damaged faces, edges and vertices

The Geometry Part was then divided into different patches according to figure 3.8. Each coloured patch can be combined with another patch and generate a surface. For this specific geometry, the part

was divided into nine separated surfaces according to Table 3.1, which also includes geometry two. Before assigning these surfaces to regions, a periodic contact was established between the two periodic surfaces. Because of the convergence problem at different design points, geometry one was extended with a stationary outlet region and the new geometry was called geometry two, consider figure 3.9. Between Outlet 1 and Inlet 2 an interface was created.

Table 3.1: The geometry one consists of nine surfaces and with the additional outlet region geometry two consists of five more surfaces. All surfaces were assigned as a region and boundaries were created for each surface.

Geometry one	Geometry two
Rotor	Rotor
Rotor back-face	Rotor back-face
Inlet	Inlet
Outlet	Outlet 1
Periodic surface 1	Periodic surface 1
Periodic surface 2	Periodic surface 2
Shroud rotor	Shroud rotor
Shroud outlet	Shroud outlet
Back-face cavity wall	Back-face cavity wall
	Extended outlet:
	Inlet 2
	Outlet 2
	Periodic surface 21
	Periodic surface 22
	Shroud 2

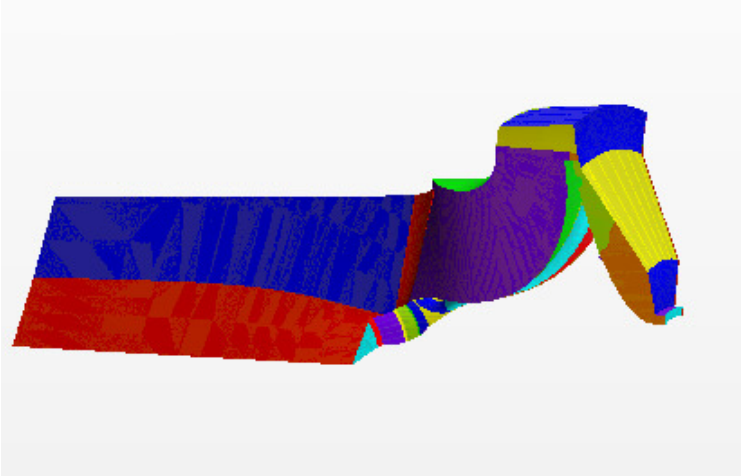

Figure 3.8: Geometry one divided into patches.

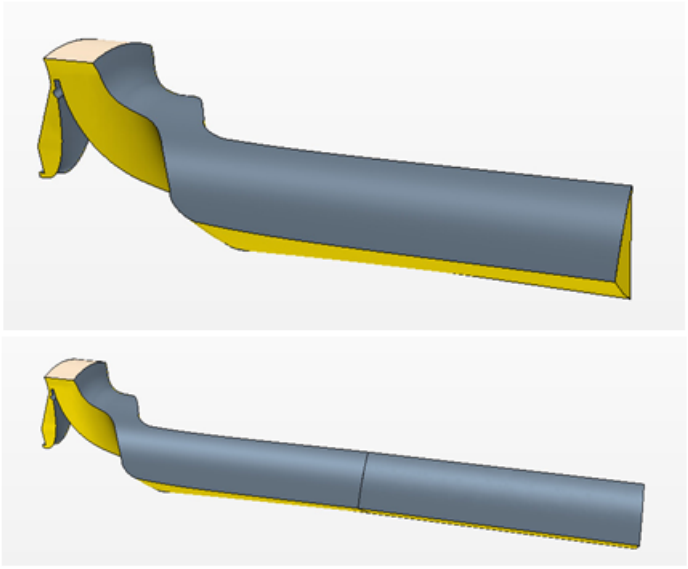

Figure 3.9: Geometry one(top) and two(bottom)

3.4 Choice of Continua

The selected mesh and physics continua were chosen according to a standard at Volvo. The standard has proven good accuracy for previously tested turbines.

3.4.1 Selection of Mesh options

The volume mesh for the turbine geometry was made with three selected mesh options.

- Polyhedral Mesh
- Prism layer
- Surface remesher

It is possible to choose between two types of volume meshers, either tetrahedral or polyhedral. The polyhedral mesh was chosen because of better accuracy and quality of the solution [1], it also leads to quicker convergence of the numerical solution [10]. A prism layer mesher was used to generate orthogonal prismatic cells next to the wall surfaces. The prism layer is used for resolving the boundary layer [1]. Surface remesher is improving the overall quality of the surface before the polyhedral mesh can be generated on the volume mesh [1]. It should be mention that no surface wrapping was needed. Surface wrapping is used when the CAD-geometry is heavily corrupt or of poor quality, e.g multiple intersecting parts or holes and gaps. However, if the CAD-geometry needs this treatment it is better to improve the surface in the CAD-program.
The reference value in Table 3.2 for the mesh was chosen according to the standard.

Table 3.2: Mesh reference values.

Base size	0.5	mm
Number of prism layers	5	
Prism layer stretching	1.5	
Prism layer thickness	33.3	% of base size

In STAR-CCM+ the base size is a reference value for the whole geometry. For each boundaries the surface size of the polyhedral mesh is then chosen relative to the base size.

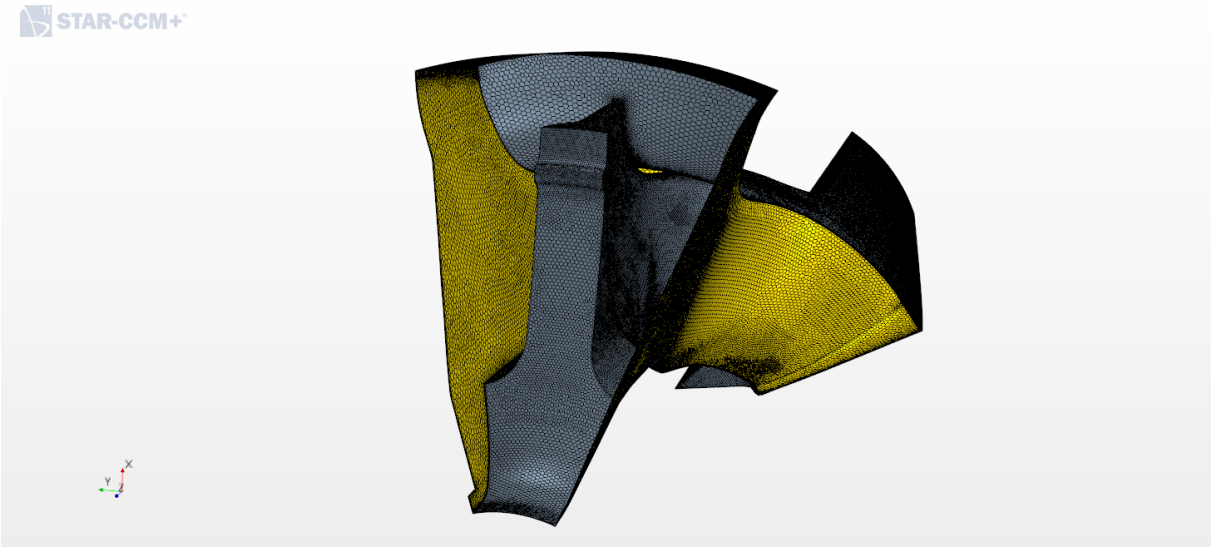

Figure 3.10: Mesh view of Model E shows the deeply scalloped rotor when back-face cavity wall is hidden. The yellow surfaces show that the two surfaces are periodic, i.e the flow on one surface will be equal to the other surface.

3.4.2 Continua Physic Models

In STAR-CCM+ the Physics Models is where different options are chosen for fluid properties, solvers and turbulence model according to Table 3.3 and 3.4. STAR-CCM+ is automatically choosing appropriated wall treatment for solving the boundary layer.

Table 3.3: The choice in the Physics Model Selection in STAR-CCM+

Physic	Model
Space	Three Dimensional
Time	Steady
Materiel	Gas-Air
Flow	Segregated Flow
Equation of state	Ideal Gas
Energy	Segregated Fluid Temperature
Viscus regime	Turbulent
Reynolds-Averaged Turbulence	K-Epsilon Turbulence
Automatically selected models	
Flow	Gradients
Viscus regime	Reynolds-Averged Navier-Stokes
Reynolds-Averaged Turbulence	Two-Layer All y+ Wall Treatment
	Exact Wall Distance

Table 3.4: Additional options for Air

Material Properties	Method	Value	
Dynamic Viscosity	Sutherland's law		
Molecular Weight	Constant	29.03	kg/kmol
Specific Heat	Polynomial in T		
Standard State Temperature	Constant	298.15	K
Thermal Conductivity	Sutherland's law		
Turbulent Prandtl Number	Constant	0.9	

In the continua physics there is also options for initial conditions and values were selected according to Table 3.5.

Table 3.5: Initial Conditions

Condition	Value	
Pressure	150 000	Pa
Static temperature	800	K
Turbulence Intensity	3	%
Turbulent Viscosity ratio	100	
Velocity	[1.0,1.0,1.0]	m/s

3.5 Reference frames

The reference frames are divided into two parts. The default stationary frame in STAR-CCM+ is called Lab Reference Frame. This was the selection for boundaries that should be stationary, e.g. shroud and back-face cavity. The second frame is called Relative Reference frame and is rotation with selected rotating speed. The rotor and rotor back-face is selected as stationary in the relative reference frame, which results that the rotor is rotation compared to the stationary parts.

3.6 Boundary region conditions

3.6.1 Inlet

The inlet was selected as a Mass Flow Inlet with constant total temperature according to Table 3.6 and stationery in the lab frame. The absolute velocity direction was decided from nozzle row calculations done by Volvo with a value of 15.75 degrees from radial. With a cylindrical coordinate system the flow was described as -0.271 in the radial direction, 0.962 in the tangential and 0 in the axial direction.

3.6.2 Outlet

The outlet was selected as a Pressure Outlet and physics values according to Table 3.6. For geometry two the default options for physics conditions was changed according to the section 4.2: Convergence problems. The back flow specification was changed from static to environmental and pressure outlet option from none to average pressure. With these two options, the outlet could handle re-entering flow at the outlet.

Table 3.6: Physical values for Inlet and Outlet

Inlet		
Total Temperature	854	K
Mass flow rates	0.033	kg/s
	0.038	kg/s
	0.045	kg/s
	0.060	kg/s
Outlet		
Static Pressure	120 000	Pa
Static Temperature	700	K

3.6.3 Rotating boundaries: Rotor and Rotor back-face

The Rotor and Rotor back-face were selected a fine mesh, for resolving the flow around the blade and scalloping, with a relative size between 60% and 10 % of the base size. Furthermore, surface proximity option added additional cells between the back-face of the rotor and back-face cavity but also between rotor and shroud for capturing the tip clearance leakage. The rotor and rotor back-face were selected with the no-slip condition and adiabatic walls.

3.6.4 Stationary boundaries: Shroud rotor, Shroud outlet and Back-face cavity wall

These boundaries have the Lab Frame as the reference frame and with the no-slip condition and adiabatic walls.

3.7 Evaluation with Efficiency

To compare the diagram from figure 1.2 by Baskharone with the simulations in STARCCM+ was it necessary to calculate the rotor total to static efficiency according to equation 3.1 [4].

$$\eta_{TS} = \frac{T0_{inlet} - T0_{outlet}}{T0_{inlet}(1 - \frac{P_{outlet}}{P0_{inlet}}^{\frac{\gamma-1}{\gamma}})} \tag{3.1}$$

With CFD the flow field quantities are calculated at discrete points in space, and the inlet and outlet quantities need to be average over section planes. Consider the outlet region where there is variation in temperature due to e.g. tip clearance, vortices and back-flow. By only considering one point in space this may result in great variation between two models. To get accurate results of the efficiency, plane sections of temperature and pressure was chosen as mass flow averaged. Total temperature and total pressure were selected at inlet and outlet according to figure 3.11. However, the ratio of specific heats (γ) was calculated at both inlet and outlet and then the average value was used in equation 3.1. It should be mentioned that real turbo tests at Volvo have the same setup with temperature and pressure equipment placed in the same manner.

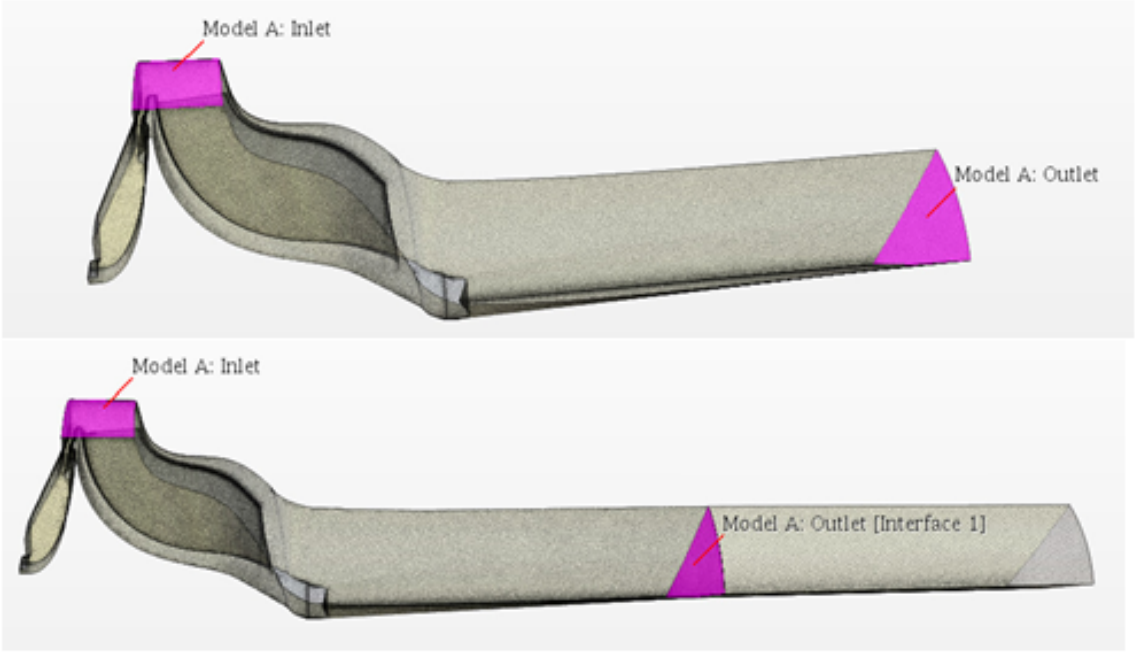

Figure 3.11: Shows the inlet and outlet of the geometry one and two. For geometry two, the interface was selected between the rotating and stationary parts for same accurate result of the efficiency between the geometries.

3.8 Design point and pulse flow interval

Models A-F were tested at one design point according to the left picture in figure 3.12. Design point one was the same reference point as for the first one-dimensional calculations Volvo used when they designed the turbine. The next three points, two, three and four, were selected to represent a small interval that the turbine handle due to the pulse flow of the engine. An example of the pulse flow can also be seen in the picture to the right in figure 3.12. The pulse flow is represented by the thin line at each design point. The

thick dark lines represent constant pressure, and the coloured area represents efficiency, where red is low efficiency and white is high efficiency. It is then easier to understand that the turbine of a turbocharger handles a great variation in pressure for only one design point.

Table 3.7: Design point and interval points for evaluating the performance of Model A-F, where the mass flow is $1/10th$ of total.

	Mass flow rate	RPM	$\frac{U}{Cs}$
Design point 1	0.038	105 000	0.73
Interval point 2	0.045	95 000	0.62
Interval point 3	0.033	105 000	0.77
Interval point 4	0.060	85 000	0.51

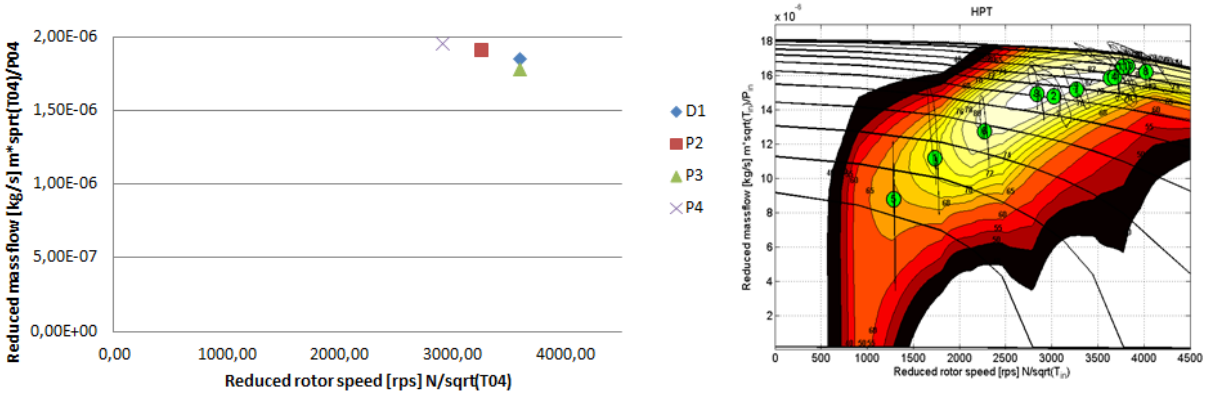

Figure 3.12: Left: The design points 1 and interval points 2, 3 and 4 on a turbine map, where D1 is the reference point and the interval due to pulse flow is P2, P3 and P4. Right: An example of a real turbine map from Volvo, the reference points 1-11 shows the characteristics of the pulse flow with a thin line at different reduced mass flow and reduced rotor speed.

Chapter 4

Accuracy

4.1 Convergence criteria

To establish accurate answers between the different scalloped turbines and design points, it was necessary to decide convergence criteria for the CFD-model. The first step was to evaluate momentum, energy and turbulence through the residual plot. The calculations started with first order of discretization of the convection term. After one thousand iterations and properly converged residuals, the convection term was changed to 2nd order of discretization. The residuals should then converge below 10^{-4} and finally stabilises. The second and the most important step were to create different mass flow averaged report plots and monitor them as the selected scalar field functions converge and stabilise. The selected scalar field functions; mass flow, pressure and temperature are listed in Table 4.1 and were monitored before it was possible to decide if the numerical calculation was stabilised and could deliver an accurate result of the efficiency. Examples of the residuals and report plots can be seen in appendix A.

Table 4.1: Selected scalar field functions for monitoring convergence

Mass flow	Inlet-Outlet
Temperature	T03, T06
Pressure	P03, P6

4.2 Convergence problems

The CFD simulations were calculated with two different geometry models according to figure 4.1. This was needed due to convergence problem that occurred when the design point and interval were tested. Design point one was stable with the first created geometry. However, when the mass flow rate and rotational speed were changed for Interval point two, the first geometry encountered difficulties to solve the flow equations when first order of discretization was changed to second order. The problem was noticed in the outlet region by reversed back flow and later the velocity increased several times above mach number one. When the residuals rapidly increased, STAR-CCM+ was self-forcing a shout down. Before geometry two was designed, several of different continua physic configurations and changes in the geometry were tested until it finally was possible to find a solution for the problem. The solution to the problem was to extend a new outlet section. The new section was stationary with new outlet physics condition. Furthermore, the backflow specification was changed from static to environmental and the pressure outlet was added with an average pressure outlet option. The environmental option added the dynamic head to the pressure outlet boundary instead of only considering the static value [1]. Both options improved the outlet boundary in handling reversed back flow.

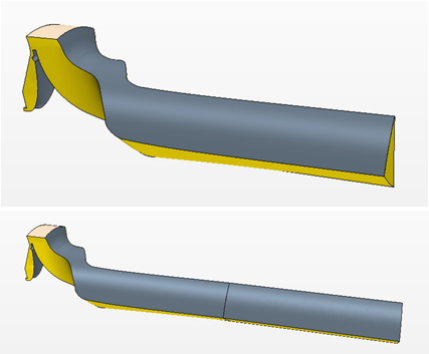

Figure 4.1: Geometry one(top) and two(bottom) with the new stationary geometry.

4.3 Grid independence study

A grid independence study [10] was performed to ensure that the proposed standard mesh would be suitable for the turbine. Model A was calculated with different base sizes according to Table 4.2. The base size value is the reference value for selecting cell size in STAR-CCM+, each region is then selected relative to the base size according to previous chapter. The relative mesh size for each region is static for the five tested base size values in table 4.2 and also for the different design points tested in this report.

Table 4.2: Base size values and number of cells of the volume mesh for grid independence study

4 mm	110455
2 mm	751298
0.5 mm	1412483
0.35 mm	2880530
0.25 mm	6136838

Each base size value was calculated with the same physics and converged according to the convergence criteria. Finally, the parameter to compare the accuracy of the grids was selected to the total to static efficiency. According to figure 4.2 the efficiency changes between base size 4 mm and 0.5 mm. When the mesh was refined with smaller base sizes and the cell number increased rapidly, the efficiency stopped around 80.8. The grid independence study shows that a volume mesh with 0.50 mm base size value has the same accuracy as the refined volume mesh at base size 0.35 mm and 0.25 mm.

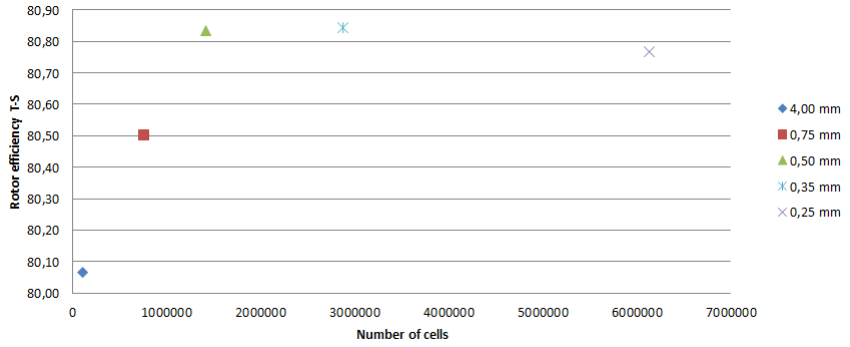

Figure 4.2: The Grid Independence study was performed on geometry one with different base size values. The study shows that the selected standard base size value at 0.5mm gave good accuracy.

4.4 Accuracy between geometry one and geometry two

Because of the encountered convergence problem with geometry one at interval point two and three, it was necessary to design a new geometry with a new outlet region. Geometry two and three was designed with a stationary and extended outlet region according to figure 4.1. Because of the change, the two geometries were needed to be compared. The two geometries were tested with the reference turbine Model A at design point one and standard continua physics. Table 4.3 shows the results of the total to static efficiency of the rotor and state that geometry one and two have the same accuracy.

Table 4.3: The difference in rotor total to static efficiency between geometry one and geometry two at design point one with standard continua physics.

Geometry one	80,83	η_{TS}
Geometry two	80,79	η_{TS}

4.5 Sensitivity study

Even if the standard continua physics at Volvo were chosen, segregated solver with $k-\epsilon$ turbulence model, it was interesting to evaluate the difference in efficiency between solvers and turbulence models. These options are often discussed in articles and it is appropriate to compare them to known if they calculate the efficiency differently. Table 4.3 show the difference in total to static efficiency of the rotor and states that the difference is within one percent.

Table 4.4: Describes the difference in rotor total to static efficiency between different solvers and turbulence models for the reference model A with geometry one.

Standard	80.8	η_{TS}
Coupled solver with $k-\epsilon$	81.5	η_{TS}
Segregated solver with $SSTk-\omega$	81.7	η_{TS}

4.6 Mesh quality

There are several ways of determining the overall quality of the volume mesh in STARCCM+. The most common are: Face Validity, Volume Change and Cell Skewness Angle [10].
Face Validity measure if the face normals point outwards, away from the cell centroid. If the cell has bad face validity, one or more cell face normals points inward. This is indicated by a value below one.
Volume Change measures the ratio of the volume for one cell compared to its largest neighbour. If the Volume Change indicates 1, then the cell has the same volume as its neighbour. A Volume Change at 0.01 or lower is considered as a bad cells.
Cell Skewness Angle is the measure of the angle between a face normal and the line between two cell centroids. If the skewness angle is below 85 degrees then the cell are considered as a bad cell.
The Face Validity, Volume Change and Cell Skewness Angle can be displayed with the mesh diagnostic tool in STAR-CCM+. Consider Appendix B for an example. Each geometry was evaluated with the mesh diagnostic test before each calculation in STAR-CCM+ to ensure the accuracy between the models.

Chapter 5

Results and Discussion

The result is divided into two parts. First design step includes reference rotor A and the scalloped models B-F. The second design step includes a new design of the reference rotor A which is compared again with the scalloped models B-F. The second design step was performed to remove any kind of measurement error between the models.

5.1 First design step - Rotor models A-F

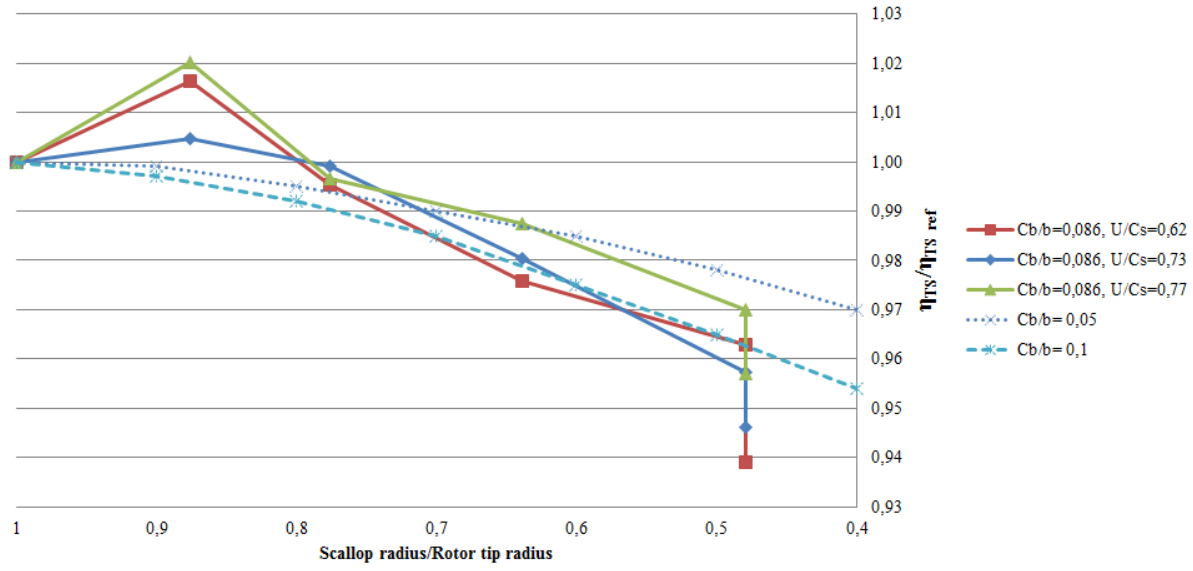

Figure 5.1: Shows the result of the reference rotor A to the deeply scalloped models E and F at 0.48 scallop/rotor tip ratio. The two lines C_b/b at 0.05 and 0.1 are the same as in figure 1.2.

Figure 5.1 shows how the efficiency increases and decreases when scalloping is introduced. The diagram shows a quite large difference between the non-scalloped rotor, reference model A, and the lightly scalloped model B. From this point of view it seems that a light scalloped rotor would be preferable with high efficiency. One question arise, is this something significant for only this tested mixed-flow rotor? Furthermore, the diagram also indicates that it is preferable to scallop even further down to 0.8 scallop/rotor tip radius ratio and still have the same efficiency as the reference rotor and a decrease of inertia to approximately 13 %.

According to figure 5.2, the relative vector flow field through the rotor is changing when the distance to the surfaces is decreasing. This clearly shows the no-slip condition at the surface were the velocity should be zero. When the distance increases from the surface, the relative vector flow field becomes more

Table 5.1: The moment of inertia and ratio of scallop and rotor tip radius.

Model	$\Delta Inertia$ %	$\frac{Scallop}{Rotor\ tip}$
A	0	1
B	-6.53	0.88
C	-13.22	0.78
D	-20.33	0.64
E	-30.19	0.48
F	-35.27	0.48

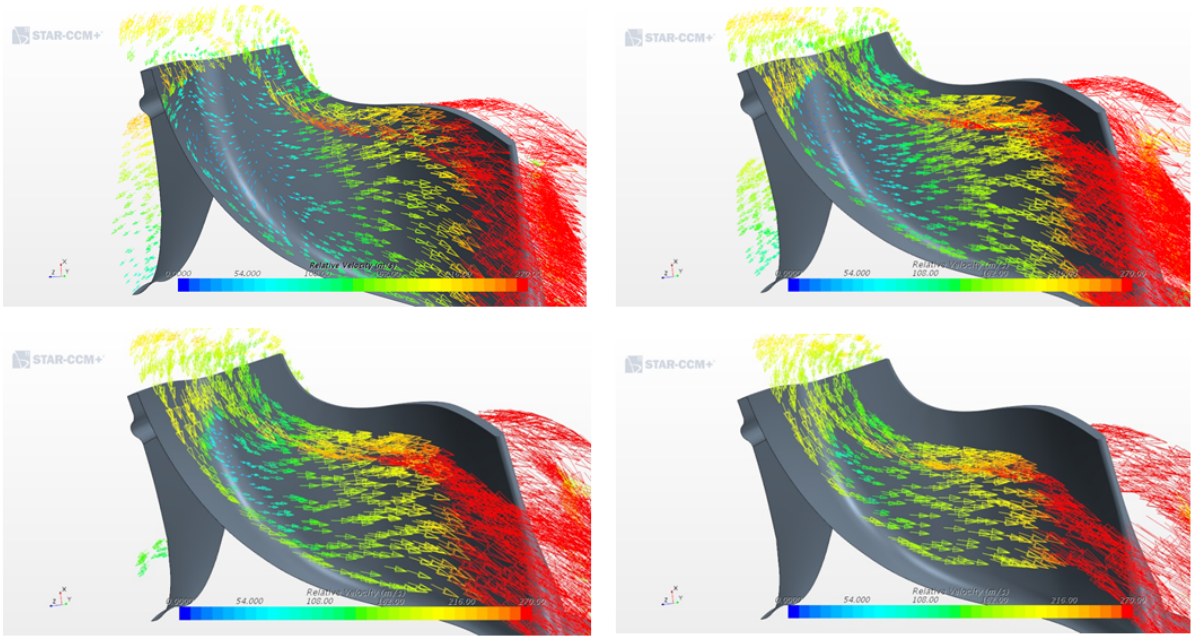

Figure 5.2: Model A at design point 1 with relative velocity vectors 1-4 millimetre from the surface. The relative flow field changes when the distance from the surface increases. From disruptive at the pressure side to a smoother flow field at mid-passage

even in the blade passage, consider the pictures in the figure 5.2. This appearance is the same for all the models but for Model B the relative velocity flow at 1 millimetre is more smooth after it hits the scalloped leading edge. It seems from the figures 5.3, 5.5 and 5.7 that the sharp edge at Model A is introducing a disturbance in the flow field compared to 5.4, 5.6 and 5.8. Therefore, is Model A desiged with a rounding for a better comparison to Model B-F in the next design step.

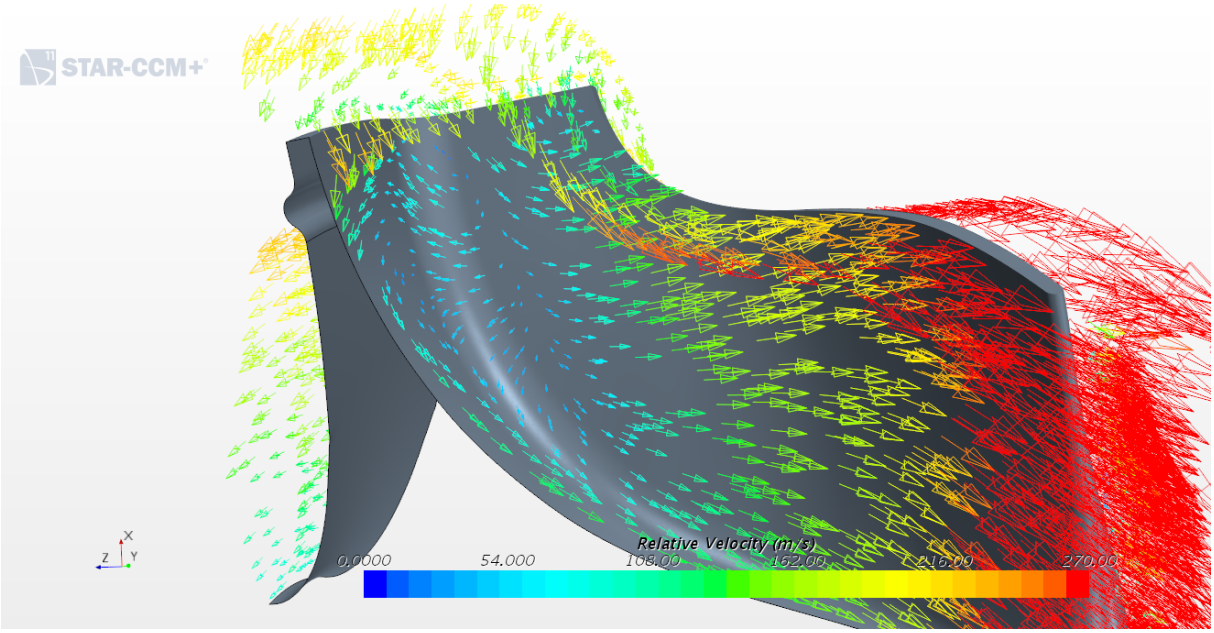

Figure 5.3: Model A at design point 1 with relative velocity vectors 1 millimetre from the surface

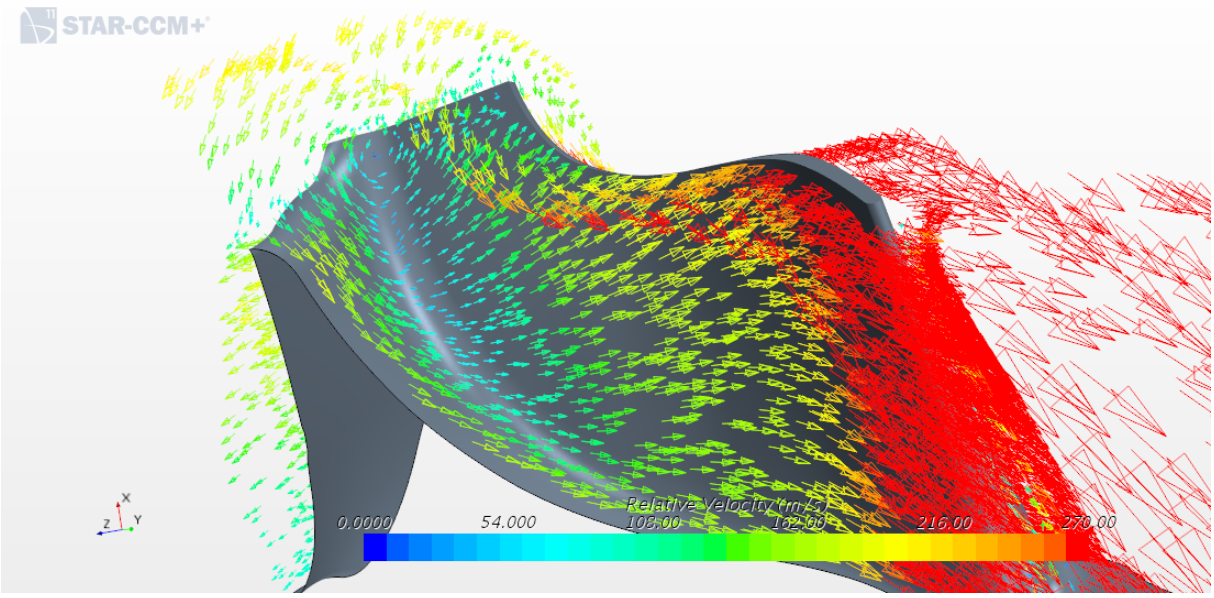

Figure 5.4: Model B at design point 1 with relative velocity vectors 1 millimetre from the surface

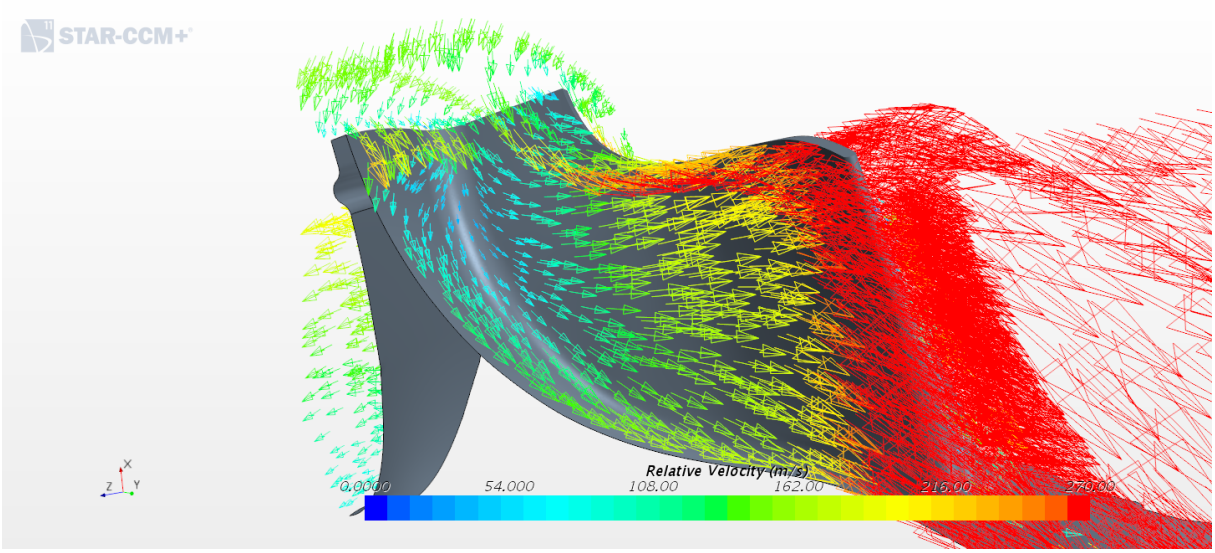

Figure 5.5: Model A at interval point 2 with relative velocity vectors 1 millimetre from the surface

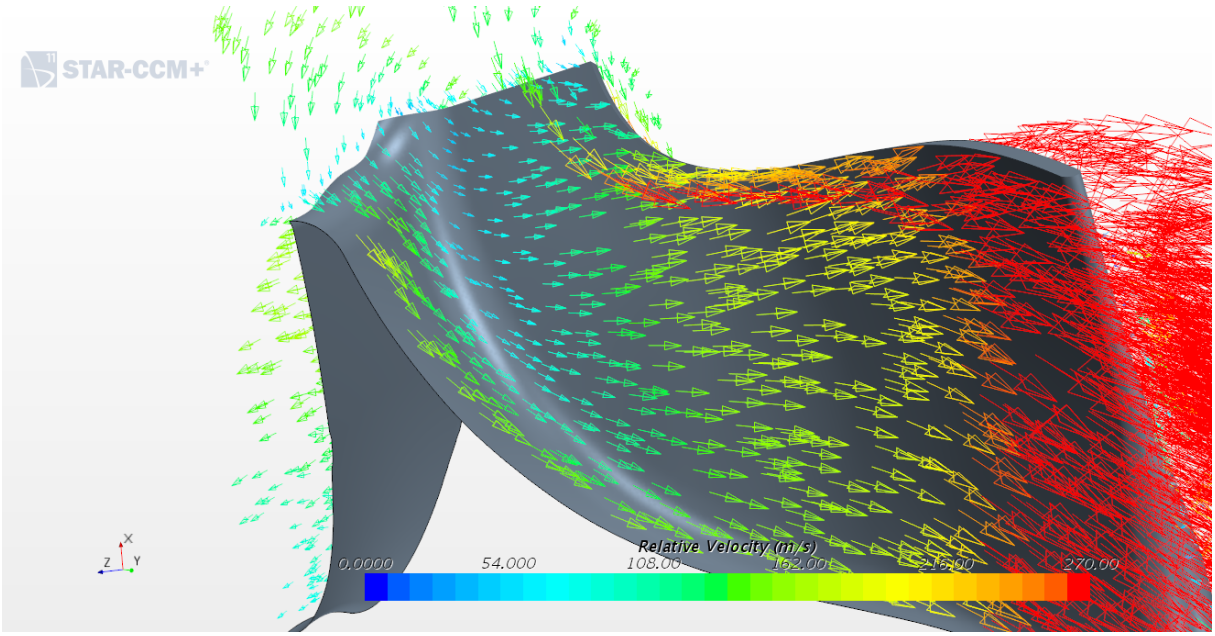

Figure 5.6: Model B at interval point 2 with relative velocity vectors 1 millimetre from the surface

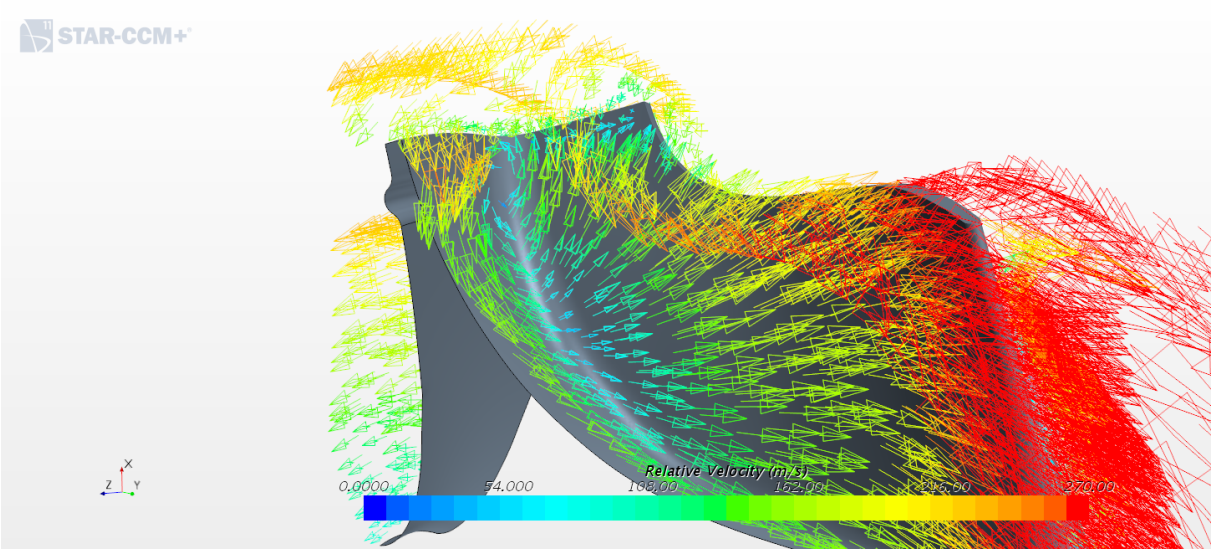

Figure 5.7: Model A at interval point 3 with relative velocity vectors 1 millimetre from the surface

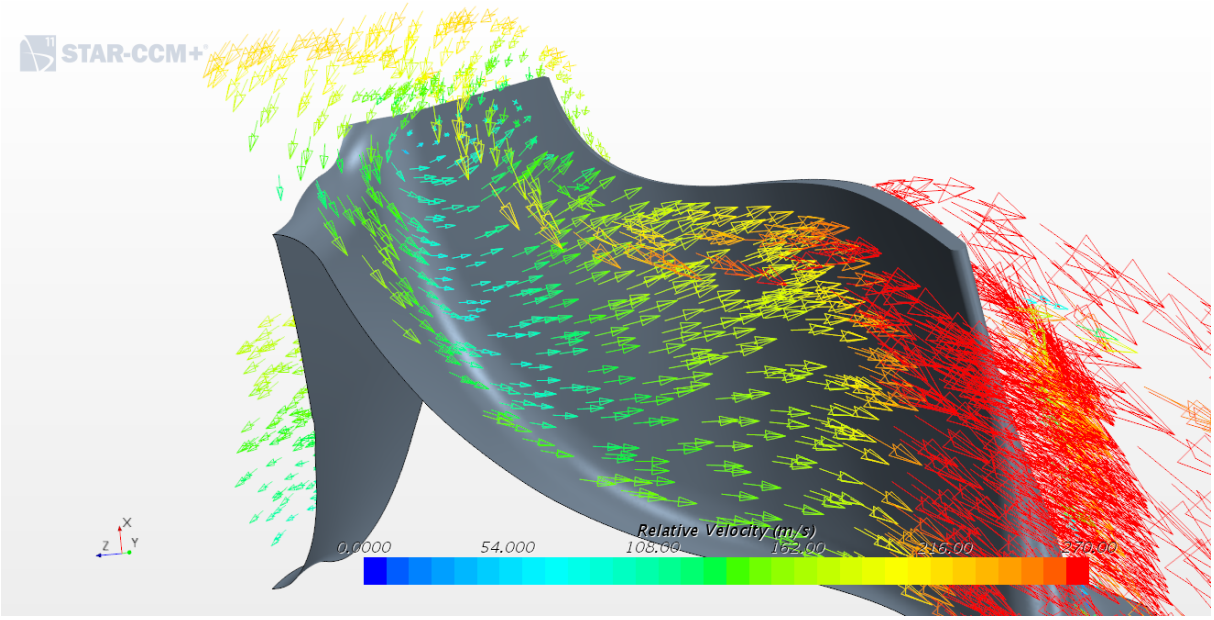

Figure 5.8: Model B at interval point 3 with relative velocity vectors 1 millimetre from the surface

5.2 Second design step - New design of the reference rotor A

The second design step was performed because of the large difference between Model A and B in the previous results. The disturbance of the flow field seemed possible to improve, and the outcome was a new design of the reference rotor. Figure 5.9 shows the results of total to static efficiency for each model

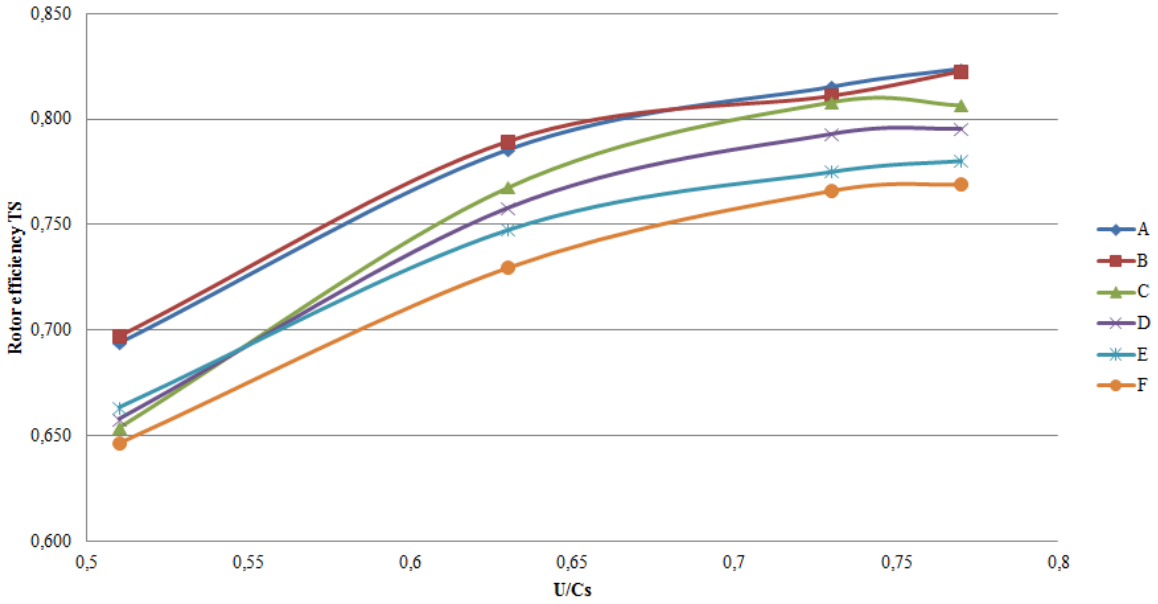

Figure 5.9: The result of Total to Static efficiency for the rotor models at different velocity ratios.

A to F. The results shows that the new reference model A and model B has almost the same performance. Furthermore, the best performance occurs around 0,74 to 0.75 U/C_s.

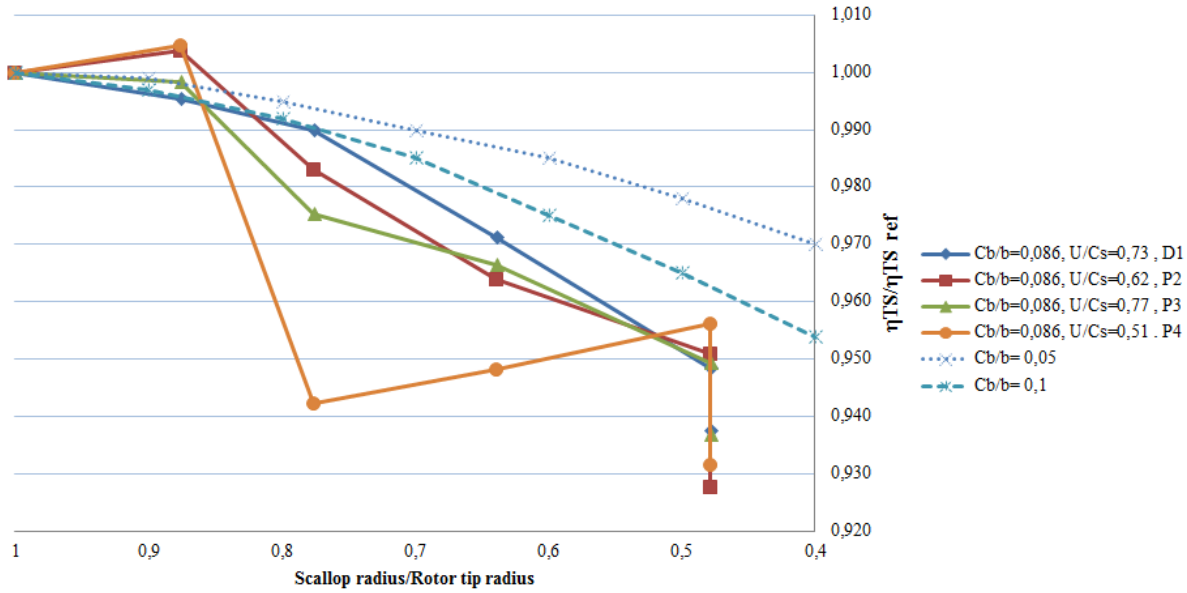

Figure 5.10: Shows the result of the new designed reference rotor A to the deeply scalloped models E and F at 0.48 scallop/rotor tip ratio. The two lines C_b/b at 0.05 and 0.1 is the same as in figure 1.2.

Figure 5.10 shows the results of the new designed reference rotor model A with previous models B-F. With the new design of Model A has now the difference decreased towards model B.

Table 5.2: New result of the moment of inertia and ratio of scallop and rotor tip radius

Model	$\Delta Inertia$ %	$\frac{Scallop}{Rotor\ tip}$
New Design A	0	1
B	-6.26	0.88
C	-12.97	0.78
D	-20.10	0.64
E	-29.99	0.48
F	-35.08	0.48

The efficiency has been improved with the new design, figure 5.11, of the reference rotor model A. According to figure 5.12 and 5.13 has the disturbance of the flow field decreased. However, it seems that a rotor with light scallop as model B would still be comparable to the new design of rotor model A. The benefit is then, a small decrease in inertia to 6.26 % close to the same efficiency as the new design of reference rotor A. According to the result in figure

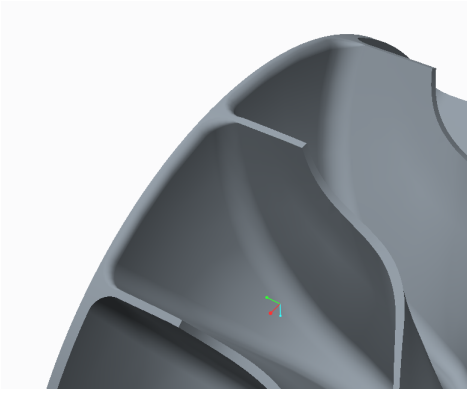

Figure 5.11: New design of reference rotor model A with a more smooth edge on the back-face of the rotor. In this figure the rounding of the edge is only performed between one blade. Consider the sharp edge to the left in the picture to see the difference.

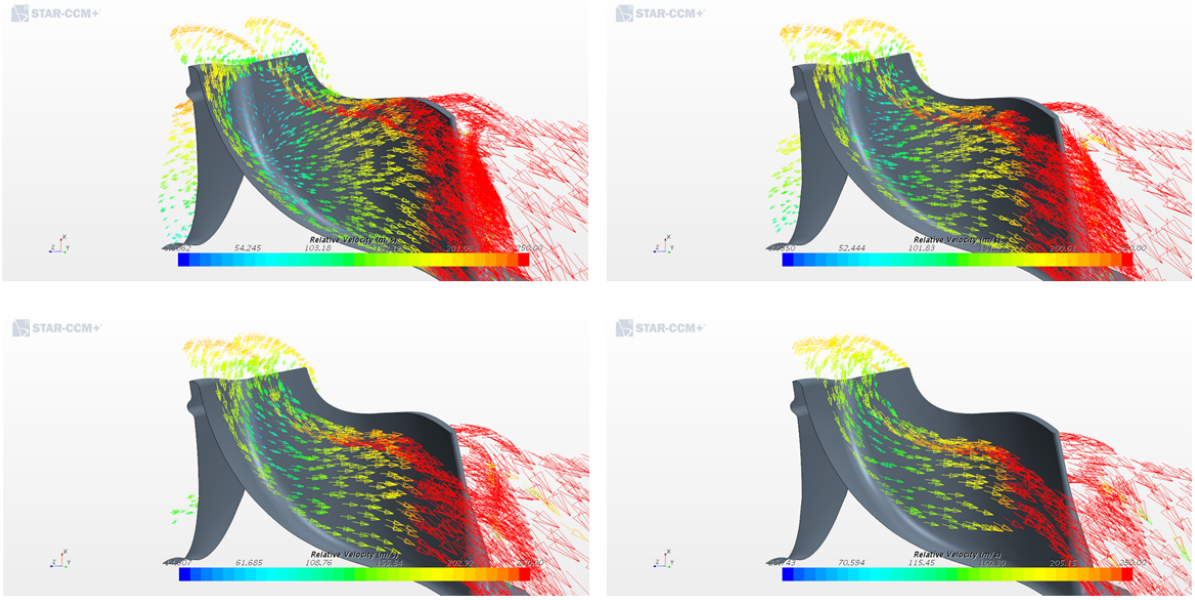

Figure 5.12: Overview of the relative velocity vectors from 1 millimetre to 4 millimetre

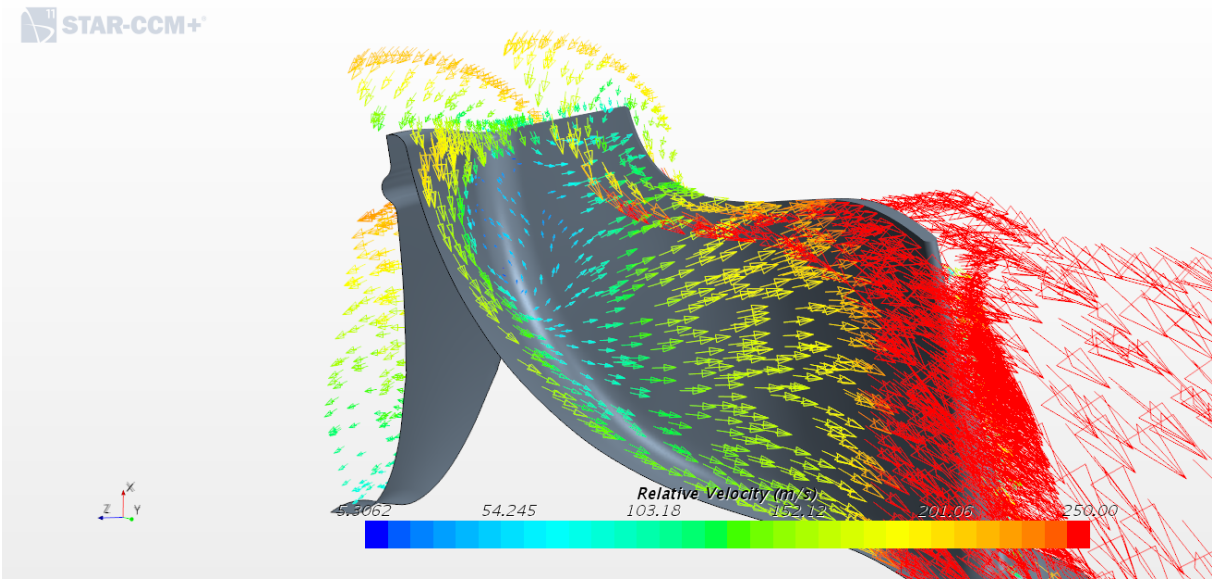

Figure 5.13: New design of Model A at design point 1 with relative velocity vectors 1 millimetre from the surface

5.3 Comparison between Model E and Model F, deeply scalloped rotor with different width of the back-face rotor blade

The model E and F has the same scalloping radius equals to 0.48 millimetre, but the difference was the width of the back-face blade. This study was done to investigate how the efficiency would change with the back-face width. Previous results, figure 5.10, showed the decrease in efficiency for model E and F at the design and interval points (velocity ratios U/C_s). For the whole interval, between 0.62 and 0.77, Model E decreased with 5% in efficiency. Model F decreased with additional 1.2% points in efficiency for 0.73-0.77 U/C_s. And for the interval point with high aerodynamic loading (low U/C_s=0.62) the efficiency decreases to 0.928.

The figures 5.14, 5.15, 5.16 and 5.17 shows the static pressure distribution on the pressure and suction side of Model F and E. The selected scalar field has been chosen only to show the selected interval, the interval has cut-off the values above and below the indicated values. This action does not display the whole rotor but indicates the difference better compared to increase the pressure interval on the same colour scale. Now the areas with pressure below or above are indicated with a non-coloured area. Consider figure 5.16 and 5.17 where the pressure close to the hub of model E is indicated with a hole. The static pressure figures indicate that the pressure is increased on the back-face of the rotor when the width of the blade back-face is decreased. The pressure distribution on the pressure side is uniform from the tip and down to the half of the rotor. Below the half of the rotor and on the back-face close to the hub area the pressure is higher for Model F according to figure 5.14. This indicates a leakage from the pressure to the suction side. However, it is quite difficult to evaluate by only consider the static pressure, next results show another way investigate the pressure leakage.

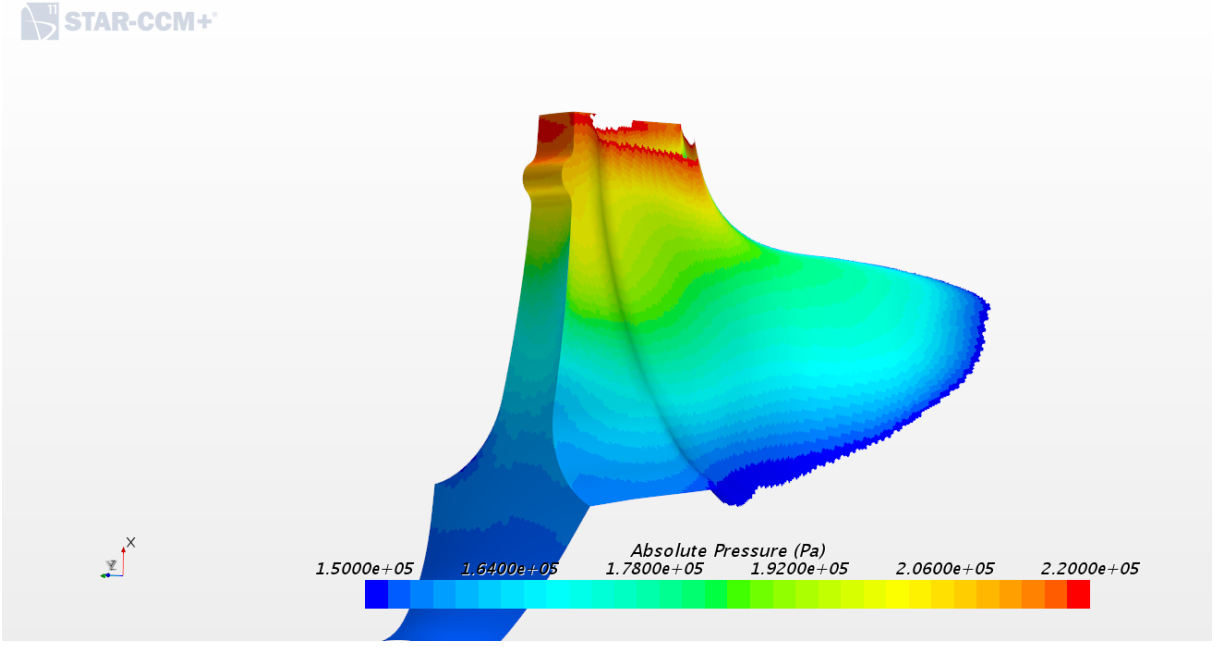

Figure 5.14: Static Pressure distribution on Model F at design point 1.

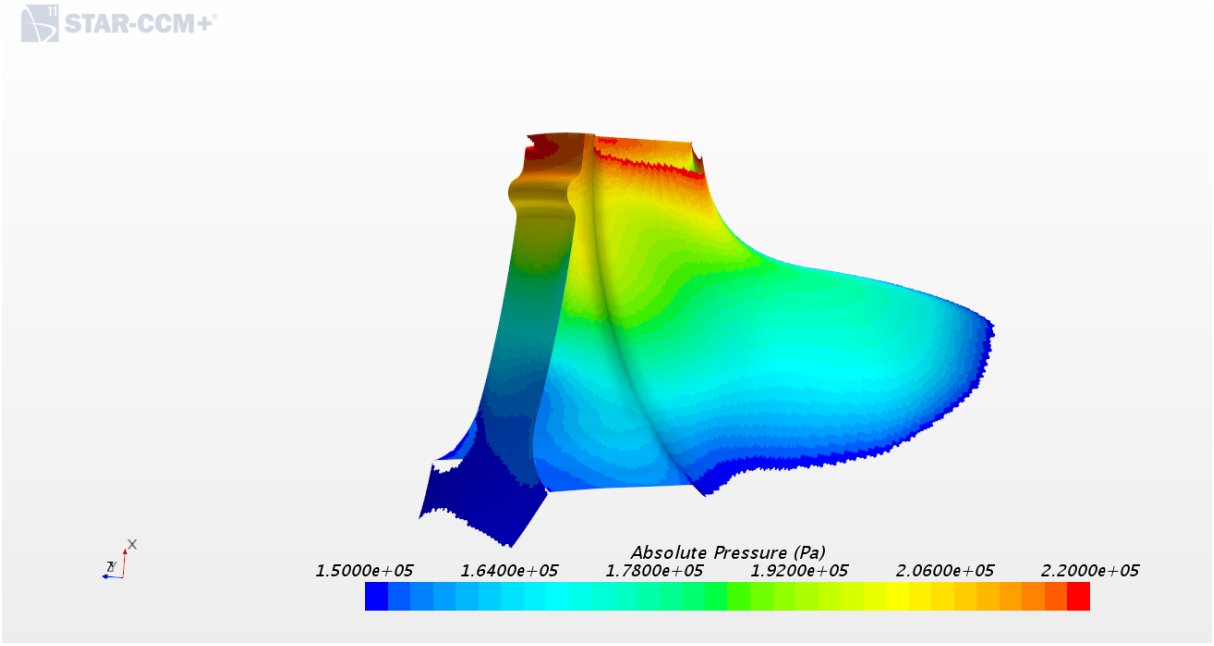

Figure 5.15: Static Pressure distribution on Model E at design point 1.

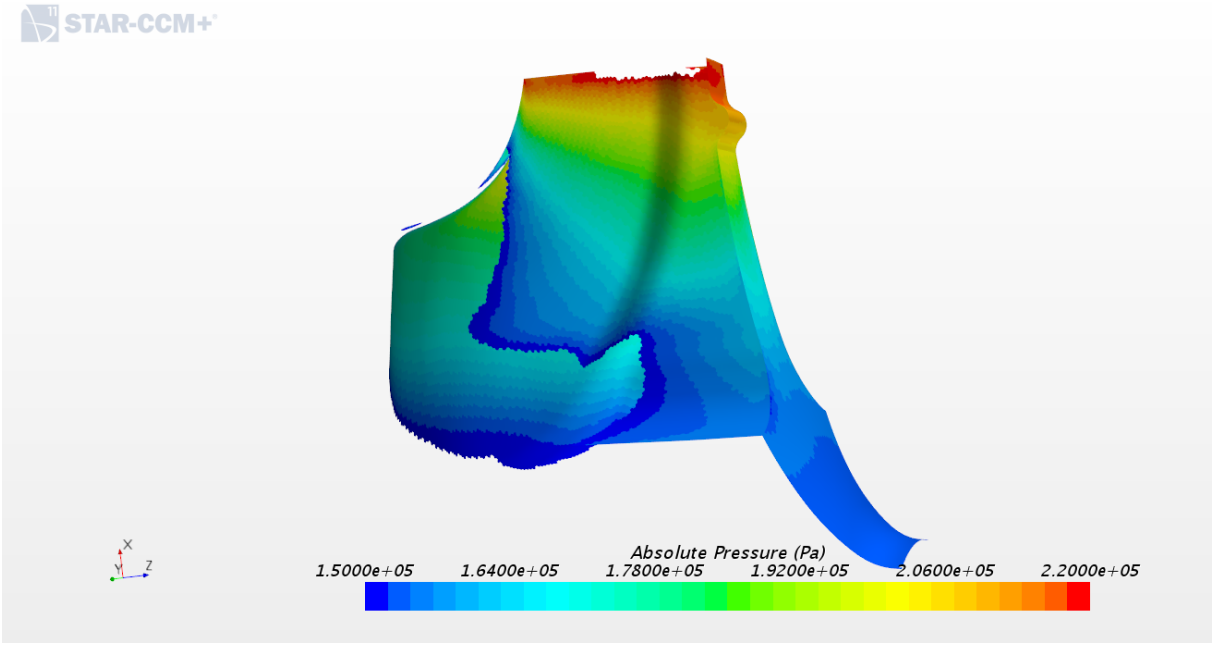

Figure 5.16: Static Pressure distribution on Model F at design point 1.

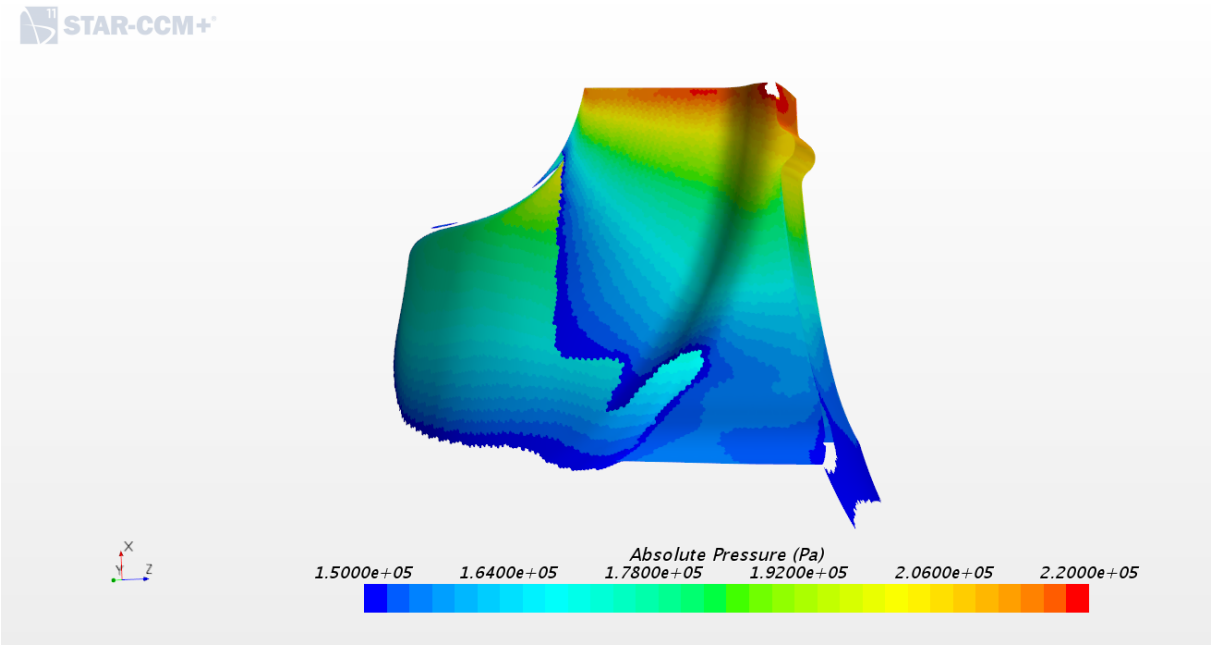

Figure 5.17: Static Pressure distribution on Model E at design point 1.

5.4 Results: Vorticity

To capture the flow through the turbine different post-processing alternatives were evaluated, consider appendix C. The main goal was to capture the generated vortexes created by the incidence angle, leakage behind the scalloped back-face and tip clearance leakage. By creating planes tangential to the streamlines through the turbine and selecting the vorticity magnitude, where it possible to evaluate the pattern of the flow field. The vorticity magnitude shows the sum of the vorticity in axial, radial and tangential. The figure 5.18 shows the radial blade and the section planes. In the figures for each velocity ratios (0.77-0.51) the radial blade is hidden and it is possible to overview each side of the blade, suction side and pressure side. The main stream flow pattern is evaluated for each velocity ratio and rotor model. The new design of Model A is in this section referred only as Model A.

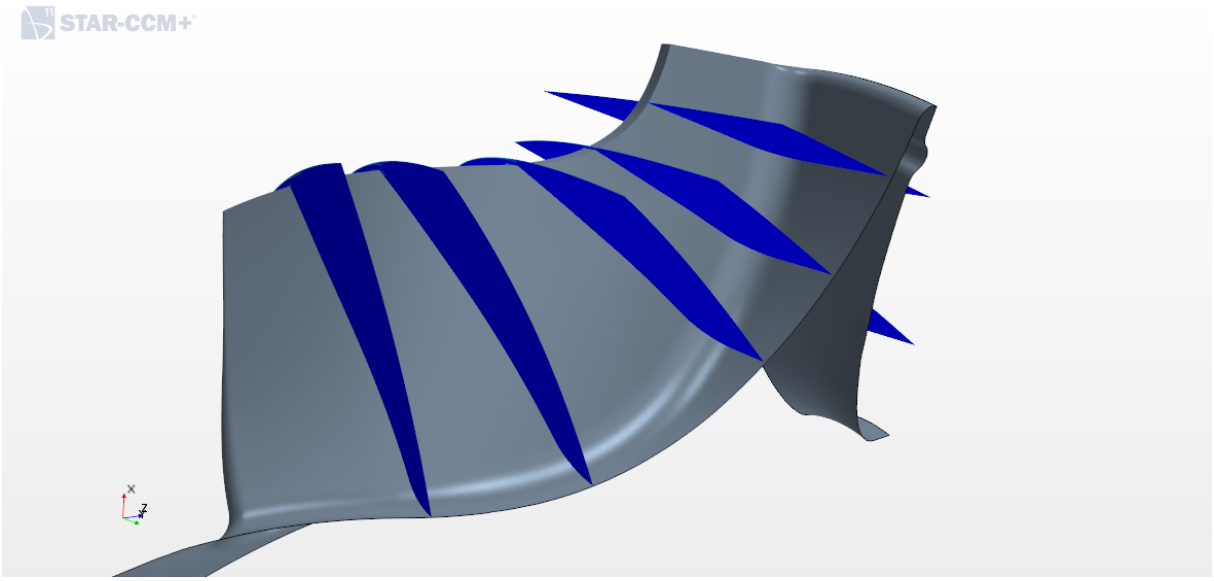

Figure 5.18: Model A with the sections planes to overview the blades, the figure shows the suction side.

5.4.1 U/Cs=0.77

At Model A, figure 5.19, the incidence angle seems to generate some small disturbance at pressure side at the inlet section plane. This is indicated as green with vorticity magnitude around 50 000. The tip clearance leakage is quite dominant and is increased and separated into two vortexes. The same pattern is generated for Model B to F. At Model B, figure 5.20, the same green field is now increased and a red dot can be seen at the inlet on the pressure side. The vortex propagates from inlet to exit and is located in the blade passage. Moving on to Model C, figure 5.21, this rotor has a slightly increased incidence vortex compared to Model B and as mention before the tip clearance leakage is still in the same magnitude. The most remarkable with Model C is the red area (vortex) generated between back-face of the blade and on the suction side at inlet section plane. The section plane also indicates the scalloped rotor, compare with Model B. The red area seems to decrease after the first section plane and can not be seen at the second plane. With increased scalloping at Model D, figure 5.22, the scalloping is now generating a small vortex at the hub on the suction side. Model E and F, figures 5.23 and 5.24, shows increased incidence vortexes, and a disturbance generated at the second section plane from inlet. The disturbance is increased and moves upwards when it propagates through the turbine.

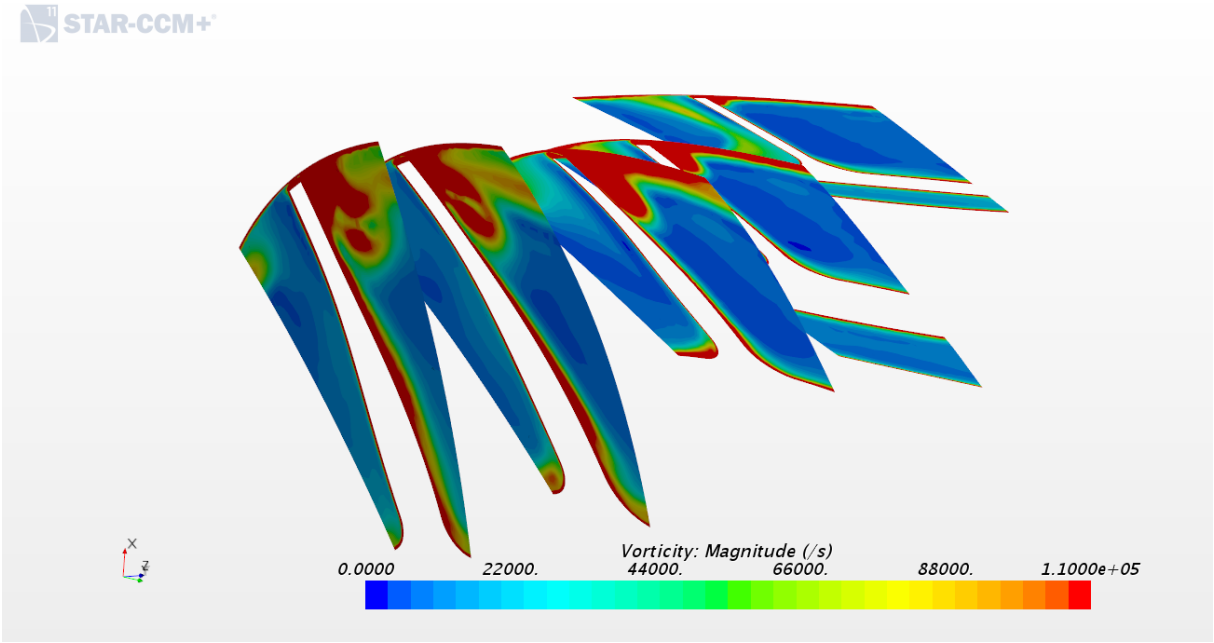

Figure 5.19: Model A at U/Cs equals 0.77

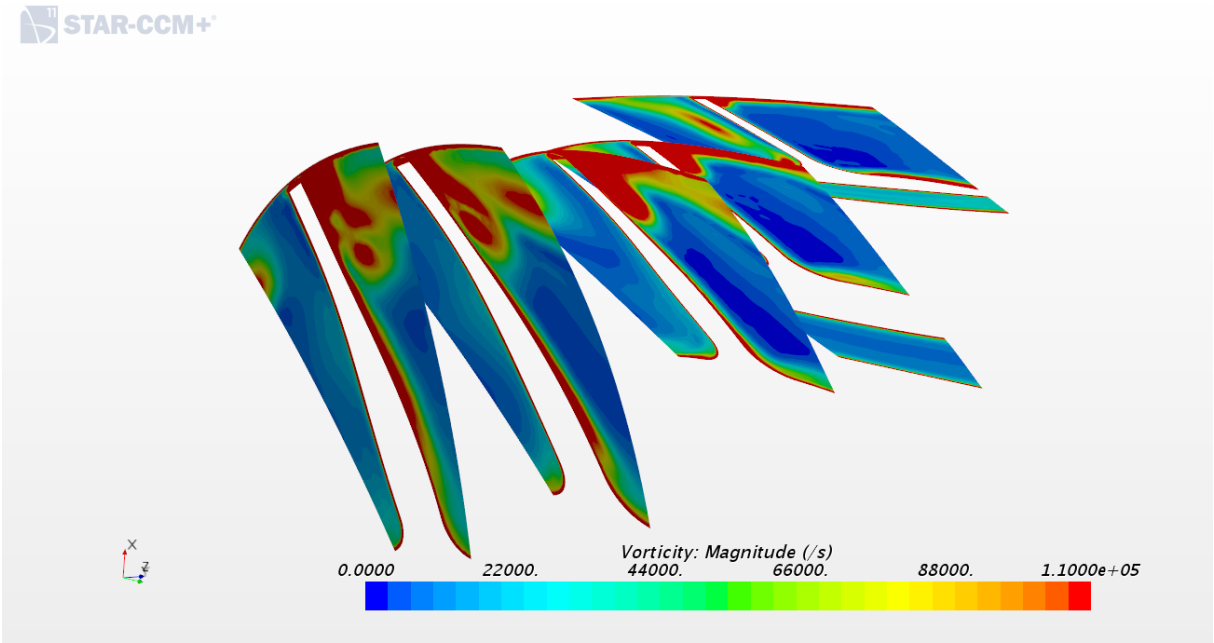

Figure 5.20: Model B at U/Cs equals 0.77

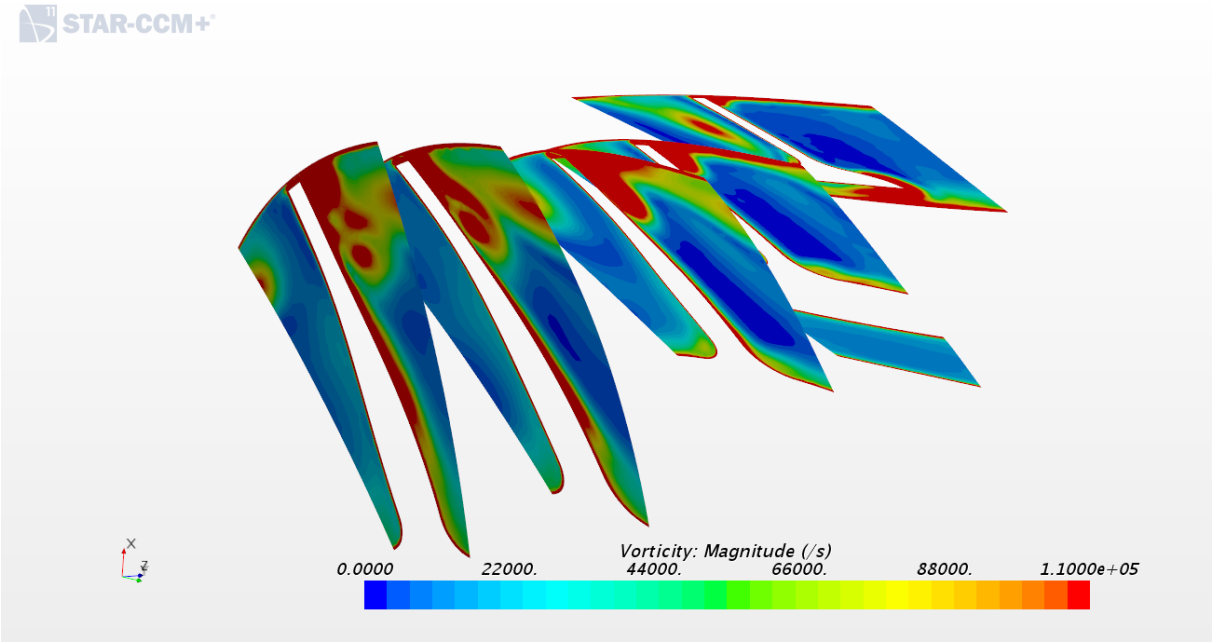

Figure 5.21: Model C at U/Cs equals 0.77

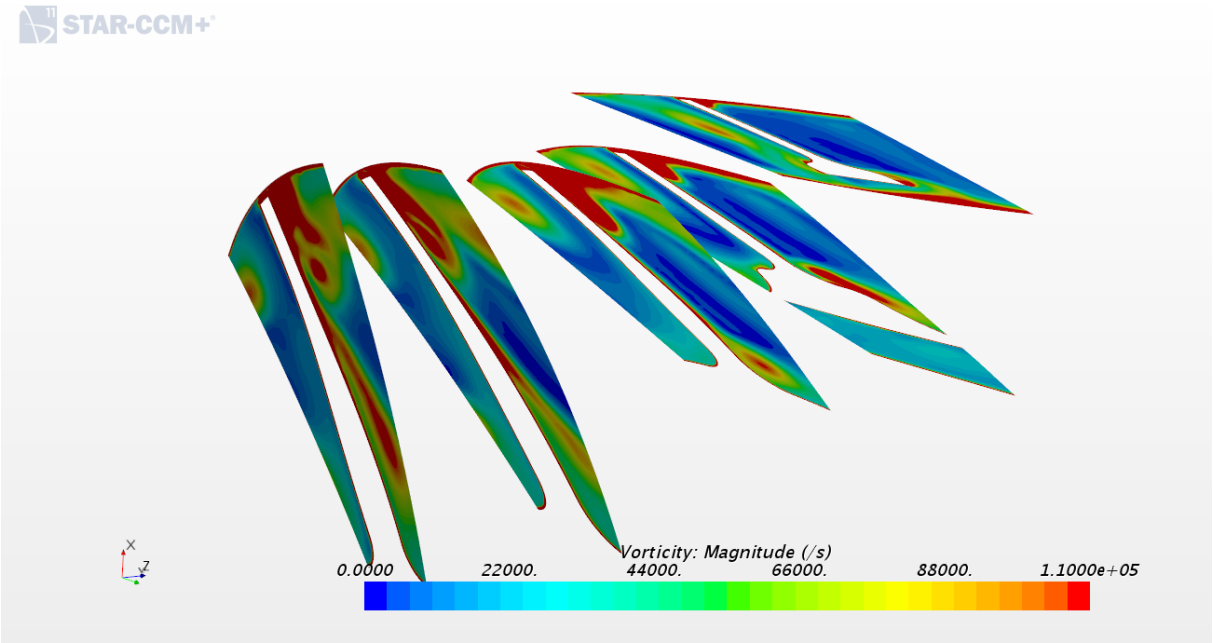

Figure 5.22: Model D at U/Cs equals 0.77

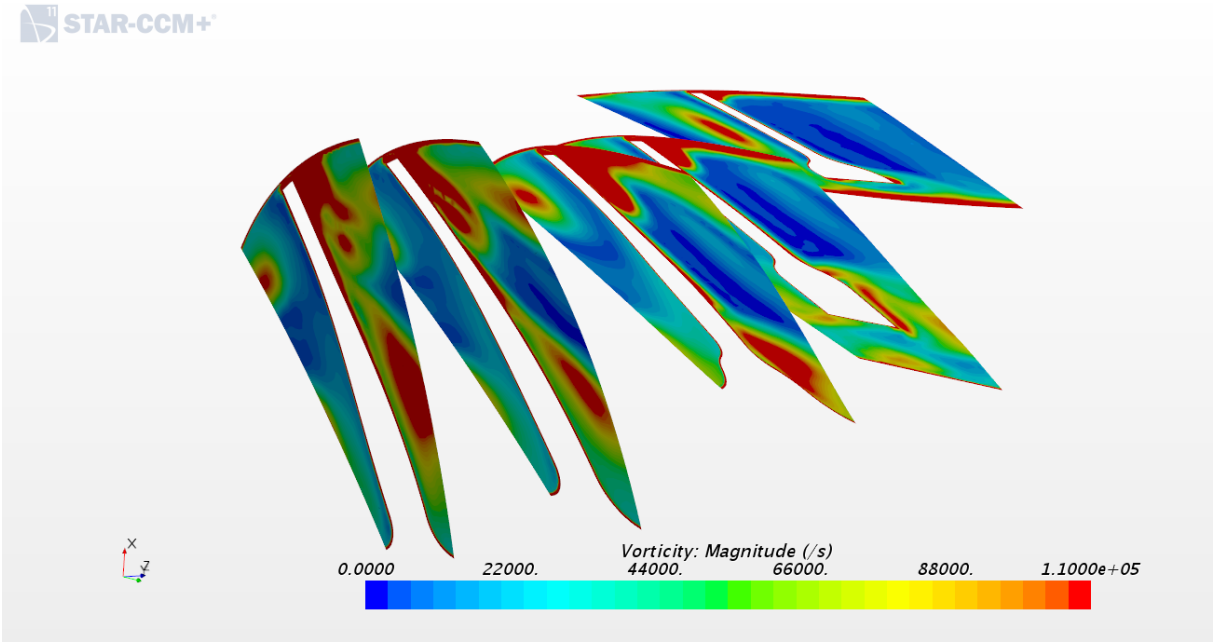

Figure 5.23: Model E at U/Cs equals 0.77

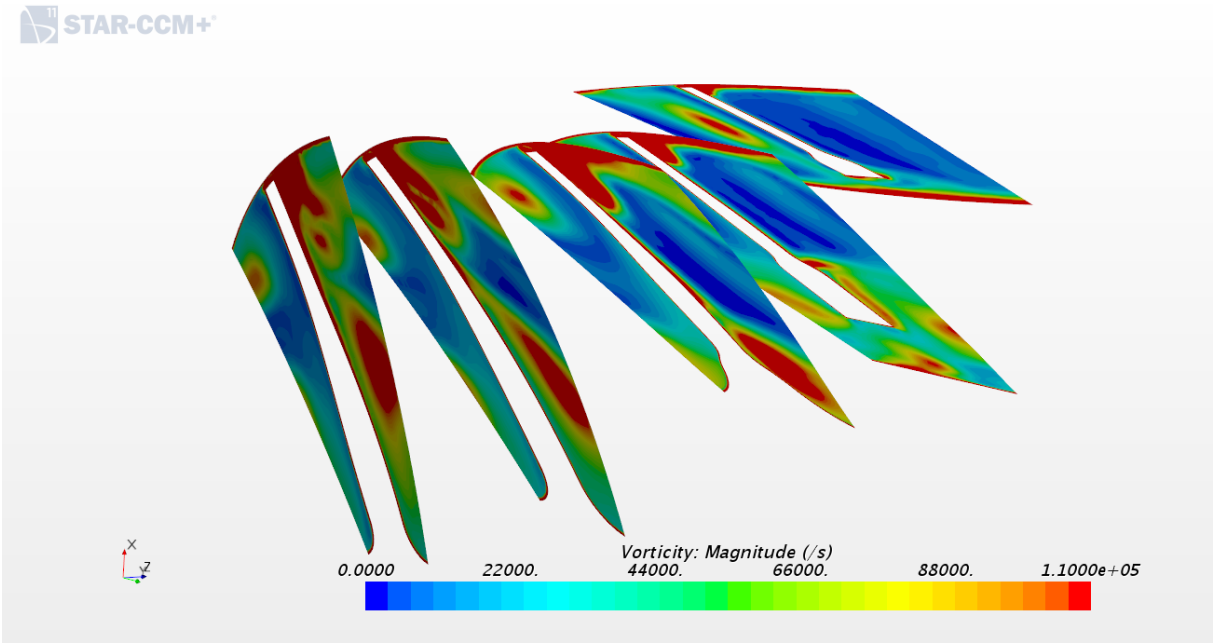

Figure 5.24: Model F at U/Cs equals 0.77

5.4.2 U/Cs=0.73

At design point with velocity ratio 0.73, Model A, figure 5.25, seems to have clean main stream flow through the rotor. Low incidence disturbance at inlet but some tip clearance leakage. Model B, figure 5.26, has some incidence disturbance at pressure side and the magnitude is the same for Model C, figure 5.27. Model C show the same behaviour again as it did at velocity ratio 0.77 with a small disturbance at the inlet section plane. For Model D, figure 5.28, a leakage is increasing from pressure to suction side and generate a vortex which can be seen at section plane two. Model E and F, figure 5.29 and 5.30, show larger incidence disturbance than previous models A, B, C and D. The same pattern as velocity ratio 0.77 is present and a large vortex is generated at the suction side and propagates towards the exit.

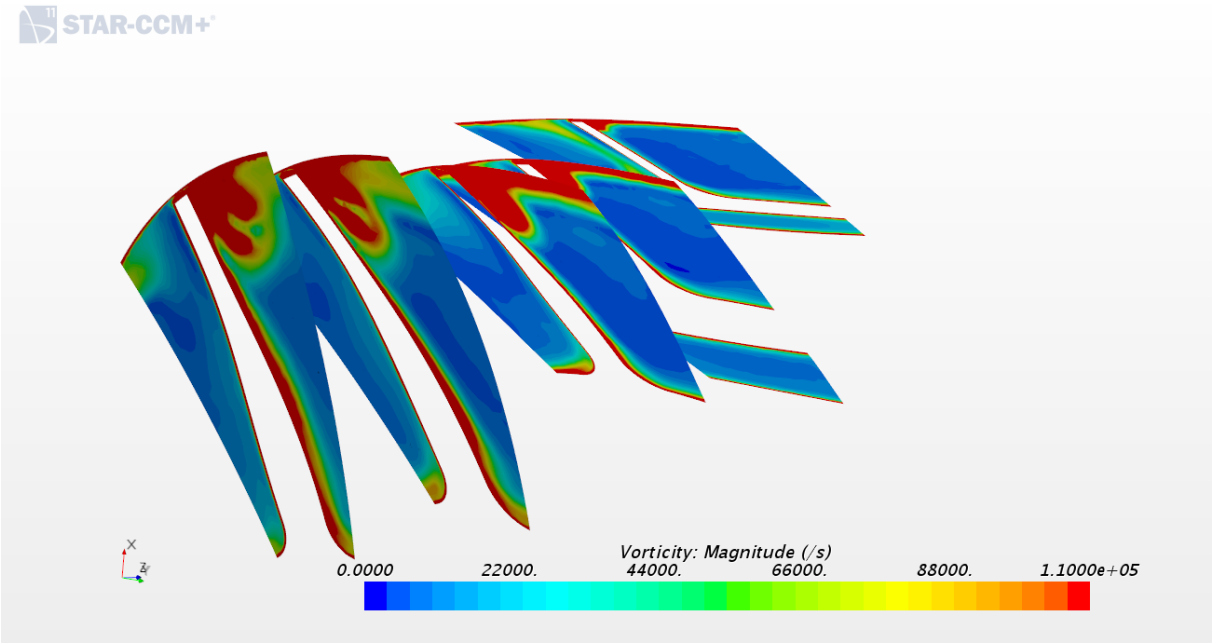

Figure 5.25: Model A at U/Cs equals 0.73

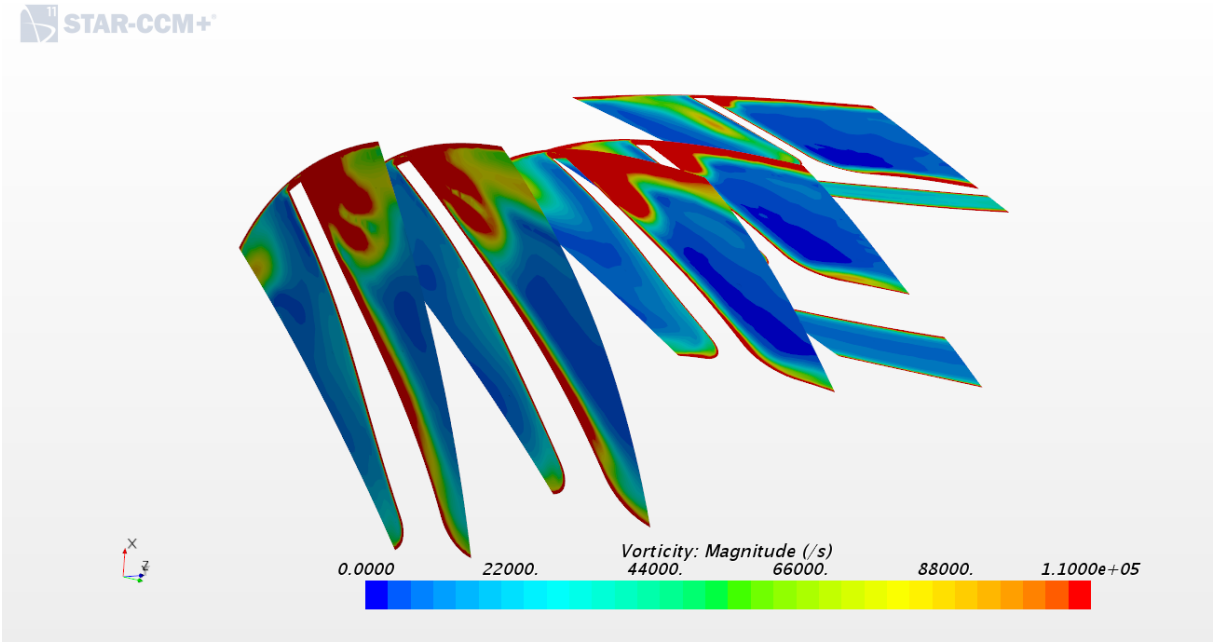

Figure 5.26: Model B at U/Cs equals 0.73

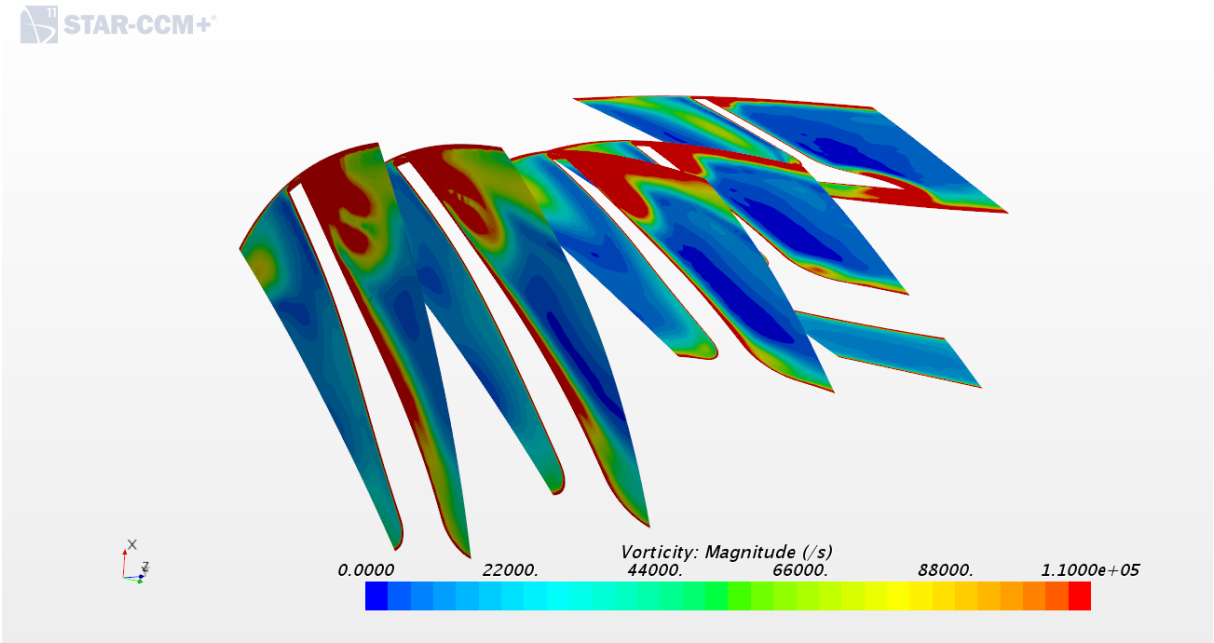

Figure 5.27: Model C at U/Cs equals 0.73

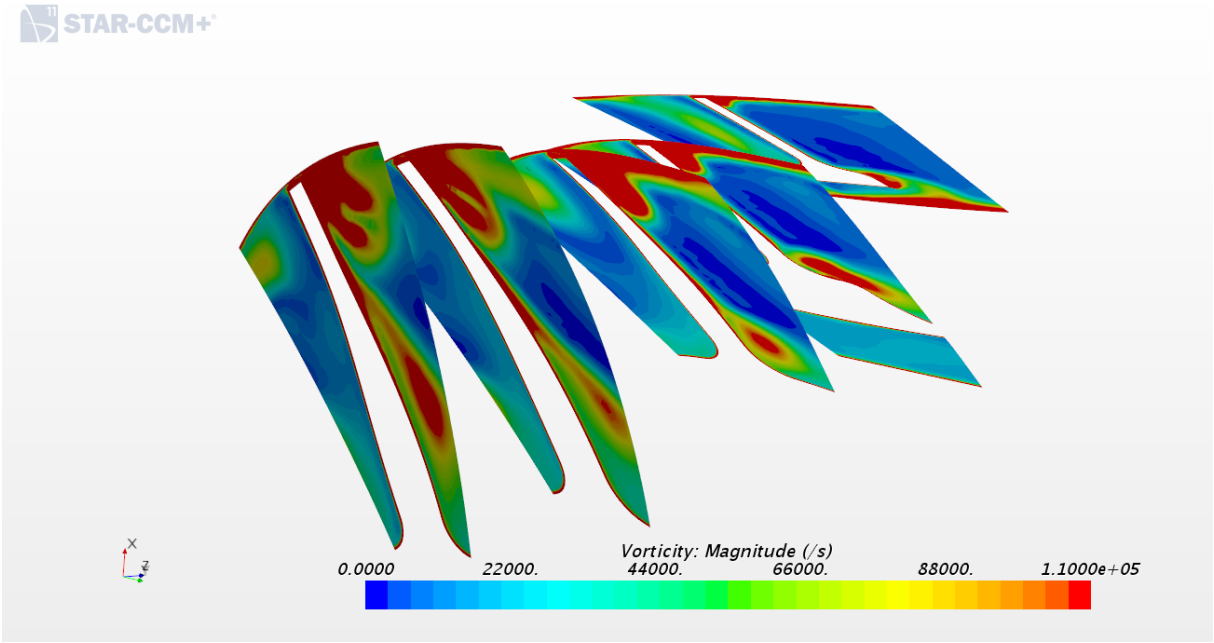

Figure 5.28: Model D at U/Cs equals 0.73

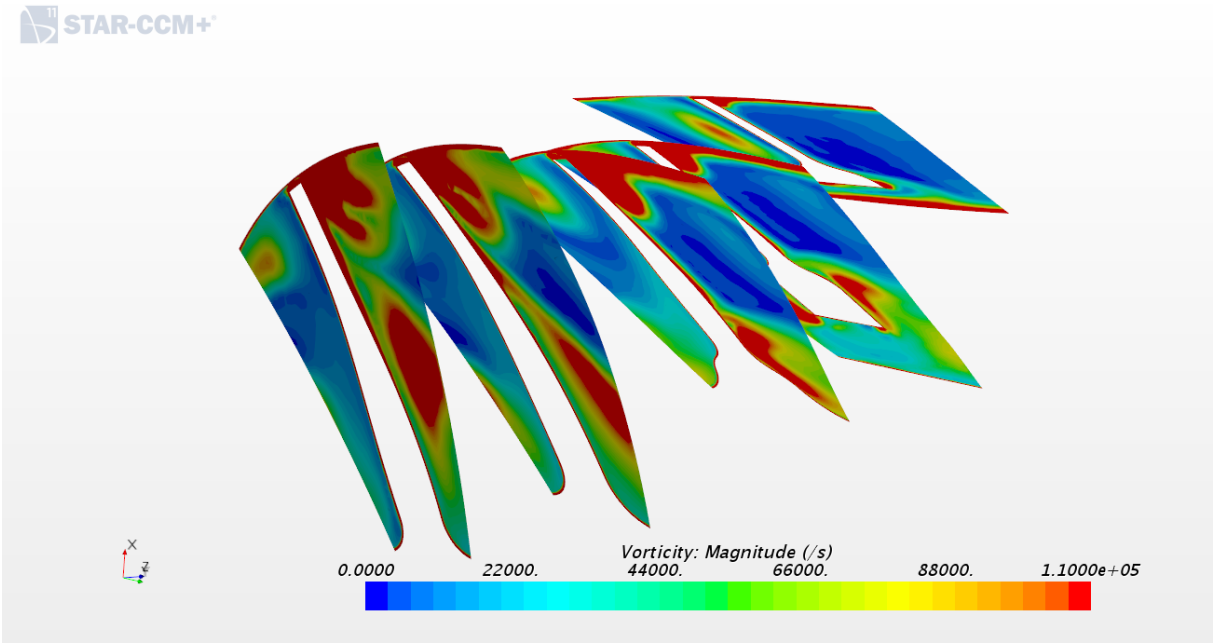

Figure 5.29: Model E at U/Cs equals 0.73

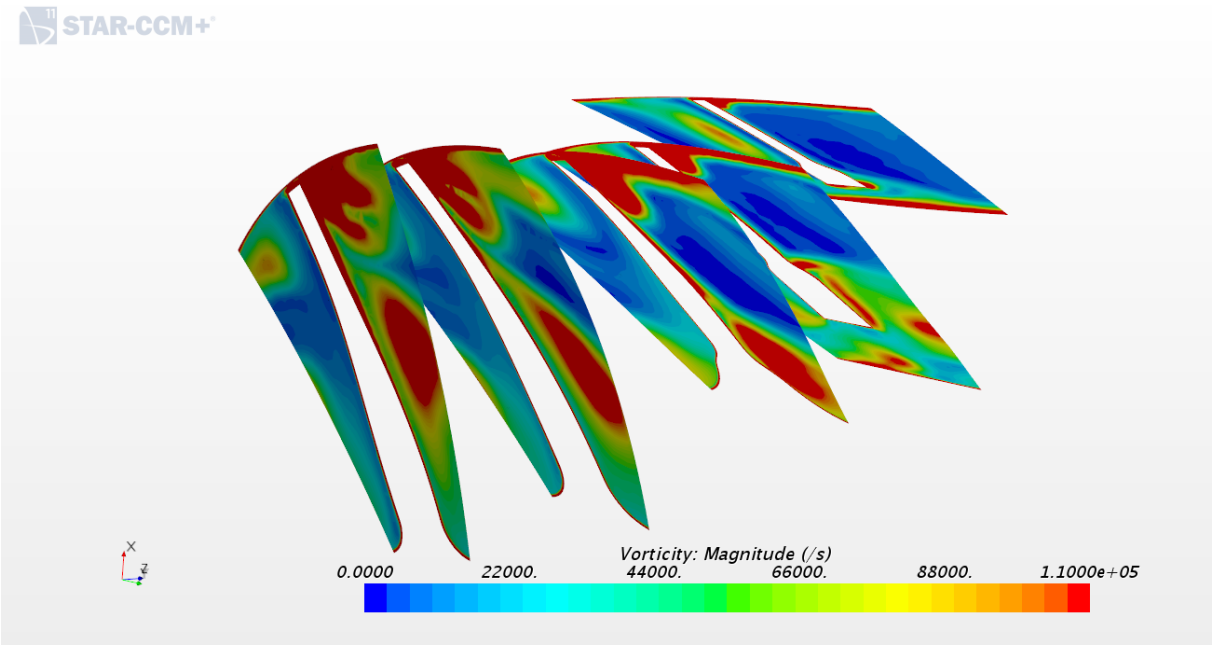

Figure 5.30: Model F at U/Cs equals 0.73

5.4.3 U/Cs=0.63

At velocity ratio 0.63 Model A and B, figure 5.31 and 5.32, seems equal and tip clearance leakage is the dominate loss source. However, at Model C, figure 5.33, the same disturbance as seen at velocity ratio 0.77 and 0.73 is present. But at this time it propagates through the turbine at suction side and moves upward. The same behaviour remain and increases for Model D, E and F, figure 5.34 5.35 5.36.

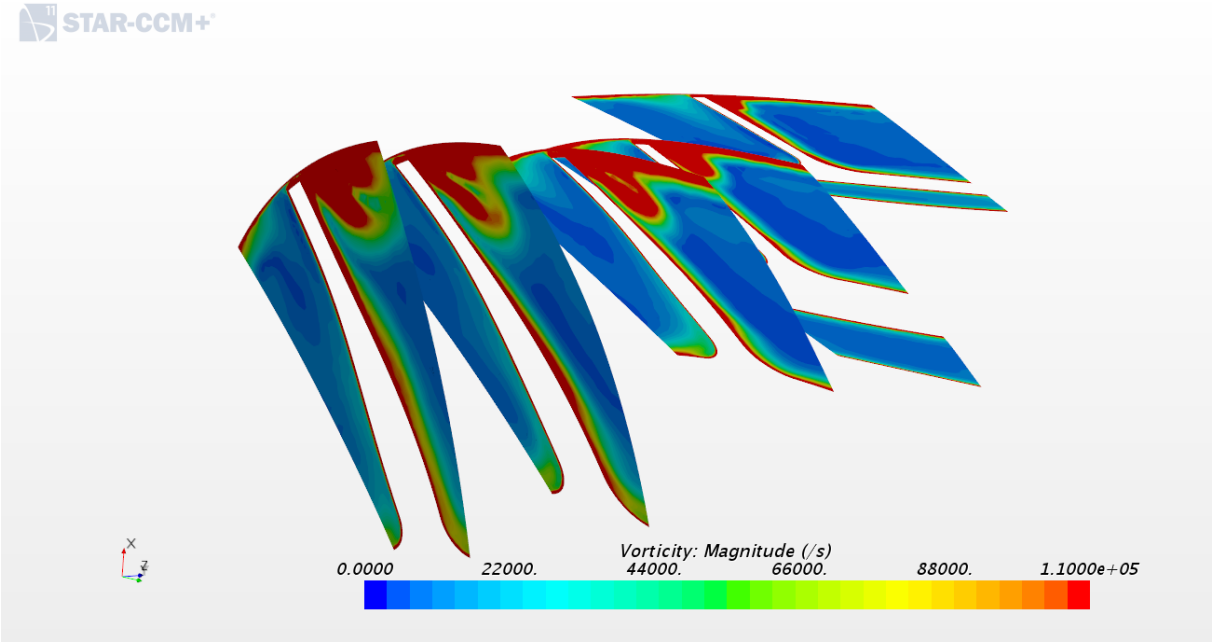

Figure 5.31: Model A at U/Cs equals 0.63

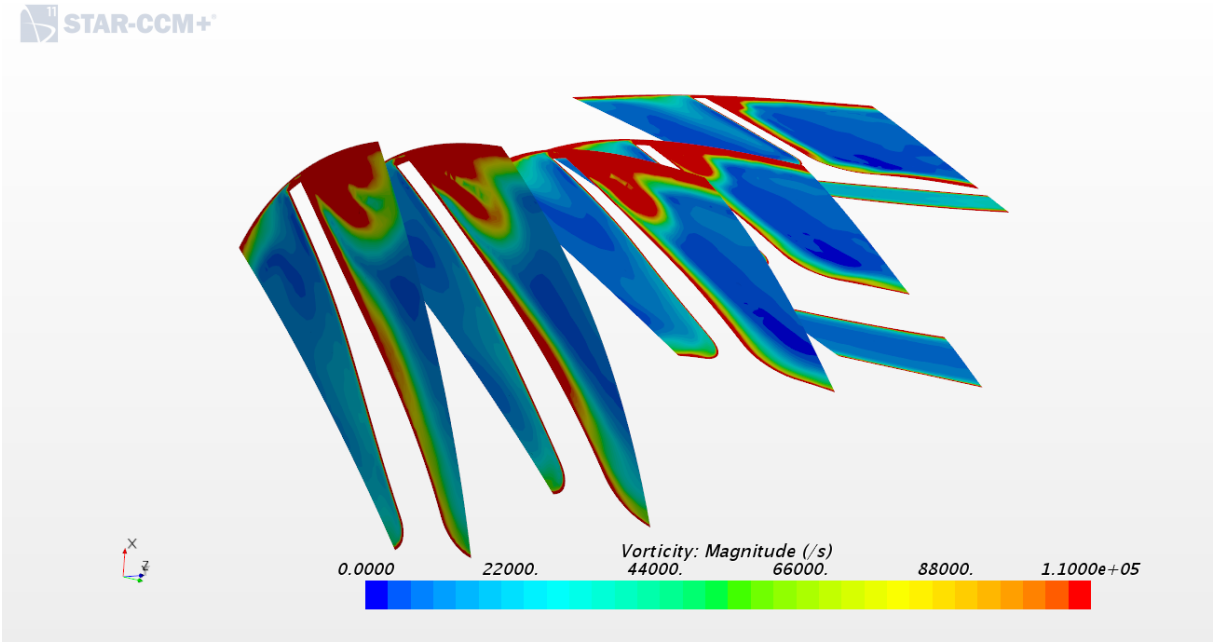

Figure 5.32: Model B at U/Cs equals 0.63

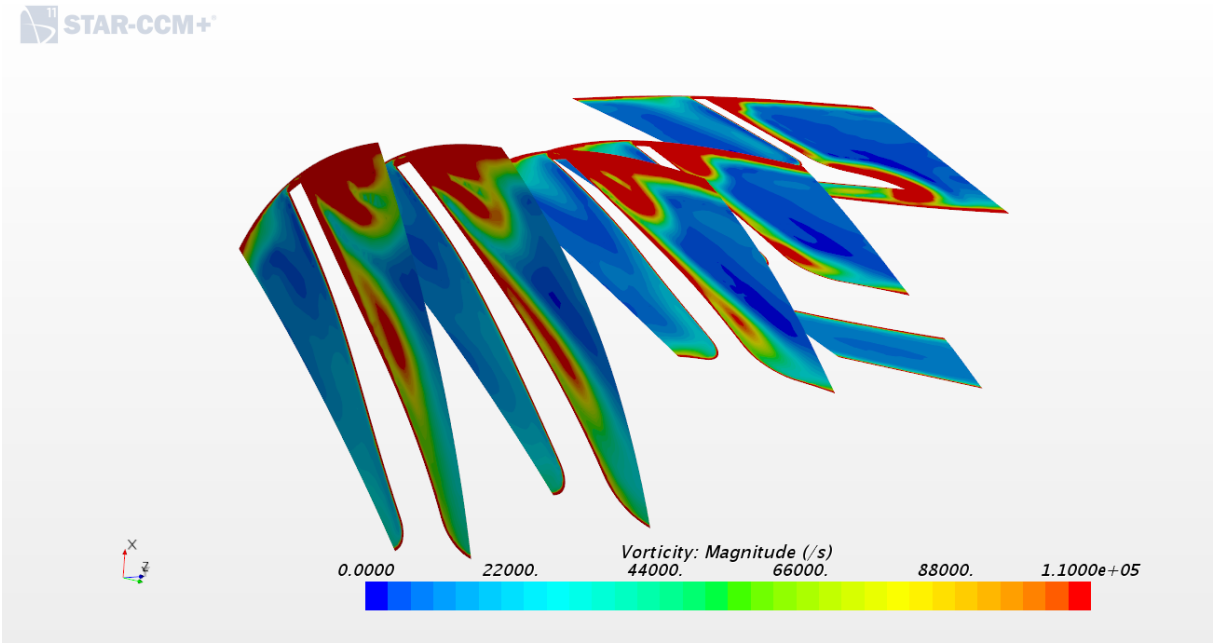

Figure 5.33: Model C at U/Cs equals 0.63

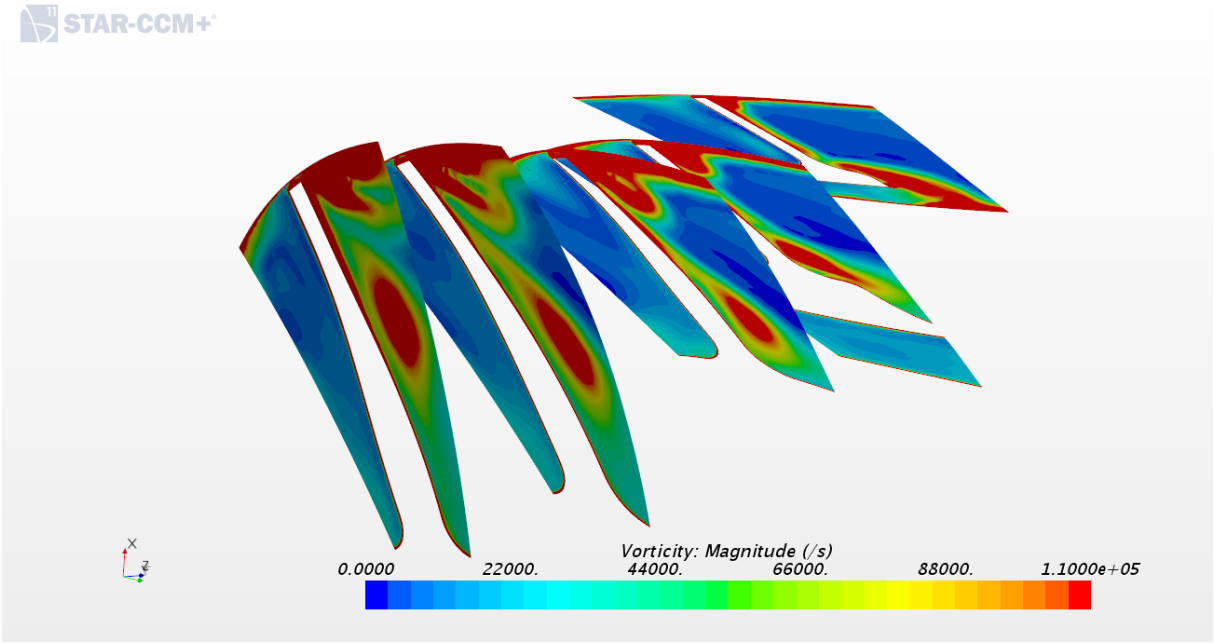

Figure 5.34: Model D at U/Cs equals 0.63

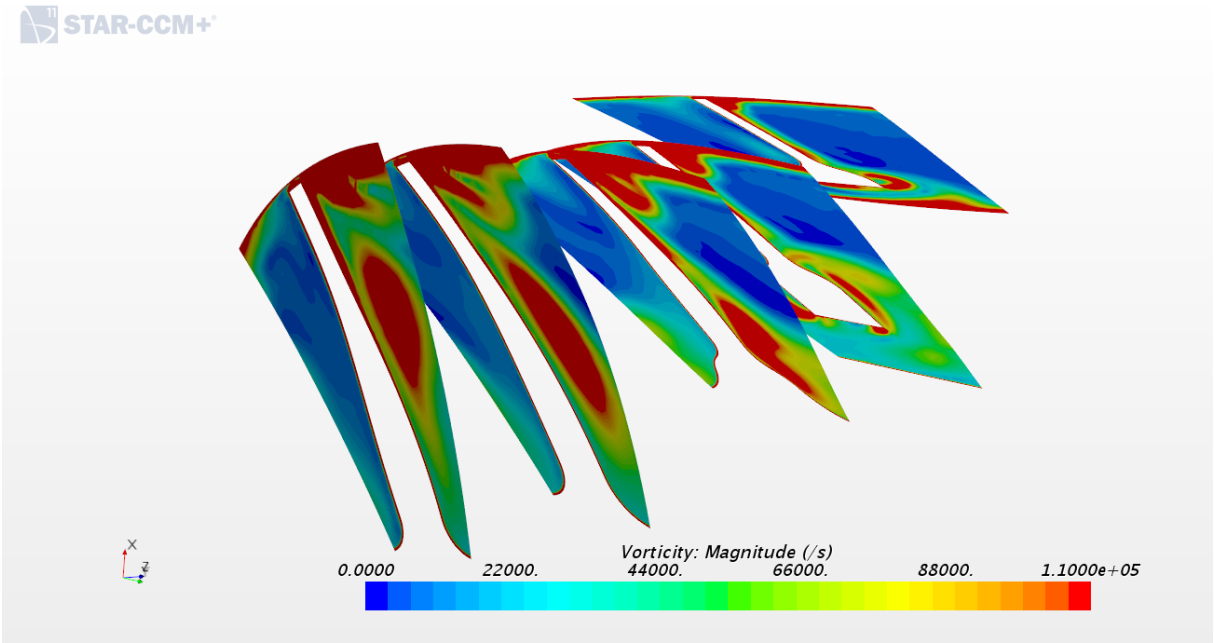

Figure 5.35: Model E at U/Cs equals 0.63

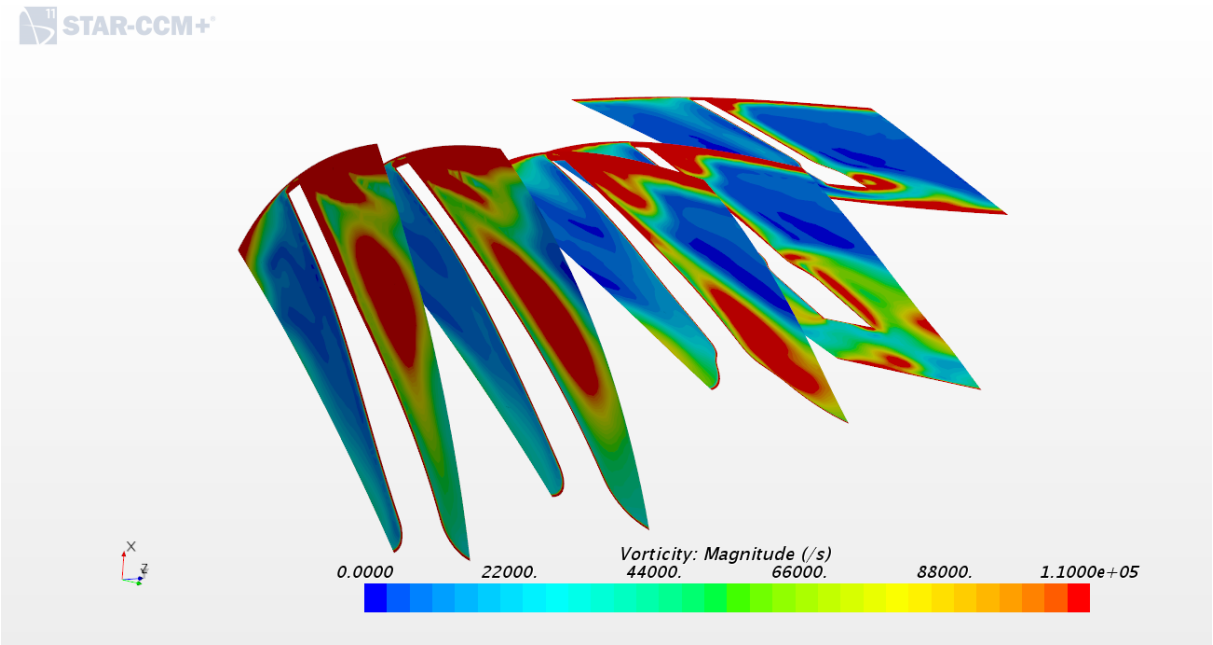

Figure 5.36: Model F at U/Cs equals 0.63

5.4.4 U/Cs=0.51

At velocity ratio 0.51, Model A, figure 5.37 shows a slightly larger red area, on the suction side, directly at the inlet section plane. Which increases with tip clearance leakage further down in the rotor compared to previous Model A at different velocity ratios. The same behaviour can be seen on Model B, 5.38, which now is increased from shroud to hub. This may be a beginning to incidence angle loss or a disturbance when the main stream is affected by the leading edge. Model C, figure 5.39, has the same behaviour as velocity ratio 0.63 but now the generated vortex is bigger. Model D, E and F, figures 5.40 5.41 5.42, show the same behaviour but now with high values of vorticity magnitude.

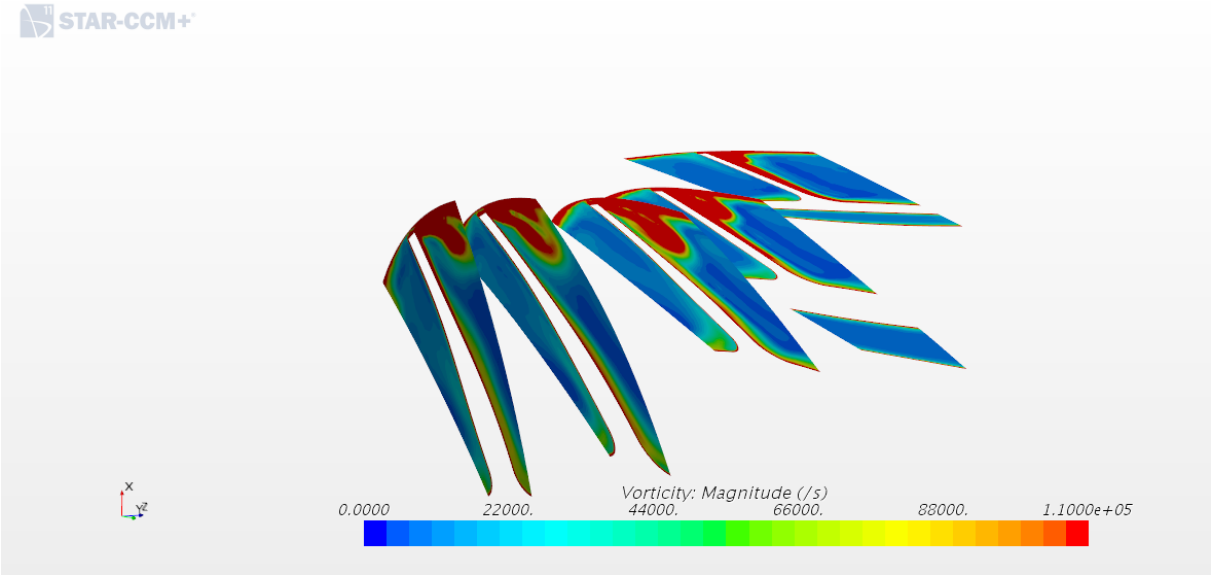

Figure 5.37: Model A at U/Cs equals 0.51

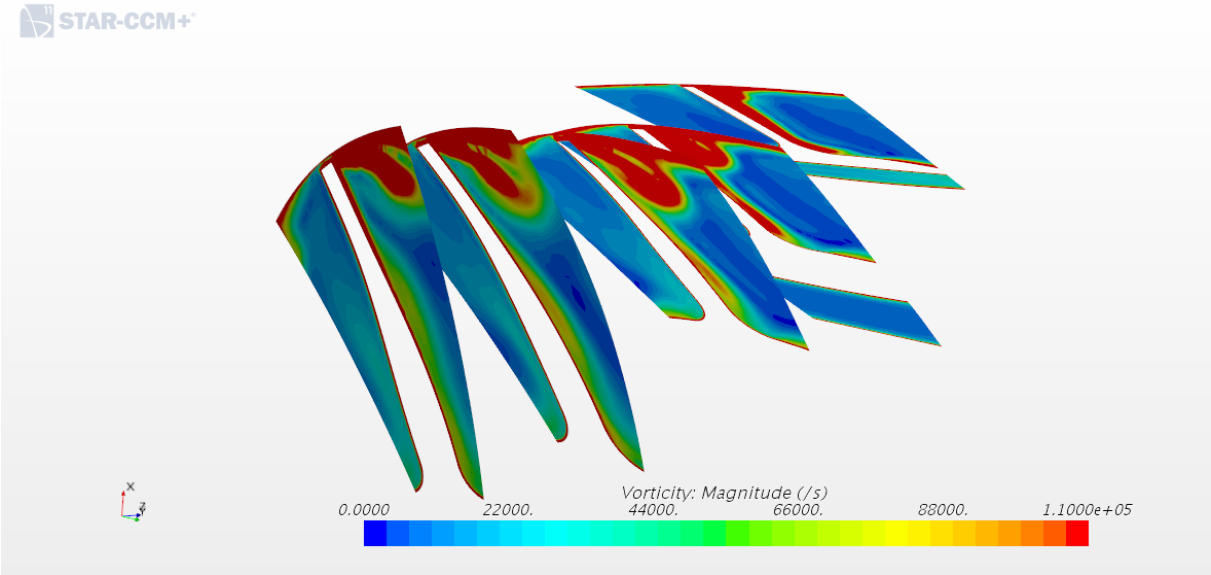

Figure 5.38: Model B at U/Cs equals 0.51

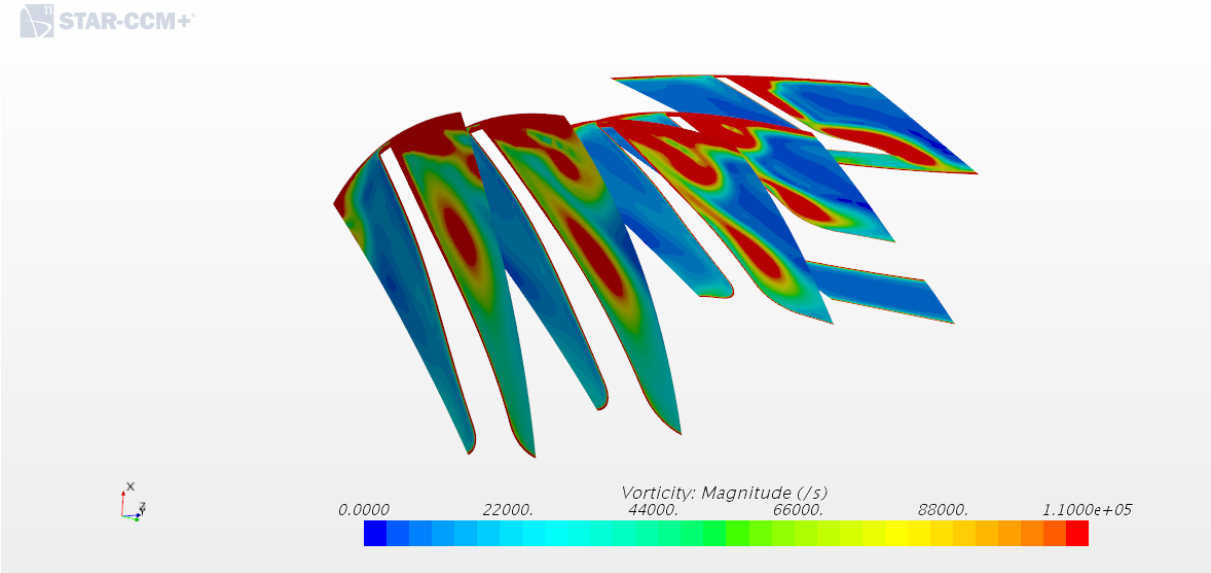

Figure 5.39: Model C at U/Cs equals 0.51

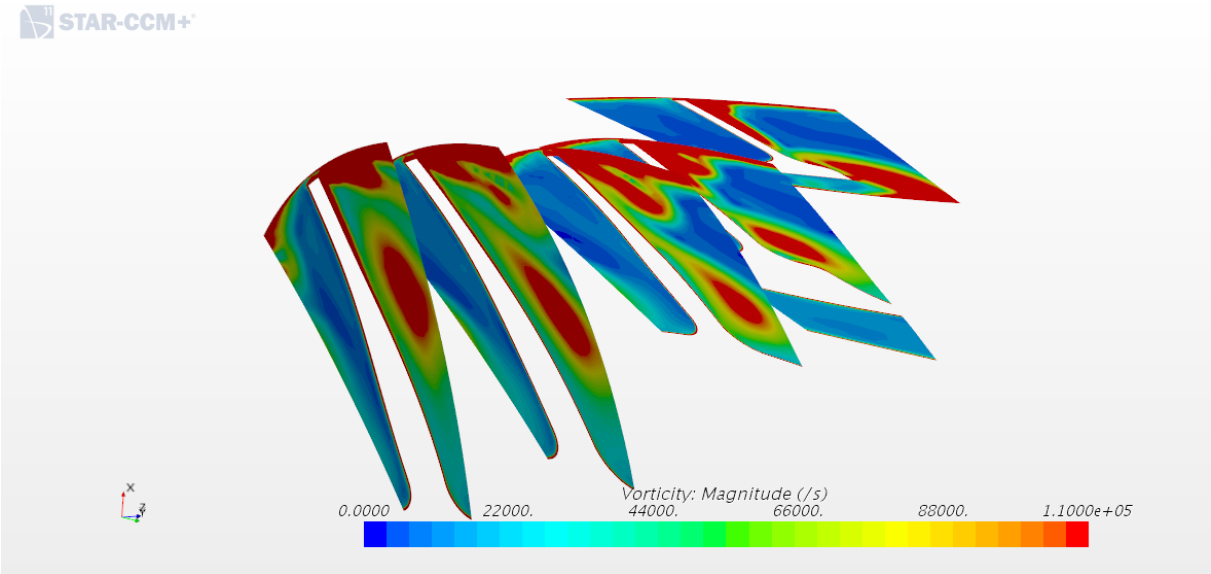

Figure 5.40: Model D at U/Cs equals 0.51

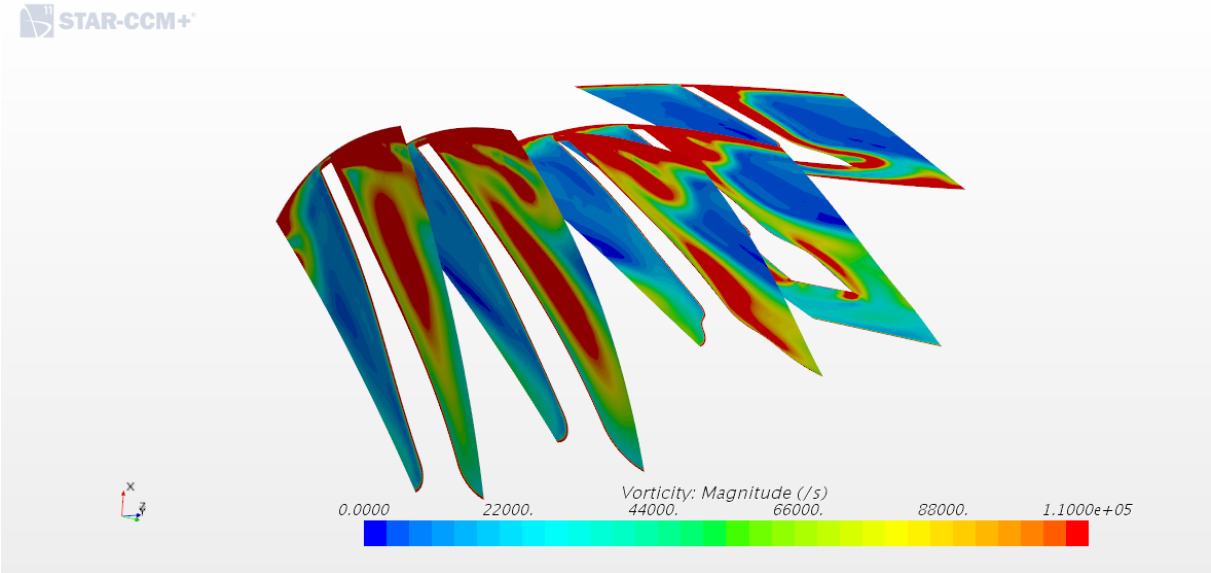

Figure 5.41: Model E at U/Cs equals 0.51

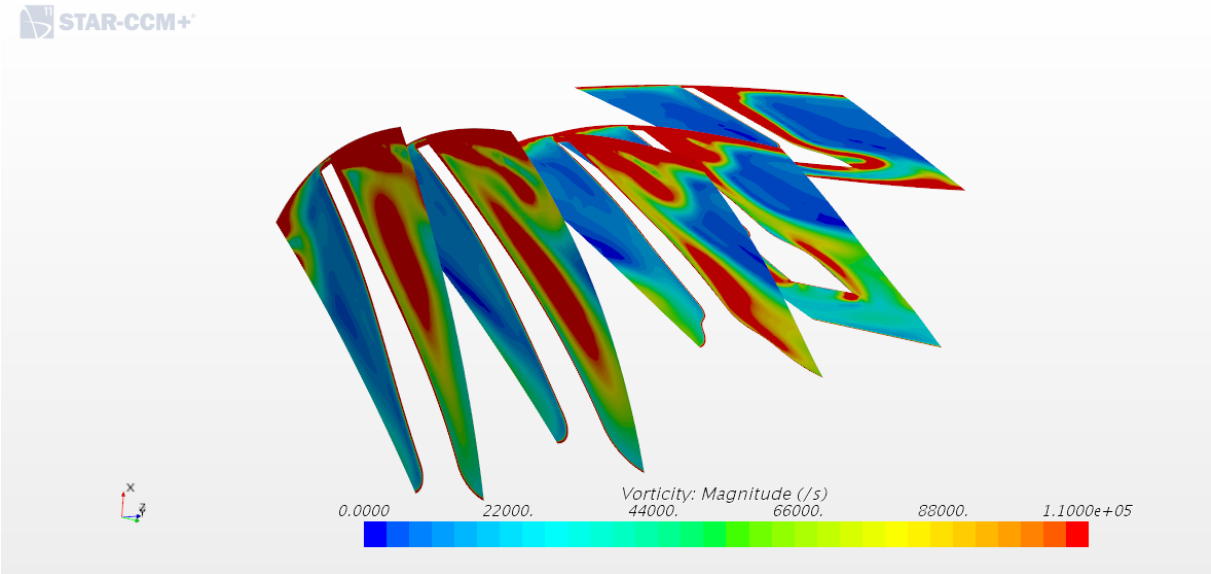

Figure 5.42: Model F at U/Cs equals 0.51

5.4.5 Visualisation of the vortex generated by the Incidence angle

The described phenomena with separation at the inlet section by Woolley and Hatton [4] was possible to detect for the range of velocity ratio 0.51 and 0.77. Figures 5.44, 5.45, 5.46 and 5.47 show the relative streamlines at the inlet for the new Model A. One more extra simulation, figure 5.43, for the new reference Model A at velocity ratio 0.37, was performed and shows the separation at the suction side. This corresponds to the same separation Cox et al.,[7] demonstrated in his article.

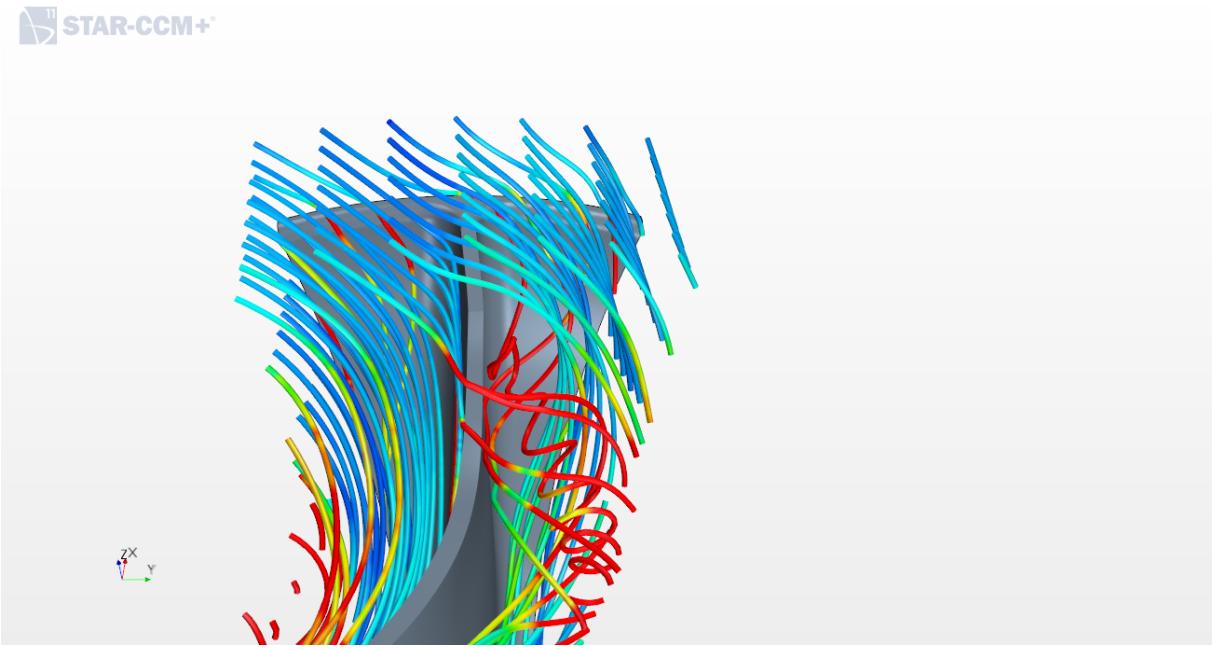

Figure 5.43: Relative velocity streamlines for New Model A at U/Cs 0.37

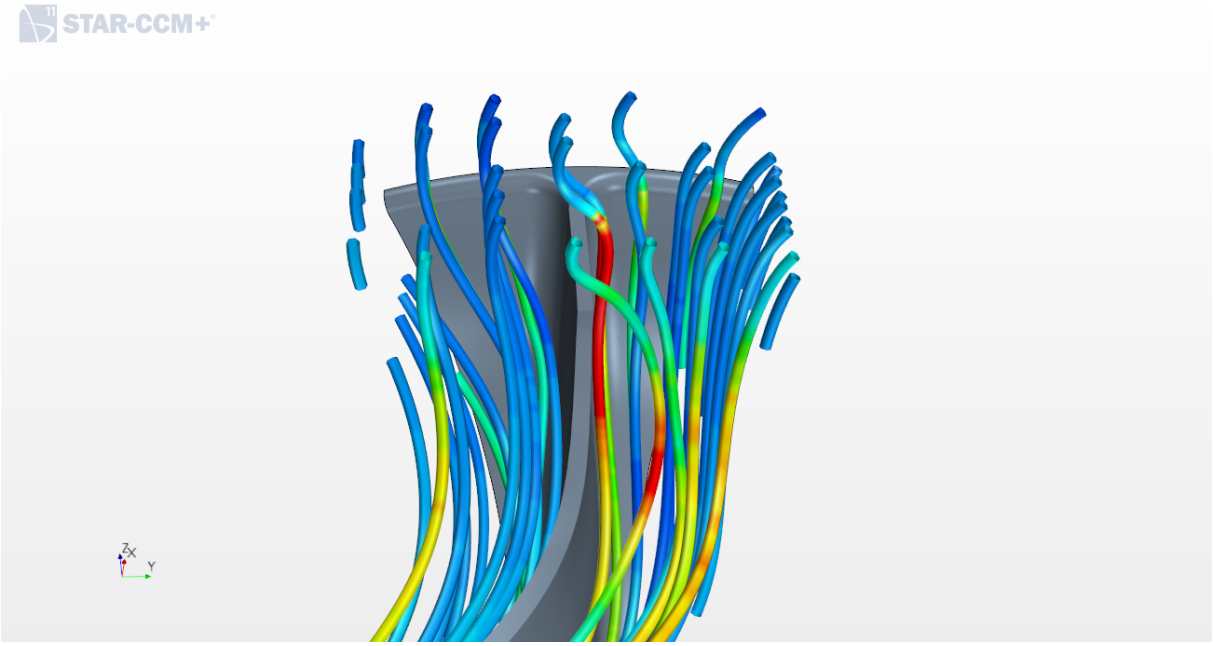

Figure 5.44: Relative velocity streamlines for New Model A at U/Cs 0.51

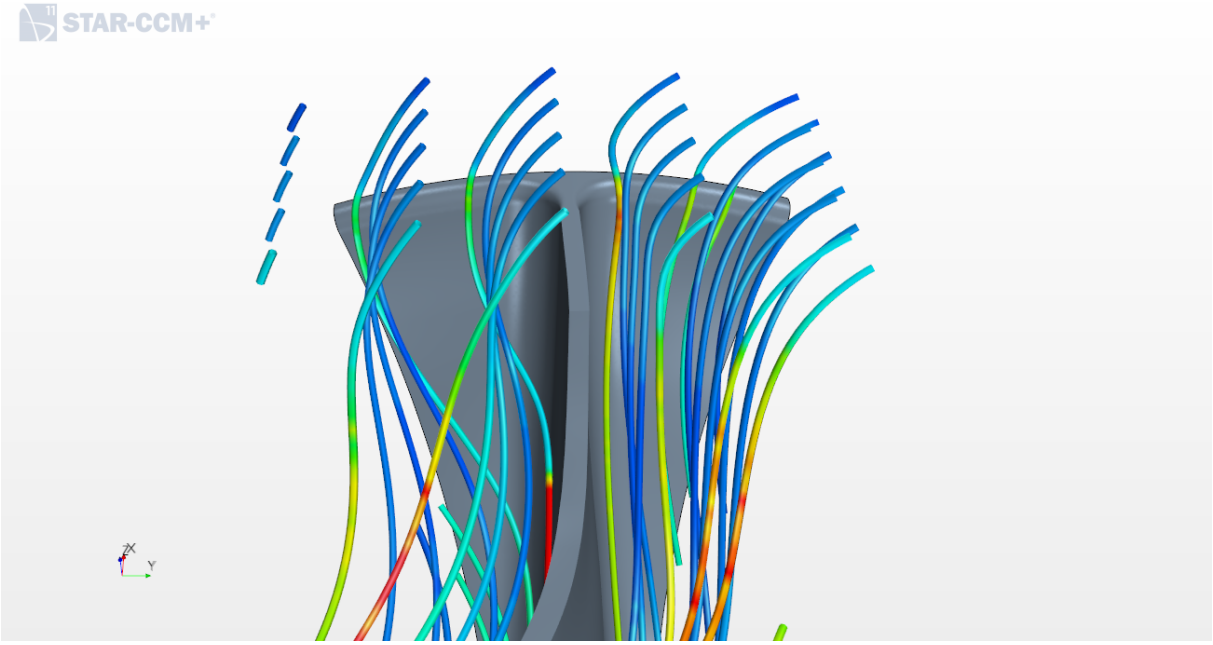

Figure 5.45: Relative velocity streamlines for New Model A at U/Cs 0.63

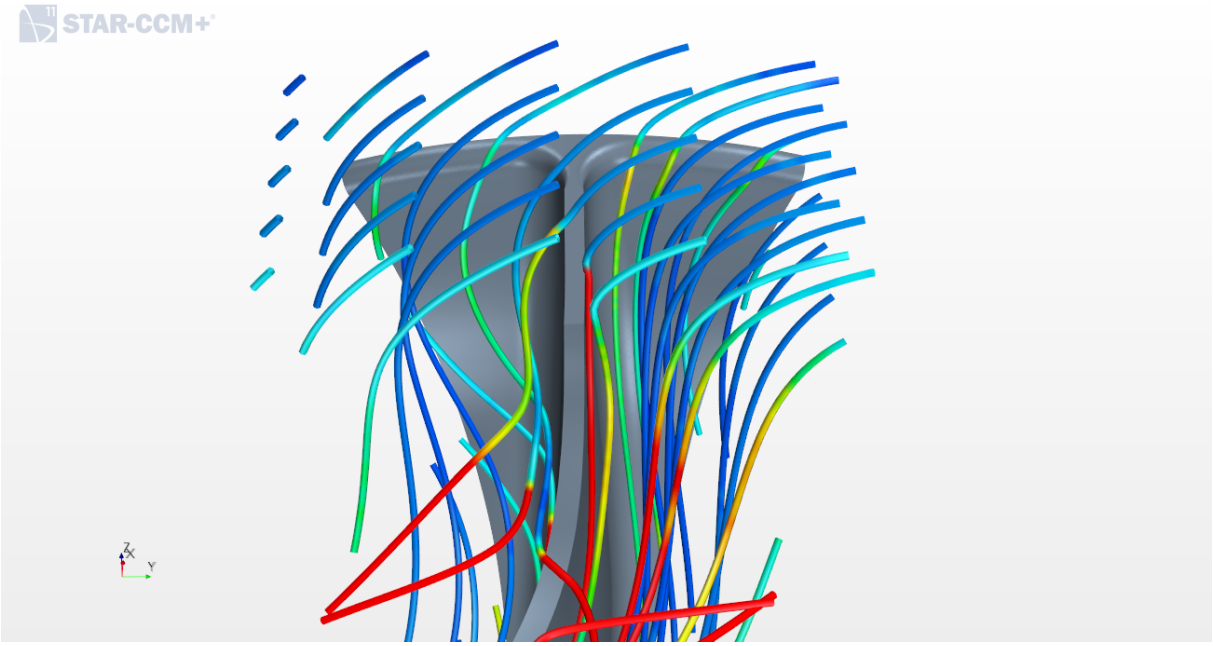

Figure 5.46: Relative velocity streamlines for New Model A at U/Cs 0.73

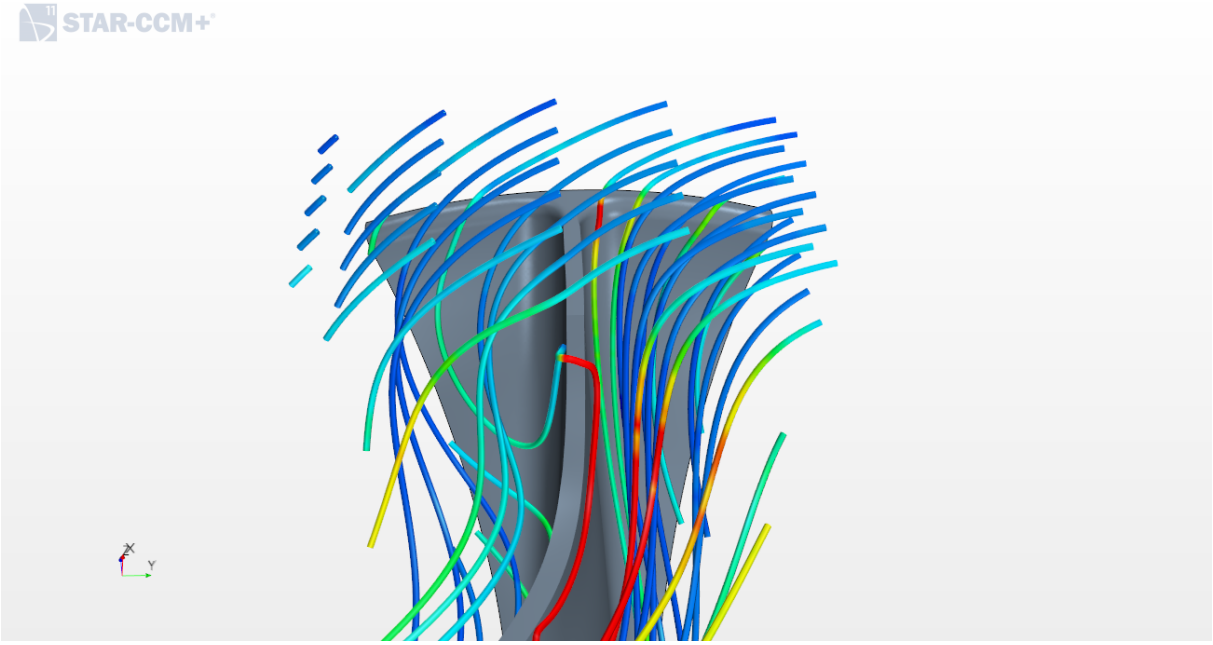

Figure 5.47: Relative velocity streamlines for New Model A at U/Cs 0.77

It seems that the vortex generated by the incidence angle increases with deeper scalloping, especially for Model A, B and C at U/Cs equal 0.77. Figures 5.20 and 5.21, show a small red area of vorticity that was detected at the pressure side of the blade. With section planes in axial direction and relative velocity streamlines from the inlet was it possible to capture a vortex, shown in figure 5.48, on the pressure side. The streamlines and section planes are selected as vorticity in axial direction and the blue and red colour show the direction of the rotation. The vortex corresponds to the same behaviour as the -60 degree rotor, c), inlet flow angle seen in figure 2.3. With a high negative relative inlet angle the flow separates at the pressure surface leading edge and starts to recirculate on the surface [4]. However, at same velocity ratio (0.77) in figure 5.49 and 5.50 Model C is displayed with the vorticity magnitude and streamlines. Now the vortex is increased compare to 5.48 and it seems that the vortex is increased when the streamlines hits the scalloped edge. Figure 5.50 shows the back-face and generated vortex according to the section plane. And again the streamlines hits the scalloped edge on the suction side. It seems that the scalloped edge on a mixed-flow rotor increases the vortex on the pressure side for high velocity ratios.

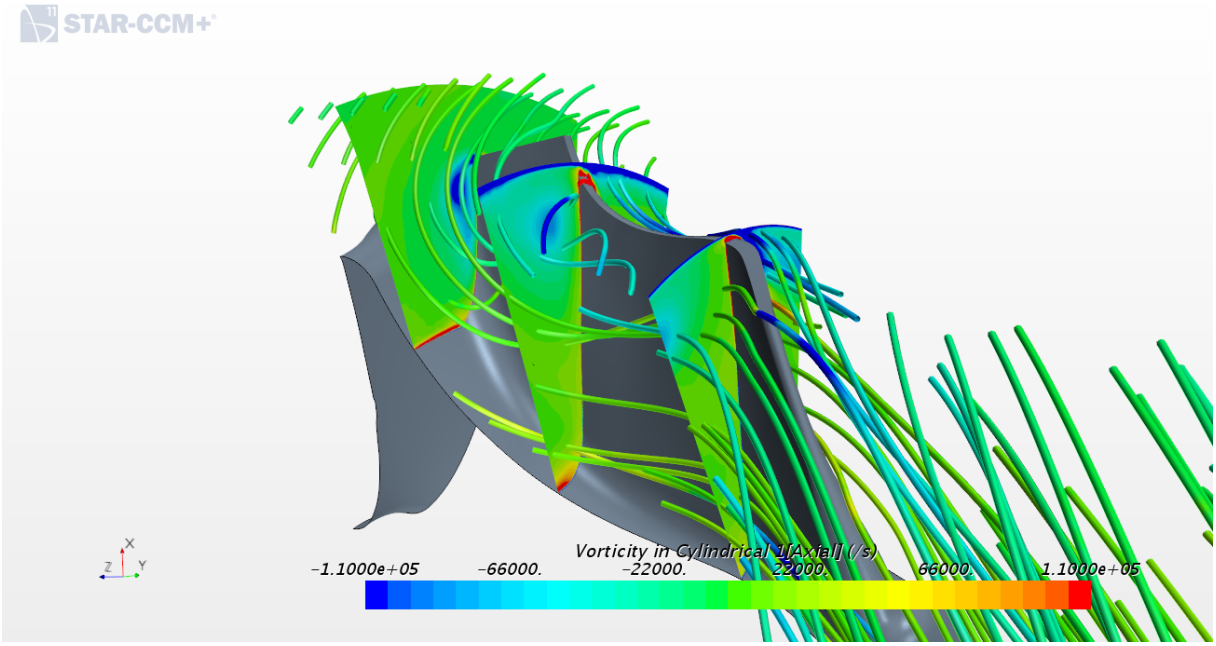

Figure 5.48: Model B at U/Cs equals 0.77, same Model as figure 5.20 but now with vorticity in axial direction. Blue or red colour is the direction of the rotation. With the vortex generated on the pressure side.

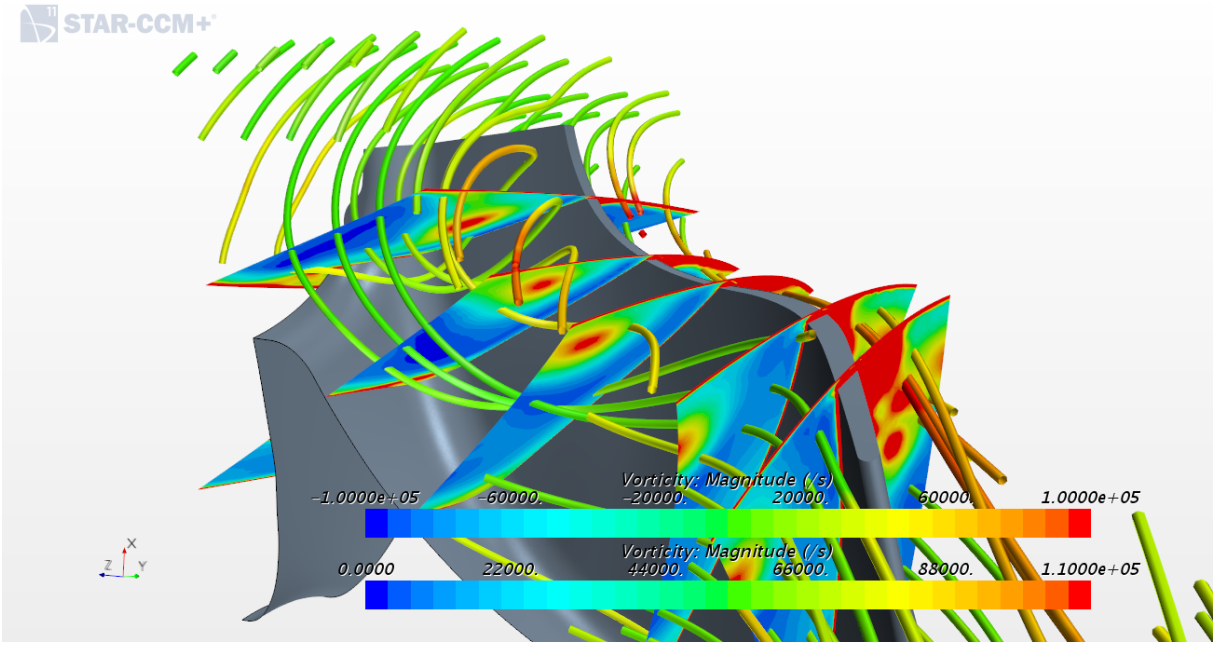

Figure 5.49: Model C at U/Cs 0.77 the same figure as 5.21 but shows the pressure side and with streamlines.

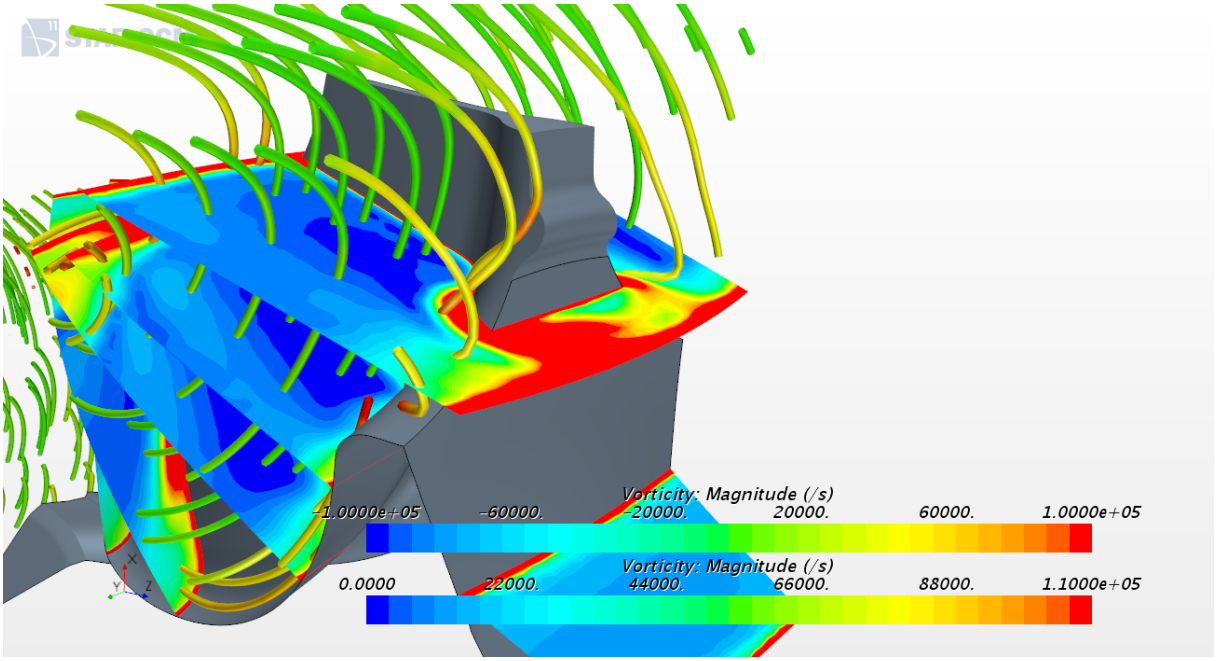

Figure 5.50: Model C at U/Cs 0.77 the same figure as 5.21 but shows the back-face and the suction side with streamlines.

With deep scalloping at velocity ratio 0.63, it does not occur any separation or vortex at the pressure side according to figures in section 5.4.3. But at Model C,figure 5.33, a vortex is generated by the leakage from pressure to suction side. Figures 5.51 and 5.52 show this vortex with streamlines and the vortex .

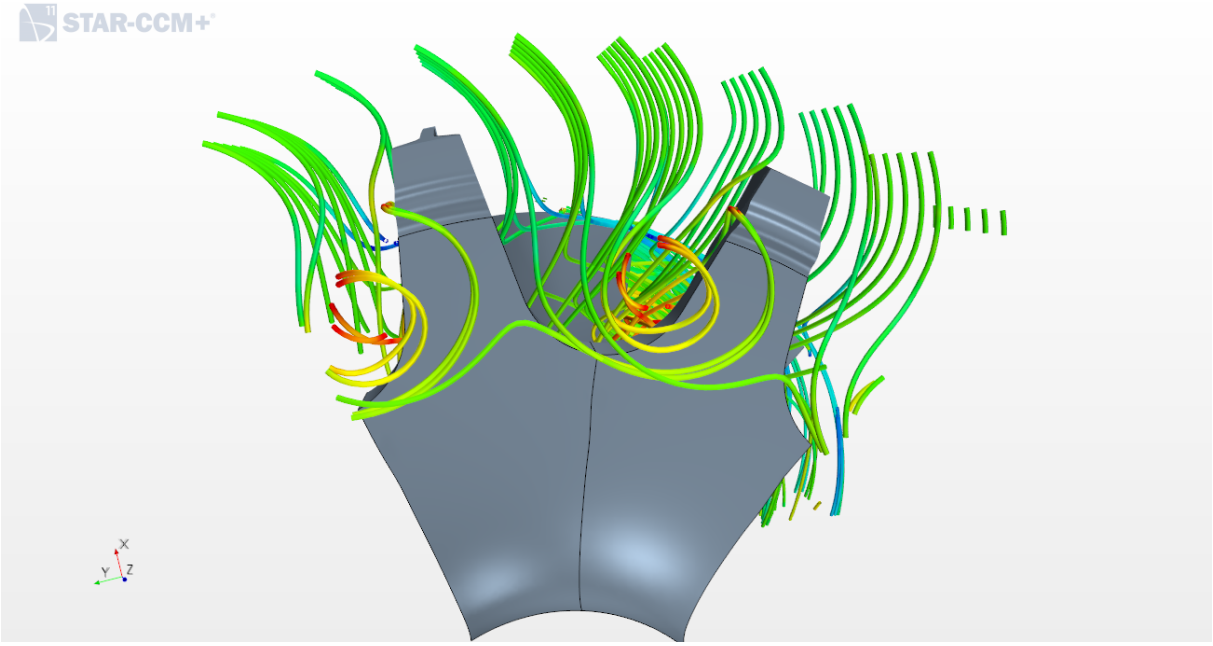

Figure 5.51: Model D at U/Cs 0.63 with streamlines.

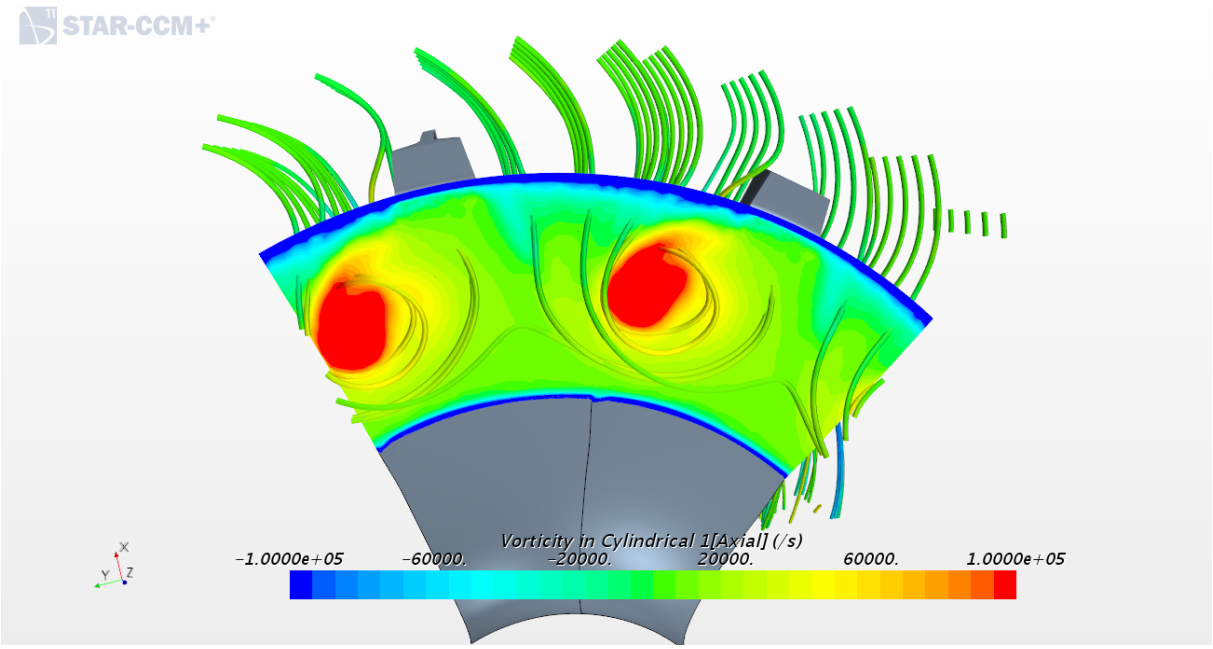

Figure 5.52: Model D at U/Cs 0.63 with streamlines and vorticity in axial direction, viewed backward.

5.5 Constant Speed Response test

A CSR-simulation (Constant Speed Response) was performed by Volvo Powertrain for the new reference model A compared to model B, C and D. The test did not consider model E and F because of low efficiency. The test measure the time in seconds from motored torque to 90% of maximum torque at a constant engine speed [11]. The input values for the simulation were the inertia value for each model and an average rotor total to static efficiency from velocity ratios 0.63, 0.73 and 0.77. In Table 5.3 the achievement from the reduction in inertia is shown in percent for rotor model B, C, D against Model A. The scalloped model B performs better compared to model C and D. With 2.50 to 1.71 percent better transient response time for engine speed 1000-1200 rpm and 4.04 percent at engine speed 1400 rpm. This is achieved by a quite small reduction of inertia of 6.26 percent, Table 5.2, and low reduction in efficiency. Even if Model D has a reduction of inertia to 20 percent it still performance worse than Model A in transient response time. This is because the CSR-simulation consider both the inertia and the efficiency.

Table 5.3: The reduced transient response time in percent normalised against new reference Model A.

RPM	1000	1100	1200	1300	1400	1500	1600
Model B	2.5	2.04	1.71	0.00	4.04	0.00	0.00
Model C	1.01	0.00	0.85	0.00	0.00	0.00	0.00
Model D	0.00	-1.36	-0.85	-0.99	5.05	1.09	0.00

Chapter 6

Conclusion

- The mixed-flow prototype turbine, Model A, designed at Volvo Powertrain AB was scalloped in five different models and simulated with Computational Fluid Dynamics.
- The scalloped models were evaluated against the loss model diagram by Baskharone.
  - In the first design step, Model B showed better efficiency compared to reference Model A. However, this was considered as a measurement error and a new design was developed.
  - A new design of the reference Model A was developed by adding a rounding of the edge between the radial blades. The rounding improved the performance and made the rotor models comparable.
  - The most promising design is the scalloped rotor Model B with similar efficiency and a reduction in transient response time to 2.5 % compared to the new design of the reference rotor Model A.
- Section plane with vorticity scalar field and streamlines have proven good quality of indicating the flow through the rotor.

6.1 Further work

Because this study has focused on steady state simulations, it would be preferable to analyse the new reference Model A and Model B in transient pulse flow mode with CFD for better accuracy of the efficiency.

Bibliography

[1] CD-Adapco. *STAR-CCM+ User Guide*.

[2] Nicolas C. Baines. *Fundamentals of Turbocharging*. Concepts NREC, 2005. ISBN: 0-93328-14-8.

[3] Nicolas C. Baines. *Turbochargers, Advanced integration and design for internal combustion engines*. Course notes. Concepts NREC, 2015.

[4] Nicolas C. Baines et al. *Axial and Radial Turbines*. Concepts NREC, 2003. ISBN: 0-933283-12-0.

[5] Erian A. Baskharone. *Principles of Turbomachinery in Air-Breathing Engines.* 2006. ISBN: 978-0-521-85810-6.

[6] Graham Cox, Jason Wu, and Ben Finnigan. "A Study on the flow around the scallops of a mixed-flow turbine and its effect on efficiency." In: *AMSE* GT2007-27330 (2007).

[7] Grahma Cox, Alex Roberts, and Michael Casey. "The Development of a Deviation Model for Radial and Mixed-Flow Turbines for Use in Throughflow Calculations." In: *ASME* GT2009-59921 (2009).

[8] Magnus Genrup. "Lecture notes, Chapter 7 - Radial Turbines." In: (2016).

[9] F. Moukalled, L. Mangani, and M. Darwish. *The Finite Volume Method in Computional Fluid Dynamics*. Springer, 2016. ISBN: 978-3-319-16873.

[10] Jiyuan Tu, Guan-Heng Yeoh, and Chaoqun Liu. *Computional Fluid Dynmaics, A Practical Approach*. Second Edition. Elsevier Ltd, 2013. ISBN: 978-0-08-098243-4.

[11] Internal report: Volvo Powertrain AB. "Methodology for constant speed response (CSR) simulation in ICES." In: (2015).

Appendix A

Example of Residuals and Reports

Appendix A shows the examples of the residuals and report plot for the mass flow and temperature.

Figure A.1: Report plot of the difference between the mass flow at inlet and outlet

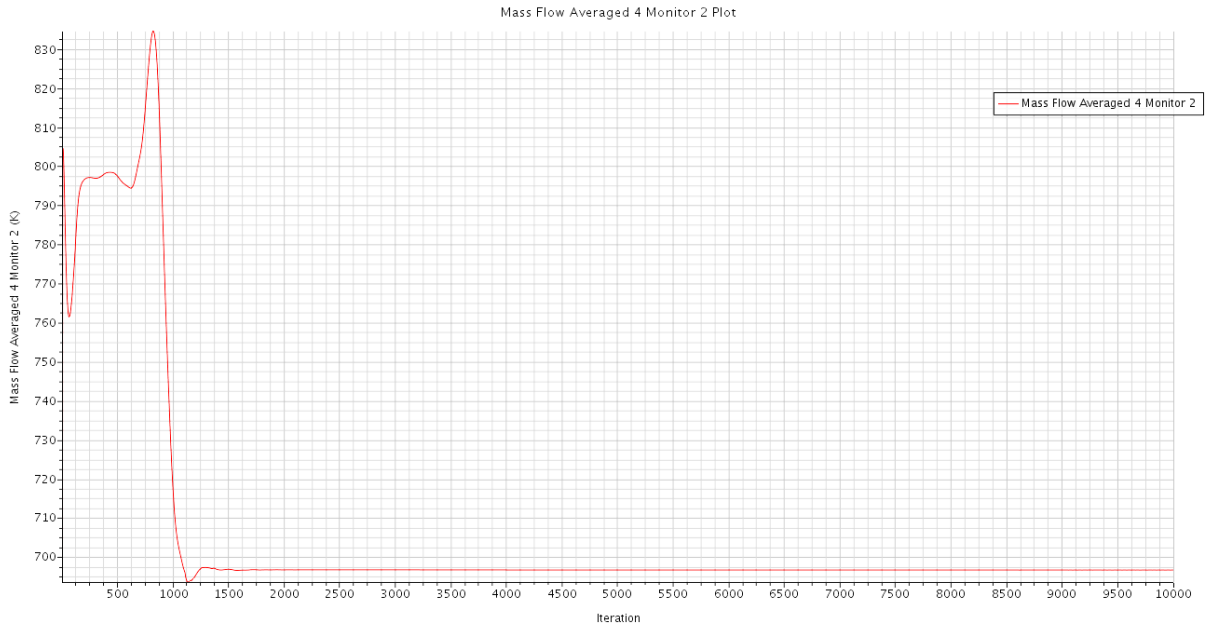

Figure A.2: Report plot of the total temperate at the outlet (T06)

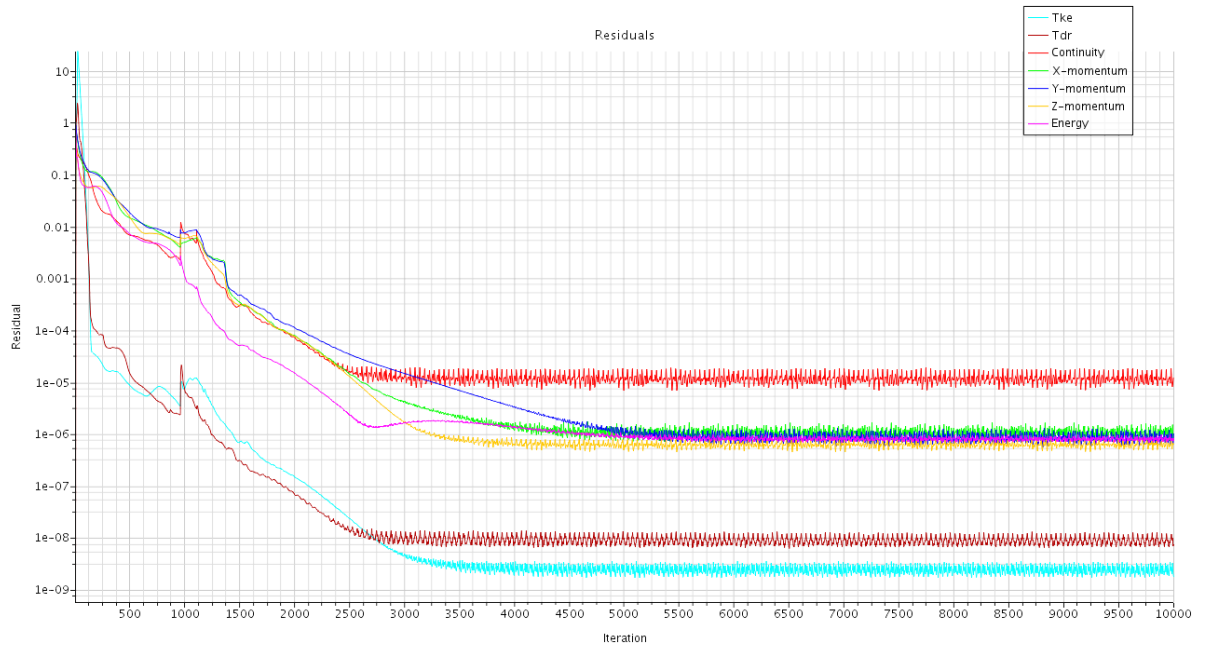

Figure A.3: Report plot of the residuals.

Appendix B

Example of Mesh Diagnostics

Appendix B shows an example of the Mesh Diagnostic test in STAR-CCM+.

```
 Extents:
  x: [0.0000000000e+00, 4.6719740782e-02] m
  y: [-3.2333481871e-02, 1.2615427494e-02] m
  z: [-9.9679999981e-02, 5.0180001124e-02] m
 Maximum interior cell index delta: 12199, average: 2.2952740927e+02
 Maximum cell face index delta: 66936, average: 1.5667241163e+02
 Volume range: [7.3956474210e-16, 5.8553467630e-10] m^3
 Minimum volume in cell with pro-STAR Cell ID 970265
 Minimum distance between centroids of neighbor cells = 7.4785111027e-06
       between cells with pro-STAR Cell ID 952446 and 948684
 Maximum skewness angle = 8.7021263123e+01 deg in cell with pro-STAR Cell ID 975151

Face validity:
Minimum Face Validity: 1.0000000000e+00
Maximum Face Validity: 1.0000000000e+00
        Face Validity <  0.50           0    0.000%
0.50 <= Face Validity <  0.60           0    0.000%
0.60 <= Face Validity <  0.70           0    0.000%
0.70 <= Face Validity <  0.80           0    0.000%
0.80 <= Face Validity <  0.90           0    0.000%
0.90 <= Face Validity <  0.95           0    0.000%
0.95 <= Face Validity <  1.00           0    0.000%
1.00 <= Face Validity             1412483   100.000%

Volume Change:
Minimum Volume Change: 1.002528e-03
Maximum Volume Change: 1.000000e+00
         Volume Change <  0e+00           0    0.000%
0e+00 <= Volume Change <  1e-06           0    0.000%
1e-06 <= Volume Change <  1e-05           0    0.000%
1e-05 <= Volume Change <  1e-04           0    0.000%
1e-04 <= Volume Change <  1e-03           0    0.000%
1e-03 <= Volume Change <  1e-02        1065    0.075%
1e-02 <= Volume Change <  1e-01       12395    0.878%
1e-01 <= Volume Change <= 1e+00     1399023   99.047%
 Maximum boundary skewness angle in region = 8.702126e+01 deg
```

Figure B.1: Example of the Mesh Diagnostics test in STARCCM+

Appendix C

Post-processing alternatives

Appendix C includes an alternative for evaluating the losses. An example of vorticity versus Helicity is shown. By comparing the two figures, seems the vorticity to visualise the generated vortex better than helicity. Therefore, was vorticity selected as the evaluation method in Results: Vorticity.

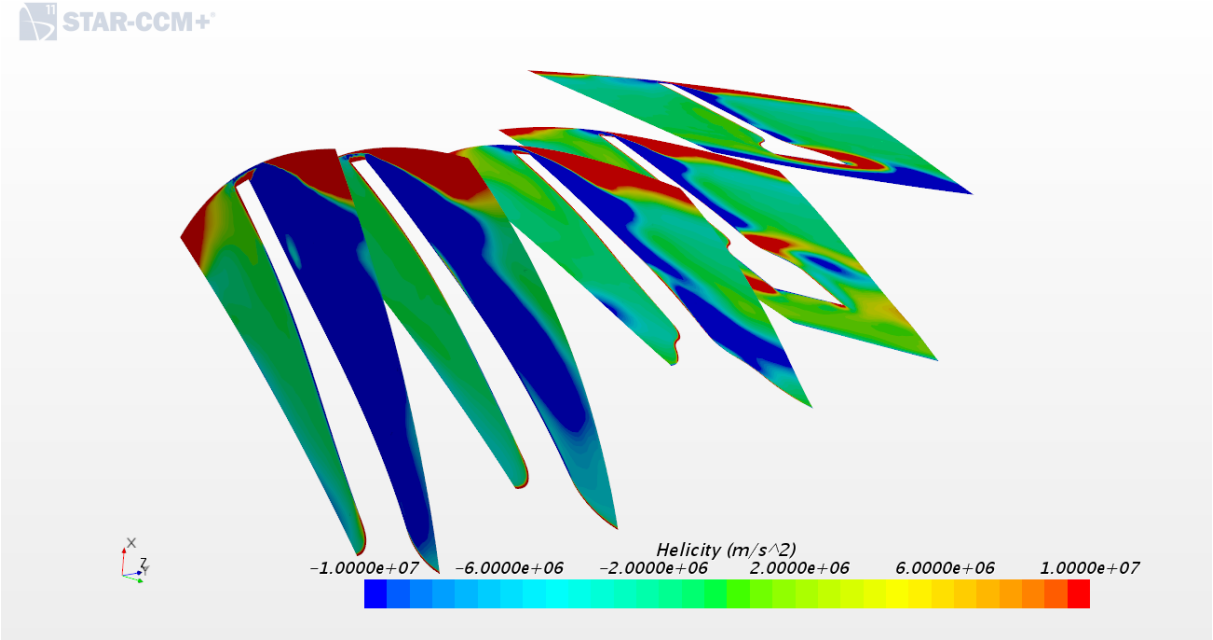

Figure C.1: Show the Helicity, the scalar of velocity and vorticity, Model E at U/Cs 0.63

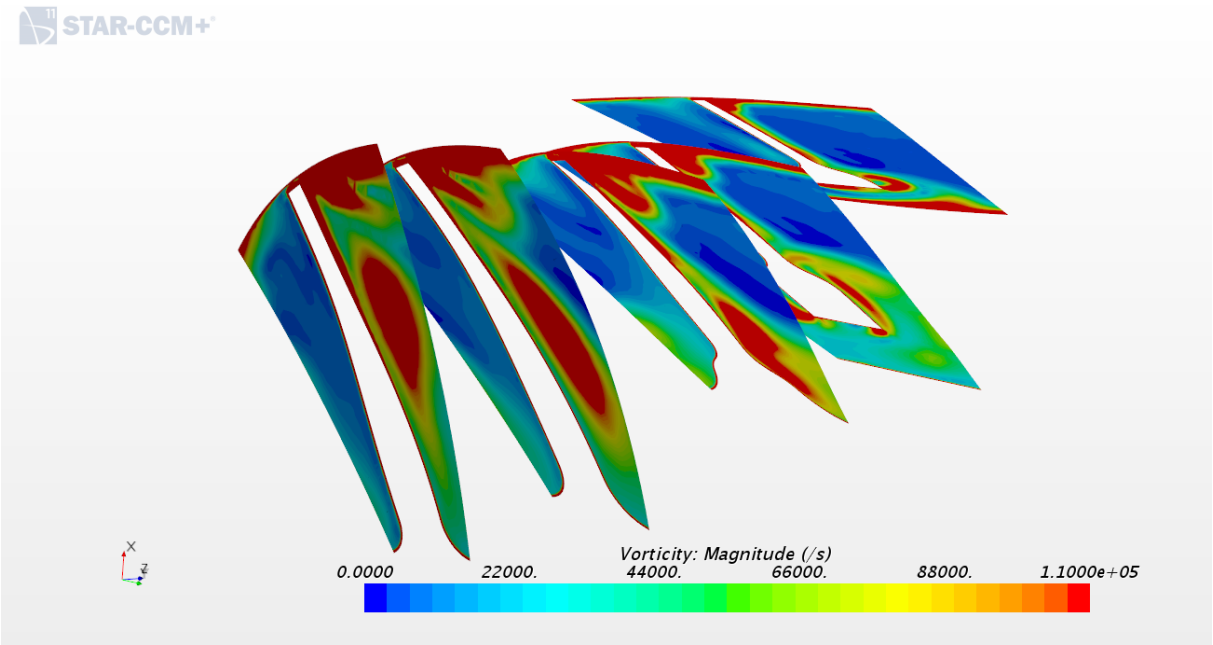

Figure C.2: Show the vorticity magnitude of Model E at U/Cs 0.63, same figure as 5.35

Appendix D

Example of y+ value

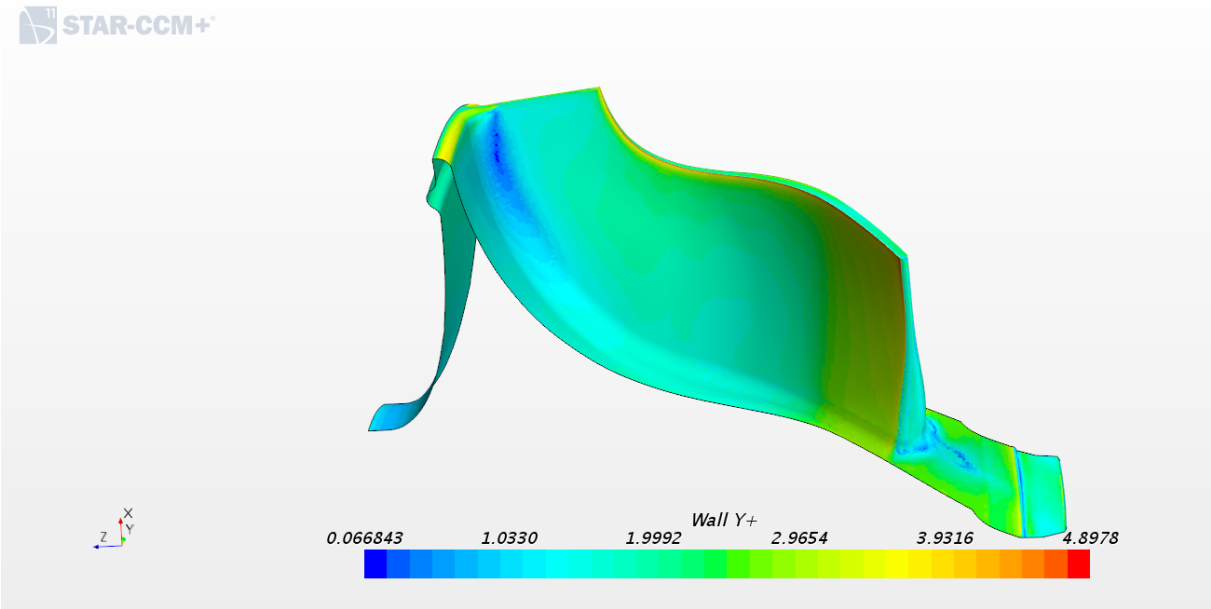

Figure D.1: Shows the $y+$ value for New reference Model A adn that the value is below five.